



EUROPEAN SOUTHERN OBSERVATORY

Organisation Européenne pour des Recherches Astronomiques dans l'Hémisphère Austral

Europäische Organisation für astronomische Forschung in der südlichen Hemisphäre

VERY LARGE TELESCOPE

The Cerro Paranal Advanced Sky Model

VLT-MAN-ESO-19550-5339

Issue 1.1.1

Date 2013-09-18

Prepared: Innsbruck In-Kind Team 2013-09-18
.....
Name Date Signature

Approved: Jakob Vinther
.....
Name Date Signature

Released: Pascal Ballester
.....
Name Date Signature

This page was intentionally left blank

ESO	The Cerro Paranal Advanced Sky Model	Doc:	VLT-MAN-ESO-19550-5339
		Issue:	Issue 1.1.1
		Date:	Date 2013-09-18
		Page:	3 of 80

Change record

Issue/Rev.	Date	Section/Parag. affected	Reason/Initiation/Documents/Remarks
1.1.1	30/08/2018	1, 3, 5.7, 6.2.1, 7	Updated to current status.
1.1	18/09/2013	All	RIXes for final review considered
1.0	29/07/2013	All	First version

Main authors (Austrian ESO In-Kind Team Innsbruck)

Stefan Noll
 Wolfgang Kausch
 Marco Barden
 Amy M. Jones
 Cezary Szyszka
 Stefan Kimeswenger (head)

Institute for Astro- and Particle Physics, University of Innsbruck
 Technikerstr. 25/8
 A-6020 Innsbruck / Austria

ESO contact: usd-help@eso.org

This page was intentionally left blank

ESO	The Cerro Paranal Advanced Sky Model	Doc:	VLT-MAN-ESO-19550-5339
		Issue:	Issue 1.1.1
		Date:	Date 2013-09-18
		Page:	5 of 80

Contents

1	Introduction	7
1.1	Structure of this document	7
1.2	Abbreviations	7
2	Overview	9
2.1	Module 1	9
2.2	Module 2	9
3	The ETC interface	13
4	Radiative transfer code	17
4.1	Line File / Line-By-Line Radiative Transfer Model (LNFL/LBLRTM)	17
4.2	Line input sources	18
5	Atmospheric profiles and meteorological data	20
5.1	Atmospheric standard profile	20
5.2	GDAS profiles	23
5.3	ESO meteo monitor (EMM)	23
5.4	GDAS profile library	25
5.5	Processing of the GDAS profiles and the EMM data	40
5.6	Merging standard and GDAS profiles	43
5.7	Profiles for given PWV values	43
6	Sky model components	45
6.1	Transmission	45
6.2	Radiance	46
6.2.1	Scattered moonlight	47
6.2.2	Scattered starlight	49
6.2.3	Zodiacal light	49
6.2.4	Thermal emission by telescope and instrument	50
6.2.5	Molecular emission of the lower atmosphere	51

ESO	The Cerro Paranal Advanced Sky Model	Doc:	VLT-MAN-ESO-19550-5339
		Issue:	Issue 1.1.1
		Date:	Date 2013-09-18
		Page:	6 of 80

6.2.6	Emission lines of the upper atmosphere	51
6.2.7	Airglow continuum	56

7	Comparison with observational data	57
7.1	Verification data set	57
7.2	Comparison of spectra	60
7.3	Comparison of photometry	71
7.4	Conclusions	75

ESO	The Cerro Paranal Advanced Sky Model	Doc:	VLT-MAN-ESO-19550-5339
		Issue:	Issue 1.1.1
		Date:	Date 2013-09-18
		Page:	7 of 80

1 Introduction

This document is intended to be a guide for the Cerro Paranal Advanced Sky Model (ASM), which has been part of the Innsbruck contribution of the Austrian ESO in-kind project. The project has aimed at providing a detailed and reliable sky background model for present and future ESO Exposure Time Calculators (ETCs).

The audience of this document is intended to be ETC users who want to obtain detailed information on the basic structure and physical background of this model, but without the need to know details about the software structure and installation. For that we refer to the `The_Cerro_Paranal_Advanced_Sky_Model_User_Manual.pdf`, which includes sections about the software and procedures for installation and execution, the individual code segments (called modules) and the incorporated external software.

Further details on the ASM can be found in the paper Noll et al. [2012], which focuses on the optical wavelength regime. The current version of the model contains a more advanced model for scattered moonlight as described in Noll et al. [2012]. A detailed description of the new scattered moonlight model is provided in Jones et al. [2013].

1.1 Structure of this document

This document is organised as follows: A general overview of the structure of the model is given in Section 2. Details on the interface to the ETC (and SkyCalc) including the required input parameters are provided in Section 3. Information on the external radiative code used is provided in Section 4. The meteorological input data and the library of molecular spectra are described in Section 5. A detailed description of the individual components of the ASM is given in Section 6. Finally, a comparison of the sky model with existing verification data is carried out in Section 7.

1.2 Abbreviations

AER: Atmospheric and Environmental Research

ARL: Air Resources Library

ASM: Advanced Sky Model

CPL: Common Pipeline Library

CRIRES: CRyogenic high-resolution InfraRed Echelle Spectrograph

EMM: ESO meteo monitor

ETC: exposure time calculator

FORS: FOcal Reducer and low dispersion Spectrograph

GDAS: Global Data Assimilation System

HITRAN: high-resolution transmission (database)

IR: infrared

ISL: integrated starlight

LBLRTM: Line-By-Line Radiative Transfer Model

LNFL: line file creation programme

NOAA: National Oceanic and Atmospheric Administration

OMI: Ozone Measuring Instrument

PWV: precipitable water vapour

ESO	The Cerro Paranal Advanced Sky Model	Doc:	VLT-MAN-ESO-19550-5339
		Issue:	Issue 1.1.1
		Date:	Date 2013-09-18
		Page:	8 of 80

RFM: Reference Forward Model

ROLO: RObotic Lunar Observatory

SINFONI: Spectrograph for INtegral Field Observations in the Near Infrared

UV: ultraviolet

UVES: Ultraviolet and Visual Echelle Spectrograph

VLT: Very Large Telescope

WMO: World Meteorological Organization

ESO	The Cerro Paranal Advanced Sky Model	Doc:	VLT-MAN-ESO-19550-5339
		Issue:	Issue 1.1.1
		Date:	Date 2013-09-18
		Page:	9 of 80

2 Overview

The software is divided into two parts, so-called modules. Module 1 calculates a synthetic sky spectra library using the radiative transfer code LBLRTM V12.2 (Section 2.1). Module 2 calculates and adds all additional components of the background model, which need only a very short computing time (Section 2.2).

2.1 Module 1

Module 1 creates a synthetic sky spectra library based on data described in Section 4.2 (HITRAN) and meteorological data. The HITRAN 2008 database (see [4] and references therein) gives spectral lines of up to 42 molecules and atoms. The meteorological data is taken from the Cerro Paranal Meteo Monitor and is used to define a parameter space grid for average weather conditions of the observing site Cerro Paranal. For each data point of this grid an atmospheric profile is calculated by merging an atmospheric standard profile and the GDAS profiles provided online by NOAA (see [5], [6], [7], and Section 5 for more details on the atmospheric profiles). Both, the atmospheric profiles and the HITRAN spectrum are used as input for the third party radiative transfer code package LBLRTM, which create a synthetic sky spectrum for each of the corresponding atmospheric profiles. LBLRTM requires the line file creation programme LNFL to convert the HITRAN data into the required proprietary format. As Module 1 is intended to create a synthetic sky spectra library, which is subsequently used as input for Module 2, it has to be run only once. Reruns are only required if the LBLRTM version, the HITRAN database, and/or the input profile data change. Figure 1 shows the workflow within Module 1: Based on the HITRAN database, the radiative transfer code LBLRTM is used to calculate a library of synthetic sky spectra. Each spectrum consists of a radiance and a transmission spectrum.

The calculation of airglow line spectra (see Section 6) requires the effective atmospheric transmission for each airglow line. The convolution of a transmission spectrum with each individual line profile at a required resolution of about 10^6 is too time-consuming for Module 2. Hence, line transmission lists are precalculated for all library spectra by a so-called Module 1a (see Figure 2).

2.2 Module 2

Module 2 of the ASM code aims at adding the background model components, which require only small amounts of computing time. Hence, these routines can be carried out during every single ETC call. These components are the scattered moonlight, scattered starlight, zodiacal light, telescope emission, and non-thermal atmospheric continuum and emission lines (see Section 6 for more information). All components are added to the spectrum selected from the library, which is best correlated to the user input selections (see Figure 3). Module 2 is linked to Module 1/1a by re-using the molecular radiance and transmission spectra and airglow line transmission lists produced by the first component of the ASM code. The maximum wavelength range and resolution of the Module 2 output spectra depend on the corresponding values for the Module 1 library data. Wavelengths between 0.3 and 30 μm and a resolution of $3 - 4 \times 10^5$ are guaranteed.

Module 2 requires a set of parameters related to target, Moon, and Sun positions, solar activity, the time of the observation, and instrument/telescope-specific data (see Section 3). The ASM code computes sky emission and transmission spectra. The wavelength grid of these spectra is provided by the ETC. Since 2015, the output files also include the radiance and transmission spectra of the individual components (see 3). The data returned to the

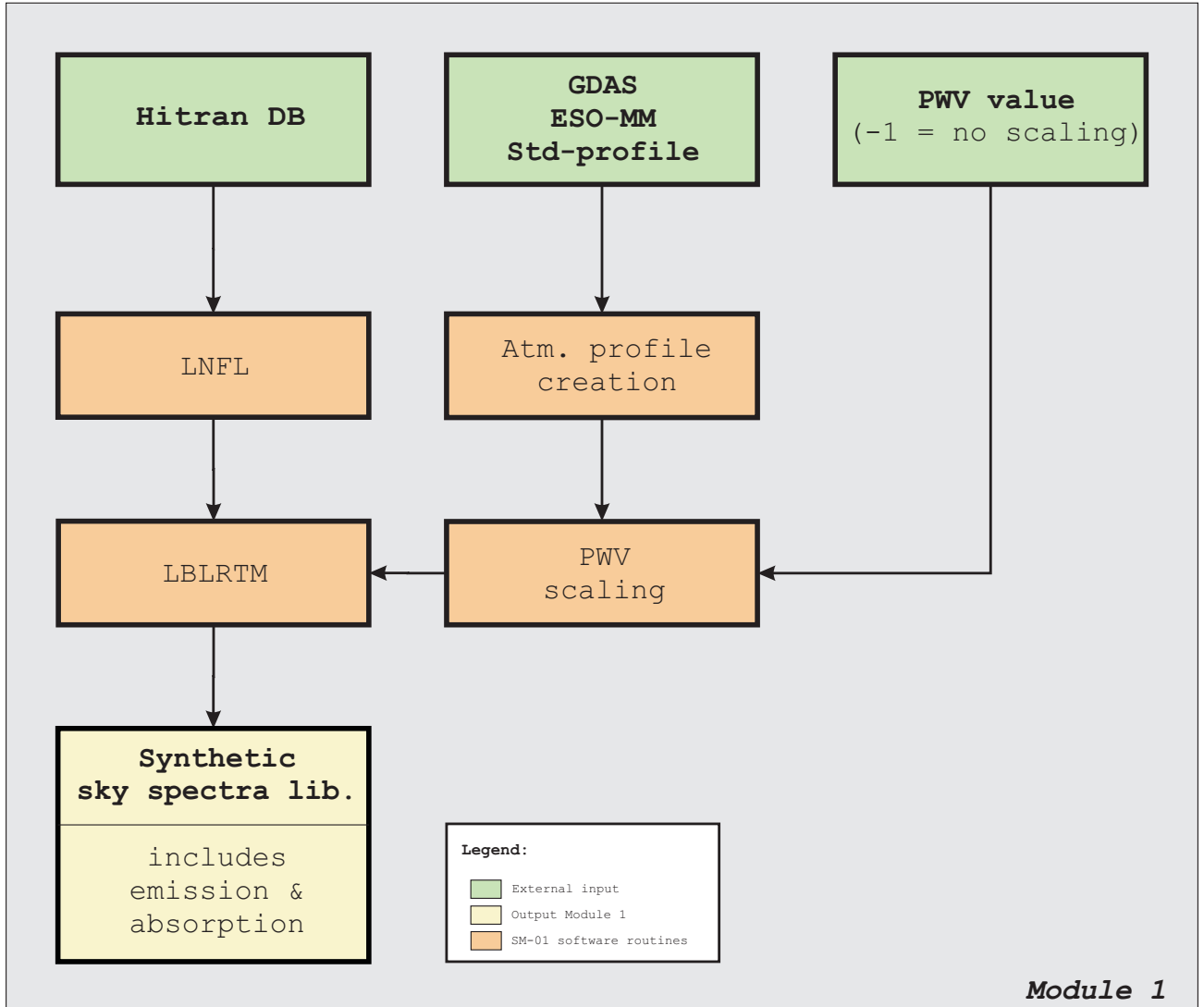


Figure 1: *Module 1*: This module creates a library of synthetic sky spectra on the basis of the HITRAN 2008 database and an atmospheric profile. The profile is created by merging the standard profile `equ.atm` (<http://www.atm.ox.ac.uk/RFM/>) and GDAS data (see [5] and Section 5), which provide information on temperature, pressure, and humidity of the selected observing site. Both, the HITRAN 2008 and the atmospheric profile, are used as input for the radiative transfer code LNFL/LBLRTM in order to calculate the sky spectrum.

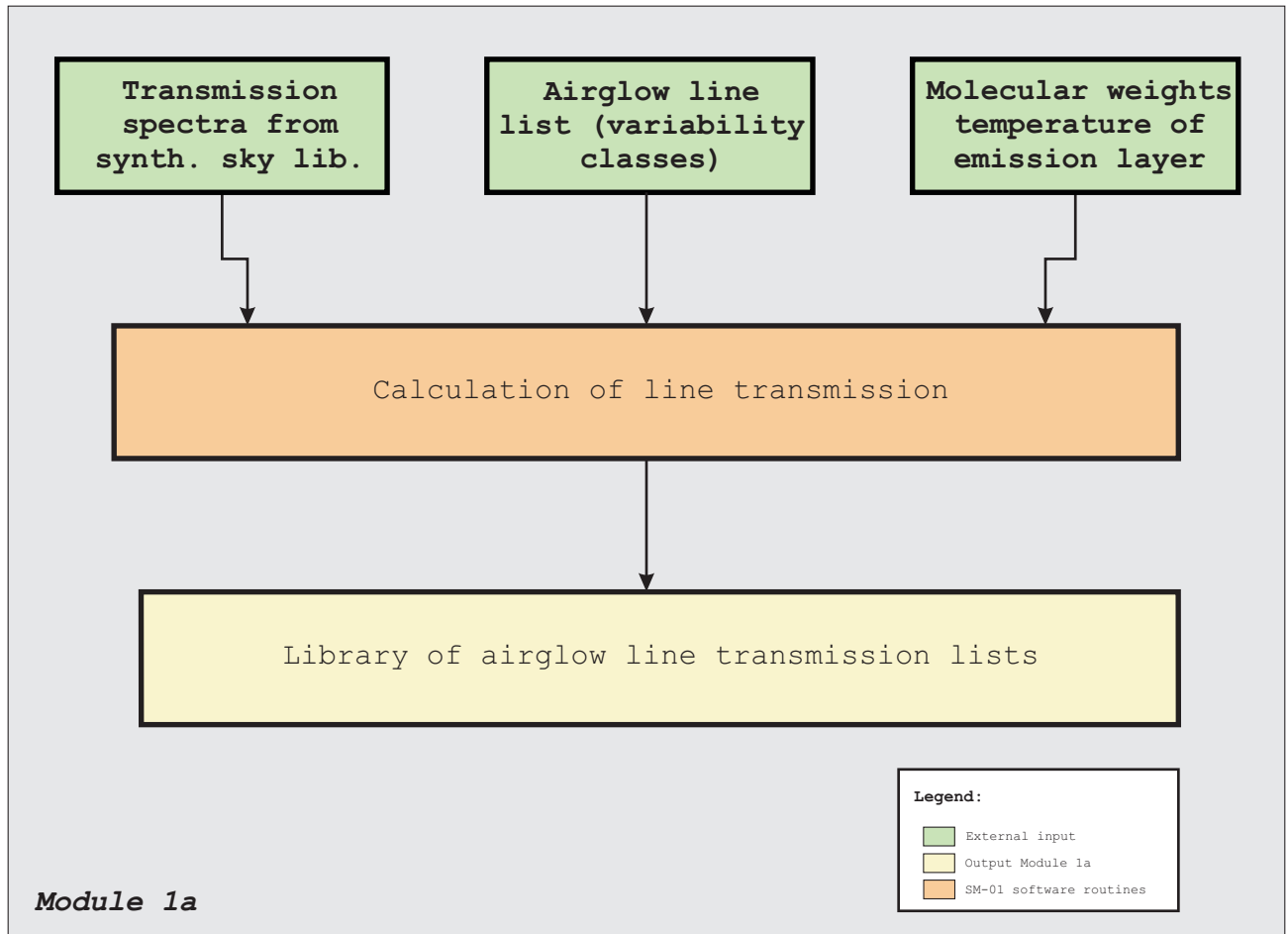


Figure 2: *Module 1a* calculates the individual airglow line transmission by means of the transmission spectra from the synthetic sky library, an airglow line list for the wavelengths, the line-dependent molecular weights, and the line-dependent emission layer temperatures.

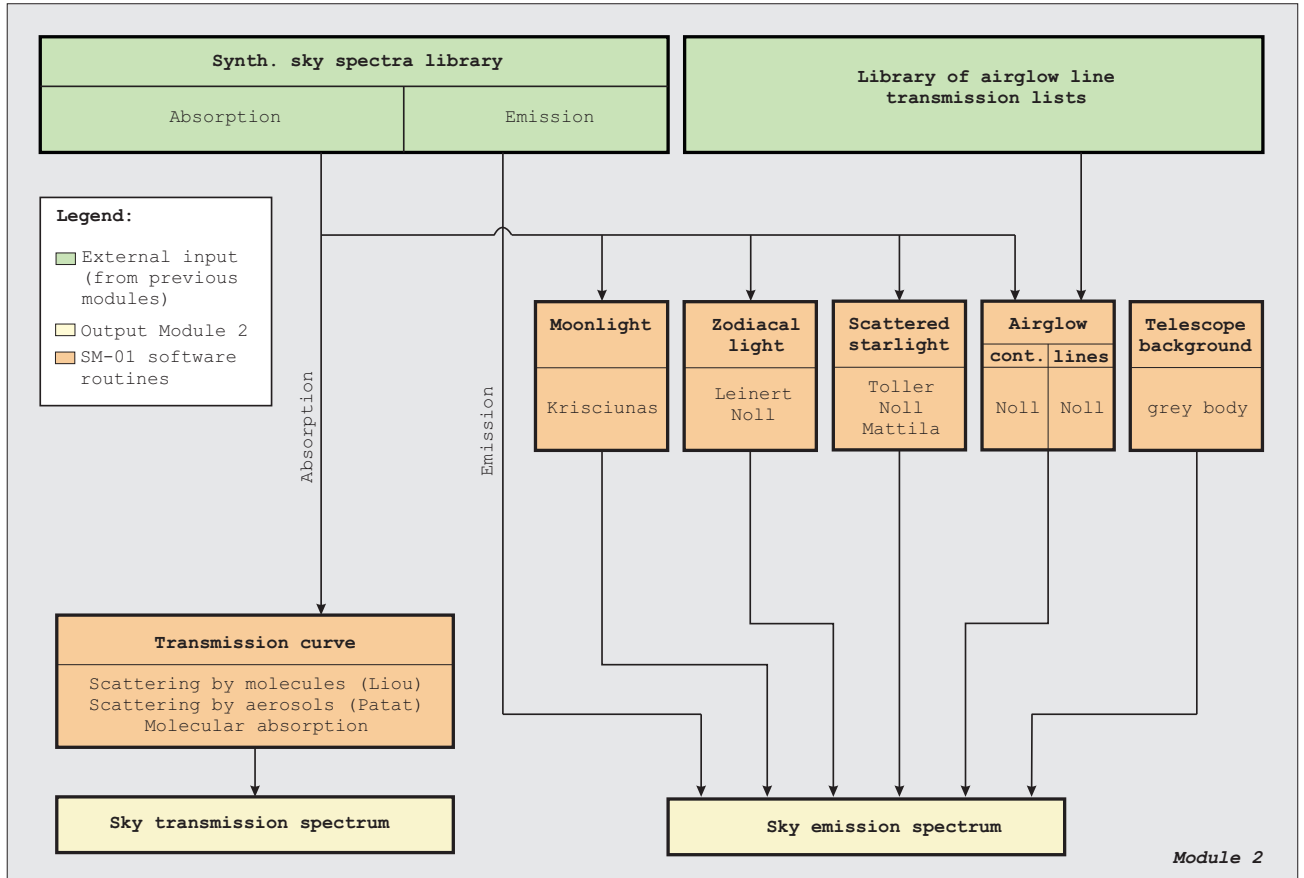


Figure 3: *Module 2* calculates the components, which need only minimal computing time. Hence, these components are computed during every ETC call. The final sky background spectrum is obtained by merging the appropriate synthetic sky spectrum from Module 1 (selected by user defined input) with these "fast" components.

ETC are *not* convolved with a user-provided kernel to reproduce the line-spread function of the desired set-up. The ETC performs this computation afterwards.

ESO	The Cerro Paranal Advanced Sky Model	Doc:	VLT-MAN-ESO-19550-5339
		Issue:	Issue 1.1.1
		Date:	Date 2013-09-18
		Page:	13 of 80

3 The ETC interface

The ASM code has been written in C using ESO's Common Pipeline Library (CPL). An ETC has to call the procedure `sm_etc_calcmodel` of Module 2 to compute the ASM. The following function declaration is used:

```
int sm_etc_calcmodel(cpl_table *skytable, const cpl_parameterlist *params)
```

The function returns 0 if no error occurred during execution.

The instrument-specific wavelength grid (in μm) is provided by the ETC via the CPL table `skytable` with only one column `lam`. In the process of running Module 2, `skytable` is extended with columns containing the sky emission spectrum in $\text{phot s}^{-1} \text{m}^{-2} \mu\text{m}^{-1} \text{arcsec}^{-2}$ (`flux`) and its -1σ and $+1\sigma$ flux uncertainties (`dflux1` and `dflux2`) and the transmission curve (`trans`) and its -1σ and $+1\sigma$ uncertainties (`dtrans1` and `dtrans2`).

The sources of the errors corresponding to the radiance/transmission spectrum are described in detail in Section 6. Together with the variation of the radiative transfer spectra (see also Section 5.4), all sources of error are added in quadrature using standard error propagation methods.

The CPL table `skytable` is also extended with columns containing spectra of the individual components contributing to the total radiance and transmission spectra.

- Radiance individual components
 - `flux_sml`: scattered moonlight
 - `flux_ssl`: scattered starlight
 - `flux_zl`: zodiacal light
 - `flux_tie`: thermal emission by telescope/instrument
 - `flux_tme`: molecular emission of lower atmosphere
 - `flux_ael`: sky emission lines of upper atmosphere
 - `flux_arc`: airglow continuum (residual continuum)
- Transmission individual components
 - `trans_ma`: molecular absorption
 - `trans_o3`: ozone UV/optical absorption
 - `trans_rs`: Rayleigh scattering
 - `trans_ms`: Mie scattering

The output spectra are *not* convolved to the instrumental resolution. This step is carried out by ETC routines.

The CPL parameter list `params` includes the input parameters necessary for running Module 2. They are provided by the ETC. Below, a complete list is given:

sm_h observatory height in km (default: 2.64)

sm_hmin lower height limit in km (default: 2.0)

alt altitude of object above horizon [0,90]

ESO	The Cerro Paranal Advanced Sky Model	Doc:	VLT-MAN-ESO-19550-5339
		Issue:	Issue 1.1.1
		Date:	Date 2013-09-18
		Page:	14 of 80

alpha separation of Sun and Moon as seen from Earth [0,360] (> 180 for waning Moon)

rho separation of Moon and object [0,180]

altnoon altitude of Moon above horizon [-90,90]

moondist distance to Moon (mean distance = 1; [0.91,1.08])

pres pressure at observer altitude in hPa (default 744)

ssa single scattering albedo for aerosols [0,1] (default 0.97)

calcds calculation of double scattering of moonlight ("Y" or "N") (default "N")

o3column relative UV/optical ozone column density (1 -> 258 DU)

moonscal scaling factor for scattered moonlight (current default 1, but see the note in Section 6.2.1)

lon_ecl heliocentric ecliptic longitude of object [-180,180]

lat_ecl ecliptic latitude of object [-90,90]

emis_str grey-body emissivity (comma-separated list starting with the first component in the light path)

temp_str grey-body temperature in K (comma-separated list starting with the first component in the light path)

msolflux monthly-averaged solar radio flux [sfu]

season bimonthly period (1: Dec/Jan, ..., 6: Oct/Nov.; 0: entire year)

time period of the night ($x/3$ of night, $x = 1,2,3$; 0: entire night)

vac_air vac[uum] or air wavelengths

pwv precipitable water vapour in mm. Currently, library spectra are provided for 0.5, 1.0, 1.5, 2.5, 3.5, 5.0, 10.0, and 20.0 mm. For all other values, the closest value of the previous list is taken. By default, the PWV is set to -1. In this case, the library spectrum for the given *season* parameter is used. The PWV value is then the mean value of the selected bimonthly period.

rtcode radiative transfer code L(BLRTM) for molecular spectra. Do not change.

resol resolution of molecular spectra in library (crucial for run time). Currently, the ASM software is delivered with three libraries calculated with three different spectral resolutions (R=60,000, R=300,000, R=1,000,000). If the value for the *resol* parameter does not match any of the resolutions of the available libraries, the next higher resolved one or the one with the highest available resolution is used.

filepath path to `sm_filenames.dat` for data paths and file names related to the required model data

incl inclusion of sky model components

format: "xxxxxx" where x = "Y" (yes) or x = "N" (no)

pos. 1: scattered moonlight

pos. 2: scattered starlight

pos. 3: zodiacal light

ESO	The Cerro Paranal Advanced Sky Model	Doc:	VLT-MAN-ESO-19550-5339
		Issue:	Issue 1.1.1
		Date:	Date 2013-09-18
		Page:	15 of 80

- pos. 4: thermal emission by telescope/instrument
- pos. 5: molecular emission of lower atmosphere
- pos. 6: sky emission lines of upper atmosphere
- pos. 7: airglow continuum (residual continuum)

More details on the required parameters are given in Section 6. As the input parameters are not completely independent, implausible parameter combinations can only be avoided by restricting the parameters to a limited set. Such parameter sets must be provided by the ETC. Moreover, a limited choice of parameter sets will also simplify the use of the ETC to an optimal extent.

ESO	The Cerro Paranal Advanced Sky Model	Doc:	VLT-MAN-ESO-19550-5339
		Issue:	Issue 1.1.1
		Date:	Date 2013-09-18
		Page:	16 of 80

ESO	The Cerro Paranal Advanced Sky Model	Doc:	VLT-MAN-ESO-19550-5339
		Issue:	Issue 1.1.1
		Date:	Date 2013-09-18
		Page:	17 of 80

4 Radiative transfer code

Currently, the radiative transfer code Line-By-Line Radiative Transfer Model (LNFL V2.6/LBLRTM V12.2) is used for calculating sky spectra. This code is widely used in atmospheric and climate research studies. This section gives an overview and is not intended to replace a full documentation. For more detailed information, the reader is referred to the sources given in the corresponding sections.

4.1 Line File / Line-By-Line Radiative Transfer Model (LNFL/LBLRTM)

LBLRTM is developed within the Radiative Transfer Working Group of the Atmospheric and Environmental Research Inc. (AER, see also Clough et al. [2005], [8], and [1]) and is publicly available. It can handle all molecules incorporated in the HITRAN database [4] and offers a wide range of possibilities to adjust input parameters (see [2] for more details).

The AER-code package used here consists of two programmes: (a) the "Line-File" `lnf1`, which extracts user selected spectral lines from the HITRAN database, and provides these in appropriate form as input for (b) the radiative transfer code `lblrtm`. For the ASM, the versions LNFL V2.6 and LBLRTM V12.2 have been used.

Some LBLRTM key features are (taken from [1]):

- the Voigt line shape is used at all atmospheric levels with an algorithm based on a linear combination of approximating functions;
- it has been and continues to be extensively validated against atmospheric radiance spectra from the ultra-violet to the sub-millimeter;
- it incorporates the self- and foreign-broadened water vapour continuum model, MT_CKD as well as continua for carbon dioxide, and for the collision induced bands of oxygen at 1600 cm^{-1} ($\lambda = 6.25\text{ }\mu\text{m}$) and nitrogen at 2350 cm^{-1} ($\lambda = 4.255\text{ }\mu\text{m}$);
- all parameters of the HITRAN line database are used including the pressure shift coefficient, the halfwidth temperature dependence, and the coefficient for the self-broadening of water vapour;
- a version of the Total Internal Partition Function (TIPS) programme is used for the temperature dependence of the line intensities;
- the effects of CO₂ line coupling are treated as first order with the coefficients for carbon dioxide generated from Niro et al. [2005];
- temperature-dependent cross section data such as those available with the HITRAN database may be used to treat the absorption due to heavy molecules, *e.g.* the halocarbons;
- an algorithm is implemented for the treatment of the variation of the Planck function within a vertically inhomogeneous layer as discussed in Clough et al. [1992];
- algorithmic accuracy of LBLRTM is approximately 0.5% and the errors associated with the computational procedures are in the order of five times less than those associated with the line parameters so that the limiting error is that attributable to the line parameters and the line shape;

ESO	The Cerro Paranal Advanced Sky Model	Doc:	VLT-MAN-ESO-19550-5339
		Issue:	Issue 1.1.1
		Date:	Date 2013-09-18
		Page:	18 of 80

- its computational efficiency mitigates the computational burden of the line-by-line flux and cooling rate calculation (Clough et al. [1992]), for example linear algebraic operations are used extensively in the computationally intensive parts of LBLRTM so that vectorisation is particularly effective with a typical vectorised acceleration of 20;
- FFT instrument function with a choice of 9 apodisation functions;
- includes a realistic spectral sea surface emissivity model in the infrared (Masuda et al. [1988]; Wu&Smith [1997]);
- input atmospheric profiles in either altitude or pressure coordinates;
- interfaces with other radiative transfer models (like RRTM), and also the forward model for inversion algorithms (*e.g.* Tropospheric Emission Spectrometer (TES) and Infrared Atmospheric Sounding Interferometer (IASI));
- these attributes provide spectral radiance calculations with accuracies consistent with the measurements against which they are validated and with computational times that greatly facilitate the application of the line-by-line approach to current radiative transfer applications.

4.2 Line input sources

For calculating the spectra, two different sources for the lines of the molecules were used (see Table 1 for an overview):

- HITRAN database [4]: The HITRAN 2008 database currently provides spectral information for 39+3 molecules. In total 2,713,968 spectral lines are included, the majority is based on modelled data.
- LNFL/LBLRTM provides a specific line database (`aer_<version>`), which is based on HITRAN 2008. However, noticeable modifications were made with respect to H₂O, CO₂, CH₄, and O₂ [9]. Thus, this line database is used as default for LNFL/LBLRTM.

However, only those 30 molecules are taken into account, which are present in the atmospheric standard profile. Table 4.2 provides an overview of all molecules (a) based on the HITRAN, (b) contained in the standard atmospheres (Column 4), and (c) known by LBLRTM (Column 5).

ESO	The Cerro Paranal Advanced Sky Model	Doc:	VLT-MAN-ESO-19550-5339
		Issue:	Issue 1.1.1
		Date:	Date 2013-09-18
		Page:	19 of 80

Table 1: List of molecules based on the HITRAN database.

# of molecule	molecule	alt. name	std. atmosphere	LBLRTM
1	H ₂ O	Water	X	X
2	CO ₂	Carbon dioxide	X	X
3	O ₃	Ozone	X	X
4	N ₂ O	Nitrous oxide	X	X
5	CO	Carbon monoxide	X	X
6	CH ₄	Methane	X	X
7	O ₂	Oxygen	X	X
8	NO	Nitric oxide	X	X
9	SO ₂	Sulfur dioxide	X	X
10	NO ₂	Nitrogen dioxide	X	X
11	NH ₃	Ammonia	X	X
12	HNO ₃	Nitric acid	X	X
13	OH	Hydroxyl		X
14	HF	Hydrogen fluoride		X
15	HCl	Hydrogen chloride		X
16	HBr	Hydrobromic acid		X
17	HI	Hydrogen iodide		X
18	ClO	Chlorine monoxide	X	X
19	OCS	Carbonyl sulfide	X	X
20	H ₂ CO	Formaldehyde		X
21	HOCl	Hypochlorous acid	X	X
22	N ₂	Nitrogen	X	X
23	HCN	Hydrogen cyanide	X	X
24	CH ₃ Cl	Chloromethane		X
25	H ₂ O ₂	Hydrogen peroxide	X	X
26	C ₂ H ₂	Acetylene	X	X
27	C ₂ H ₆	Ethane	X	X
28	PH ₃	Phosphine		X
29	COF ₂	Carbonyl fluoride	X	X
30	SF ₆ q	Sulfur hexafluoride	X	X
31	H ₂ S	Hydrogen sulfide		X
32	HCOOH	Formic acid		X
33	HO ₂	Hydroperoxy		X
34	O	Oxygen		X
35	ClONO ₂ q		X	X
36	NO+	Nitrosonium		X
37	HOBr			X
38	C ₂ H ₄	Ethylene		X
39	CH ₃ OH	Methanol		X
40	BrO			X
41	C ₃ H ₈	Propane		X
42	C ₂ N ₂	Cyanogen		X

ESO	The Cerro Paranal Advanced Sky Model	Doc:	VLT-MAN-ESO-19550-5339
		Issue:	Issue 1.1.1
		Date:	Date 2013-09-18
		Page:	20 of 80

5 Atmospheric profiles and meteorological data

Information concerning the composition of the atmosphere is available at various levels. To the end of creating a uniform profile with the variables temperature, pressure, and density of various molecular species as a function of geoelevation, three sources of input are merged: standard profile, GDAS profile, and ESO meteo monitor (EMM) data.

The largest amount of molecular density information is contained in the atmospheric standard profile. However, it is only available for a specific geographical latitude and does not contain any time information whatsoever (see Section 5.1). To compensate the lack of time information, one can rely on the EMM. It provides the most frequent updates and is specific to the selected observing site (see Section 5.3). Unfortunately, it cannot provide molecular species information apart from water vapour (relative humidity measurements) and is restricted to a local on-site measurement, *i.e.* a single geoelevation data point only. To bridge the gap between these two data sources, GDAS provides a global grid of profile measurements (with approximate grid spacing of 110 km) to an altitude of ~ 26 km with updates every three hours. GDAS does not contain molecular species apart from H₂O, though (see Section 5.2).

These three data sources and the required processing for use with the spectra library are described in detail below.

5.1 Atmospheric standard profile

The atmospheric standard profiles provide the basis for the model atmosphere used for any calculations in Module 1 including information on pressure, temperature and molecular abundance as function of height (121 levels in the range 0–120 km). Standard profiles provided by the homepage of the atmospheric radiative transfer code ‘Reference Forward Model’ RFM [10] are available for mid-latitude (Lat = 45°, both, day and night), polar winter/summer (Lat = 75°), and equatorial day-time regions. For the included molecules, see Table 1. Apart from these data, less resolved profiles (a tropical, sub-arctic summer/winter and a US standard profile) are available with 50 geoelevation layers including the molecules H₂O, CO₂, O₃, N₂O, CO, CH₄, and O₂ only.

For estimating the possible differences in the output spectra by different standard profiles, the equatorial day-time `equ.atm` and the mid-latitude profile `ngt.atm`, corresponding to a latitude Lat = 45°, are compared. The location of Cerro Paranal (Lat = 24.6°) is between these two profiles. In Figure 4, both profiles are shown. Although the distribution of several molecules (*e.g.* N₂, O₂, CO₂) does not vary, significant differences between the two profiles are visible. To investigate the impact of the input profile differences on the output spectra, LBLRTM was run with the same input parameters, but with varying standard profiles. Calculating broad-band ratios in the main filter ranges $UBVRI_cJHKLMN$ indicates deviations of less than 2% for the radiance and transmission spectra (see Table 2). Hence, one can conclude that the differences between the two standard atmospheric profiles are negligible at this stage. Following a recommendation by Anu Dudhia [Anu Dudhia 2009, priv.comm.], the author of the RFM code, the equatorial profile `equ.atm` was used for the creation of the library.

The ozone profile is slightly modified following Patat et al. [2011], who found a discrepancy between the measured O₃ column density (258 DU¹) and the corresponding column density derived from the standard profile (238.8 DU). Thus, a correction factor of 1.0805 is applied to the O₃ profile. In addition, the CO₂ abundance

¹Dobson Unit (DU): 1 DU = 2.69×10^{16} molecules cm⁻²

ESO	The Cerro Paranal Advanced Sky Model	Doc:	VLT-MAN-ESO-19550-5339
		Issue:	Issue 1.1.1
		Date:	Date 2013-09-18
		Page:	21 of 80

is multiplied by 1.06 due to the creation of the `equ.atm` standard profile in 2001 and the continuing anthropogenic emissions (see WMO Greenhouse Gas Bulletin [WMO12]). This correction leads to a carbon dioxide abundance of 391 ppmv at ground, which corresponds to the global mean value in 2011.

Table 2: Broad band comparison of the relative ratios between the `equ.atm` and the `ngt.atm` atmospheric standard profiles.

Filter	λ_{\min} [μm]	λ_{\max} [μm]	Radiance ratio [%]	Transmission ratio [%]
<i>U</i>	0.33	0.40	0.02	0.06
<i>B</i>	0.39	0.50	0.00	0.02
<i>V</i>	0.50	0.60	0.14	0.56
<i>R</i>	0.58	0.82	0.05	0.28
<i>I_c</i>	0.73	0.85	0.01	0.04
<i>J</i>	1.10	1.34	-0.00	-0.00
<i>H</i>	1.50	1.80	-0.00	-0.01
<i>K</i>	2.00	2.40	-0.05	-0.06
<i>L</i>	3.56	4.12	-0.00	-0.05
<i>M</i>	4.52	4.96	-0.69	1.37
<i>N</i>	7.40	13.60	-0.60	1.39

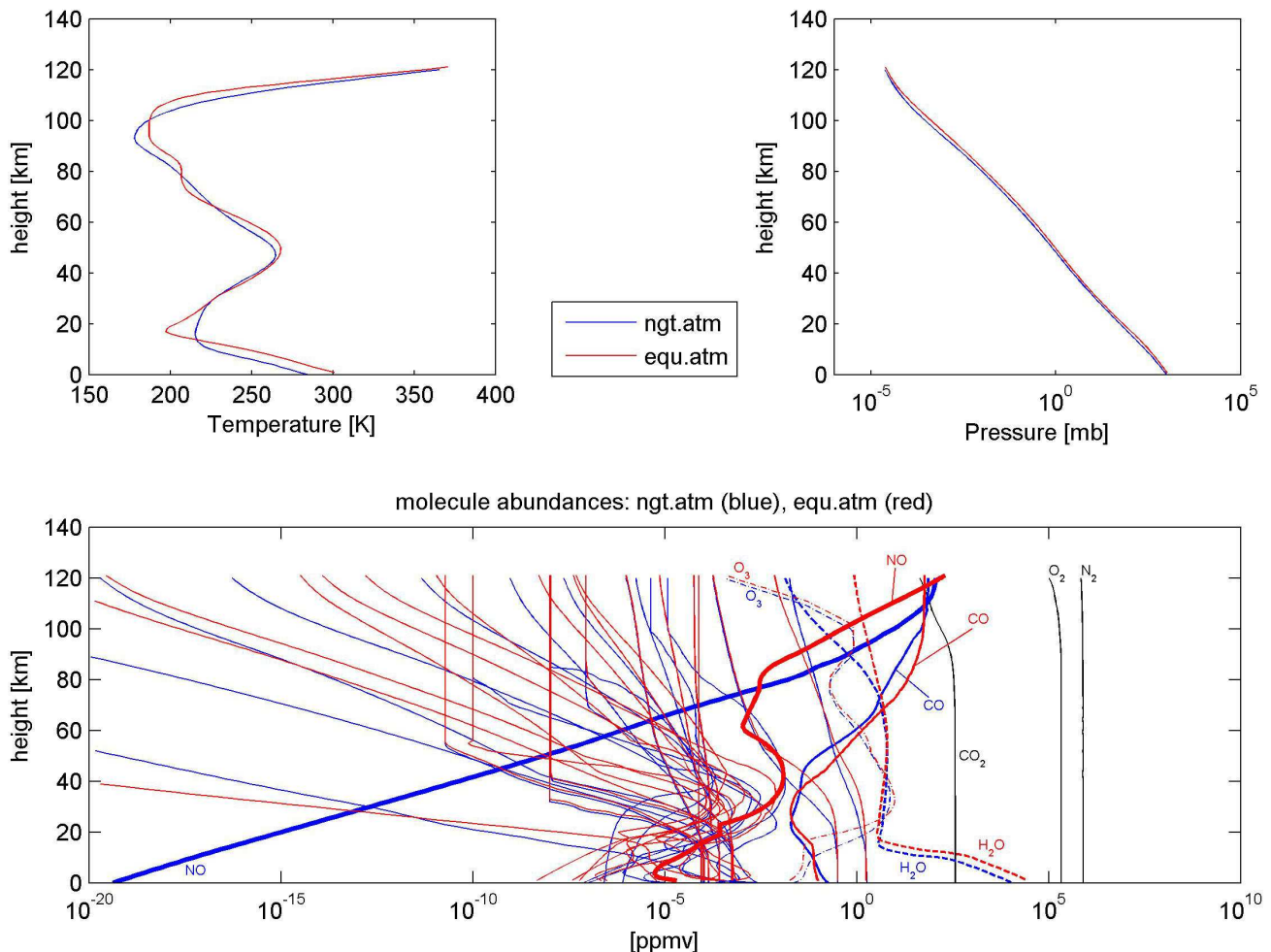


Figure 4: Comparison of the equatorial (equ.atm) and the mid-latitude night time atmospheric profile (ngt.atm). Red lines correspond to the equatorial, blue lines to the mid-latitude profile.

ESO	The Cerro Paranal Advanced Sky Model	Doc:	VLT-MAN-ESO-19550-5339
		Issue:	Issue 1.1.1
		Date:	Date 2013-09-18
		Page:	23 of 80

5.2 GDAS profiles

The GDAS (Global Data Assimilation System) data provided by NOAA are a model based set of meteorological data dedicated to weather forecast studies. The models are archived by the ARL (Air Resources Library) on a 3 hour basis, as a global, 1 degree latitude/longitude data set (requiring bilinear interpolation for Cerro Paranal) based on pressure surfaces (from Dec. 2004 to present and ongoing). Apart from various meteorological parameters for the surface, vertical profiles for 23 pressure levels ranging from 0 to about 26 km are provided for the geopotential height, temperature, relative humidity, and wind components for three dimensions (not used for the ASM). An example is shown in Figure 5.

#	P [hPa]	HGT [km]	T [K]	RELHUM [%]
903	0.971	294.5	49.9	
900	0.976	295.8	35.5	
850	1.467	293.7	30.9	
800	1.985	291.0	29.8	
750	2.533	288.2	27.4	
700	3.112	284.5	26.0	
650	3.726	280.7	18.8	
600	4.379	276.2	11.4	
550	5.077	271.4	8.7	
500	5.827	266.0	7.5	
450	6.638	259.9	7.5	
400	7.522	252.7	10.5	
350	8.494	244.7	25.1	
300	9.578	236.0	53.4	
250	10.813	227.0	66.5	
200	12.267	218.8	37.7	
150	14.069	209.2	17.3	
100	16.489	200.3	32.4	
50	20.571	206.1	0.0	
20	26.324	221.4	0.0	

Figure 5: *GDAS profile* with columns for pressure, geoelevation, temperature, and relative humidity.

5.3 ESO meteo monitor (EMM)

The ESO meteo monitor (EMM) provides information on the local meteorological conditions at the ESO sites La Silla and Cerro Paranal. The data at Cerro Paranal are taken by a local meteorological station mounted on a 30 m high mast installed in October 1984 [11]. This station provides the following meteorological information on a 20 min average basis:

```
s1,d1 = wind speed (m/s) and direction (0=North, 90=East..)
        at 10m above ground (30m from 1998 onwards)
rh = relative humidity (%) at 2m above ground
t1 = air temperature (Celsius) at 2m above ground
```

ESO The Cerro Paranal Advanced Sky Model	Doc: VLT-MAN-ESO-19550-5339 Issue: Issue 1.1.1 Date: Date 2013-09-18 Page: 24 of 80
---	--

p = pressure (mb) at 2m above ground

td = dew point temperature (C) computed from rh and t1

Starting from January 1st 1985 currently ~ 400 000 data points are measured with the following accuracy [11]:

wind direction: ~5.63deg
wind speed: ~2% over 10m/s
temperature: ~0.1deg
humidity: linearity about 1%
seeing: better than 10% above 0.25 arcsec

The data can be retrieved online² on a daily basis or as download provided by M. Sarazin³, and are cumulatively shown in Figure 6. Thus, for any requested average time interval, like e.g. December and January, ample measurements are available. In compiling these data care has to be taken to remove bad measurements before further processing.

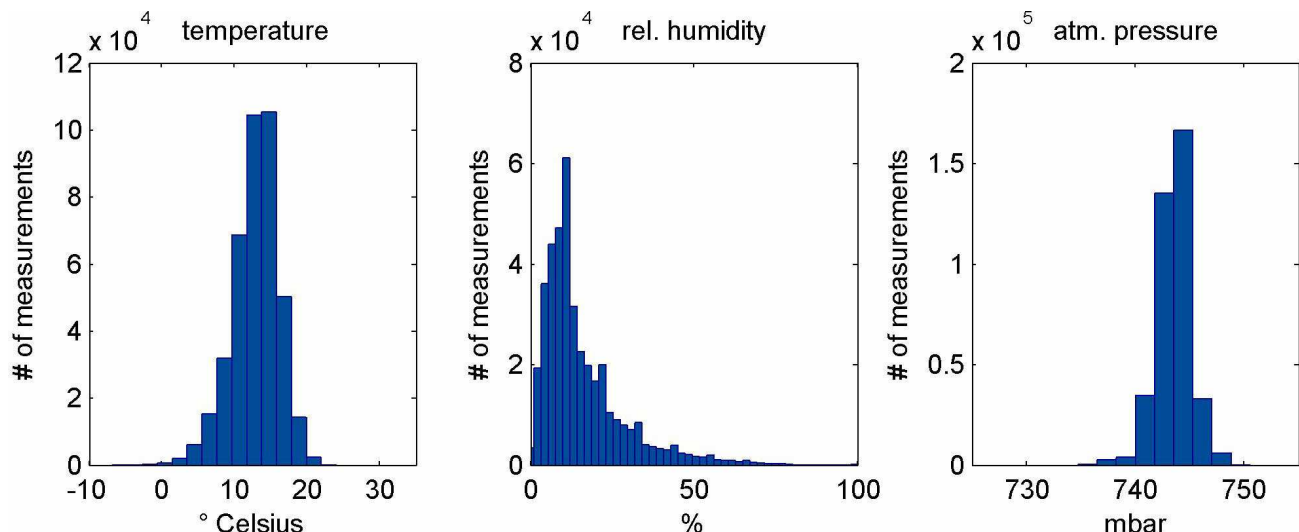


Figure 6: Histograms of EMM data (from Jan. 1985 to Jan. 2008). *Left panel:* temperature; *middle panel:* relative humidity; *right panel:* pressure.

²<http://archive.eso.org/asm/ambient-server>

³<http://www.eso.org/gen-fac/pubs/astclim/paranal/database/>

ESO	The Cerro Paranal Advanced Sky Model	Doc:	VLT-MAN-ESO-19550-5339
		Issue:	Issue 1.1.1
		Date:	Date 2013-09-18
		Page:	25 of 80

5.4 GDAS profile library

The computation of a full sky spectrum ($\lambda = 0.3 - 30.0 \mu\text{m}$) with LBLRTM takes a considerable amount of time, in the order of 10 to 90 minutes on a standard PC. Thus, calculating a spectrum (or even a subsection of the full wavelength range) becomes infeasible for an online ETC application. The best approach to tackle this problem is to compute a full set of spectra ahead of time for a specified set of environmental conditions and to extract the best-matching section of one such spectrum in reply to an online ETC request.

In order to prepare such a spectra library educatedly, analysis of the importance of various influencing properties is important and a procedure for estimating the error potential of a given configuration is required. The variation of the resulting spectra is characterised by calculating the scatter of all input atmospheric profiles contributing to a specific library spectrum and computing the average profiles at $\pm 1\sigma$ of the distribution of contributing data points at a given altitude for a specific atmospheric data set. With the $\pm 1\sigma$ atmospheric profiles, “error” spectra are calculated, which specify the $\pm 1\sigma$ bandwidth of the library spectra. In the process of composing those error profiles, a special fitting procedure is used to take the strongly asymmetric shapes of the profile distributions into account. The averaging process, the incorporation of the EMM data, and the calculation of the error estimates will be described in detail in the next section.

As the variation of the atmospheric profiles is realised through introduction of the EMM and GDAS data, the crucial ingredients determining the time variability of the resulting spectra are the shapes of the pressure, temperature, and humidity profiles as a function of time/date.

There are mainly two time scales which dominate the variation of the GDAS profiles. On a short scale, the “weather” varies in the course of the night, *e.g.* the temperature drops; on a longer scale the GDAS profile will vary with the season over the course of one year. A compromise between a fine grid and enough statistical significance is achieved by dividing the night into three time bins (dusk, midnight, dawn) and the year in two-month bins (December/January, February/March, ...).

In the following, several statistics will be employed for evaluating the deviations of the “error” spectra from the “mean” spectra.

Spectra resulting from computing the smallest unit, *e.g.* December/January midnight, are shown in Figure 7. For such a single library spectrum the continuum values of the radiance spectra can vary by 100% to more than 300%. Moreover, the lines deviate from the continuum by factors of up to 6 or more. The lines in the transmission spectrum are not as strongly affected. However, they still vary by factors of 1-2. Only the transmission continuum is mostly stable (up to 10% deviation). However, this results from the fact that the continuum values cluster around unity, which follows from the atmosphere being mostly transparent across the spectral windows shown here. In Figure 8 the corresponding GDAS profiles are shown. By far the largest percentual scatter arises from the change in relative humidity.

In order to quantify the impact of the variation of the atmospheric conditions in the course of a night, the mean spectra for the beginning and the end of the night are compared (see Figure 9). The radiance continuum varies only by 10-20%. In the lines for both radiance and transmission, the variation ranges from 20-60%. As expected, the transmission continuum is practically unaffected. The corresponding GDAS profiles are compared in Figure 10. The change during a night in pressure and temperature is totally negligible in comparison to the variation of the relative humidity (less than 1% compared to up to 500%).

The seasons (see Figure 11) cause a variation of the radiance continuum by 40-70%. However, strongest affected are the lines in the radiance spectra: between 20-200%. In transmission, the values are 10-50% for the lines and

ESO	The Cerro Paranal Advanced Sky Model	Doc:	VLT-MAN-ESO-19550-5339
		Issue:	Issue 1.1.1
		Date:	Date 2013-09-18
		Page:	26 of 80

less than 2% for the continuum. Note that the data are summed over a whole night, thus each curve is composed of three times more data than the previous plots. Figure 12 shows the corresponding GDAS profiles. In contrast to the variation across a single night, the changes of the GDAS profiles across the year are more significant. The pressure decreases by more than 3% at an altitude of ~ 15 km in June/July winter compared to summer. Furthermore, the temperature profile exhibits an inversion at ~ 15 km altitude. In winter, temperatures are lower than in summer at lower altitudes, and vice versa at higher levels. The relative humidity profile has the same overall shape in both seasons, but is compressed to lower altitudes in winter, resulting in lower ground humidity values than in summer.

In order to quantify the response of the scatter of the spectra corresponding to one library data point to increasing the number of input GDAS profiles, the “error” and “mean” spectra for a whole night, *i.e.* summing the data for evening, midnight, and morning, are inspected (see Figure 9). In the majority of cases, a significant decrease of the scatter is observed. In the cases where it increases, the value of the increase is small. In particular, the radiance spectra profit substantially from the better statistics. Figure 14 shows the corresponding GDAS profile. Apart from the relative humidity, no significant change is apparent. Relative humidity exhibits a decrease of $\sim 30\%$ at altitudes below 3 km when averaging over the whole night.

To separate the influence of the various ingredients, special error profiles were created that only include the variation of a single quantity, like *e.g.* pressure. Exemplary, the data for December/January, whole nights, averaged over several years will be used. Figure 15 shows the evaluated atmospheric profiles. While pressure and temperature both vary only by $\pm 1\%$, the relative humidity changes dramatically (by $\pm 100 - 400\%$).

The results from evaluating the spectra obtained from running the code with these profiles in the four spectral windows ($\sim 0.7 \mu\text{m}$, *K*-band, $\sim 9 \mu\text{m}$, $\sim 3.3 \mu\text{m}$) are shown in Figures 16 to 18. Varying the pressure has very little effect. The continuum is systematically shifted by only 0.2% in both radiance and transmission, while some lines deviate by up to 8%. However, the picture changes dramatically for the temperature (see Figure 17). Interestingly, temperature mostly affects the radiance continuum in contrast to the pressure (+10/-10% to +100/-50%). Few lines both in radiance and transmission show deviations exceeding $\pm 20 - 30\%$. The transmission continuum is mostly unaffected (less than 0.6%). The most critical parameter is relative humidity (see Figure 18). While lower deviations of the radiance continuum never exceed -40%, the upper variation reaches more than 100%. To an even larger extent, lines in the radiance and transmission spectra are affected by 30-370%. However, the transmission continuum remains almost unchanged (changed by a few per cent at most).

In conclusion, the impact of the variation across a single night must be valued as only marginally significant compared to the overall variation of all spectra corresponding to a single data point in the spectra library. For this reason and keeping in mind the targeted use of this module as an ETC application, in the following, the library will be reduced to spectra summing up all the data across a whole night, *i.e.* beginning, midnight, and morning data. However, the variation across seasons is not as insignificant. As seasons can be incorporated easily during the planning of the observations even at the proposal stage, at least in some applications, it is prudent to include this parameter as an option in the library.

Relating the input GDAS profiles to the resulting spectra, it is interesting to note several issues. Both temperature and pressure vary only by a relatively small amount ($\sim 1\%$). Yet, temperature has a much larger impact on the resulting spectra than pressure. In fact, the pressure dependence is so weak that it can be neglected altogether (at least in environments similar to Cerro Paranal). Furthermore, relative humidity shows an extremely large scatter in the GDAS profiles and, therefore, dominates the “error” budget of the sky background spectra.

ESO	The Cerro Paranal Advanced Sky Model	Doc:	VLT-MAN-ESO-19550-5339
		Issue:	Issue 1.1.1
		Date:	Date 2013-09-18
		Page:	27 of 80

In addition to the aforementioned weather dependent quantities, the by the ETC requested atmospheric sky spectrum is also influenced by the elevation of the target, *i.e.* the airmass. Therefore, the airmass parameter space will be quantised in steps of 0.5 for the interval from 1 to 3.

Thus, the resulting library will consist of $(6+1) \times 5 = 35$ combinations, for the two-month/year (6+1) and airmass (5) bins, respectively. The additional bin in season results from summing the data over a whole year, which is useful when a specific ETC forecast period cannot be given (see also Section 5.7 for another application). Each library spectrum encompasses a time window of several GDAS profiles, which must be averaged to obtain meaningful profiles representing a specific bin. Furthermore, the library will have to be computed for the $\pm 1\sigma$ GDAS/EMM profiles to obtain an “error” estimate for the scatter of the data distribution. In total, the library will contain $35 \times 3 = 105$ computations with LBLRTM stored in 70 library files (one file for transmission and radiance each; three computations per bin for the “mean” and the two “error” spectra).

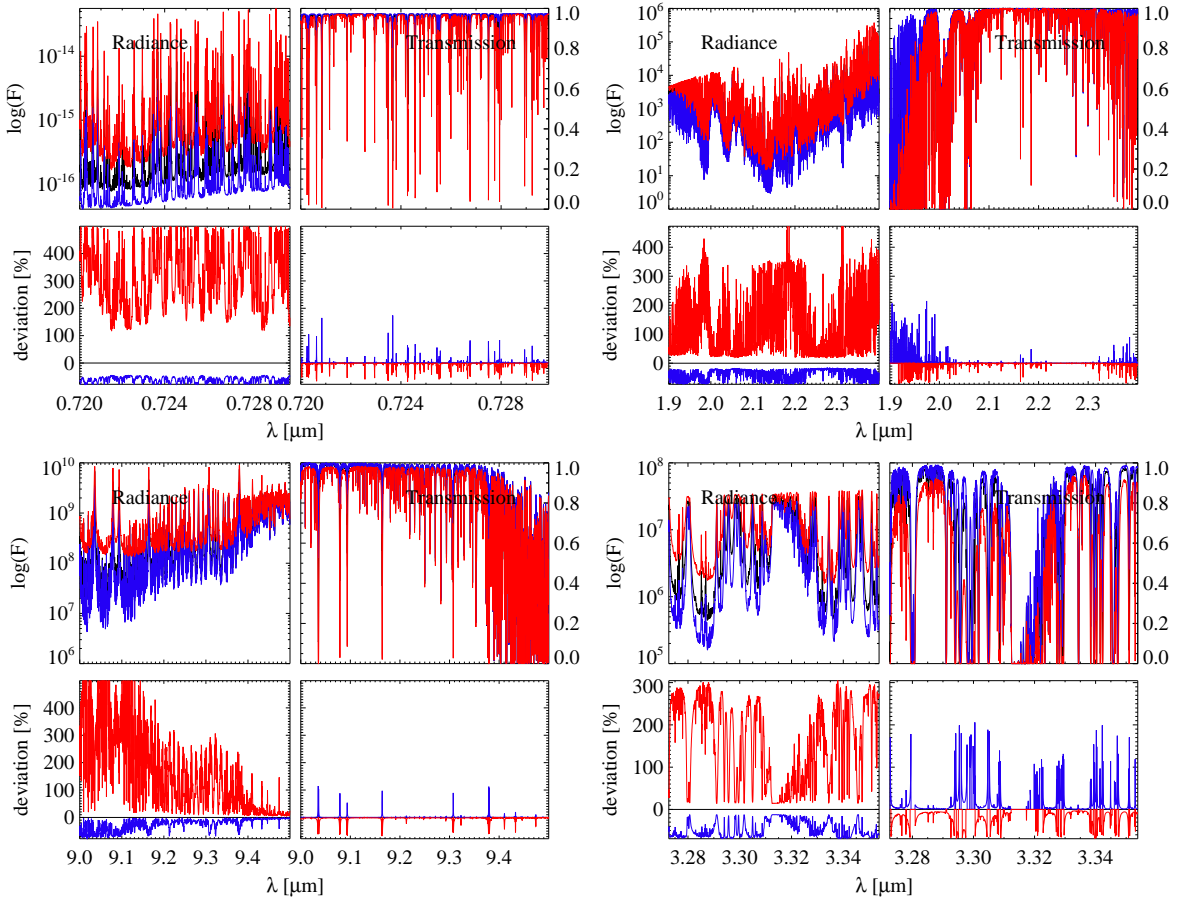


Figure 7: *Spectra for December/January midnight*: Each of the four panels shows a different spectral window ($\sim 0.7 \mu\text{m}$, K -band, $\sim 9 \mu\text{m}$, $\sim 3.3 \mu\text{m}$; from top left, clockwise). The panels display radiance (left half) and transmission spectra (right half). The top rows show the emission (in flux units) and transmission spectra, while the bottom rows indicate the relative deviation of the plus/minus spectra from the mean. Blue, red, and black curves show the negative and positive error spectra and the mean spectrum, respectively.

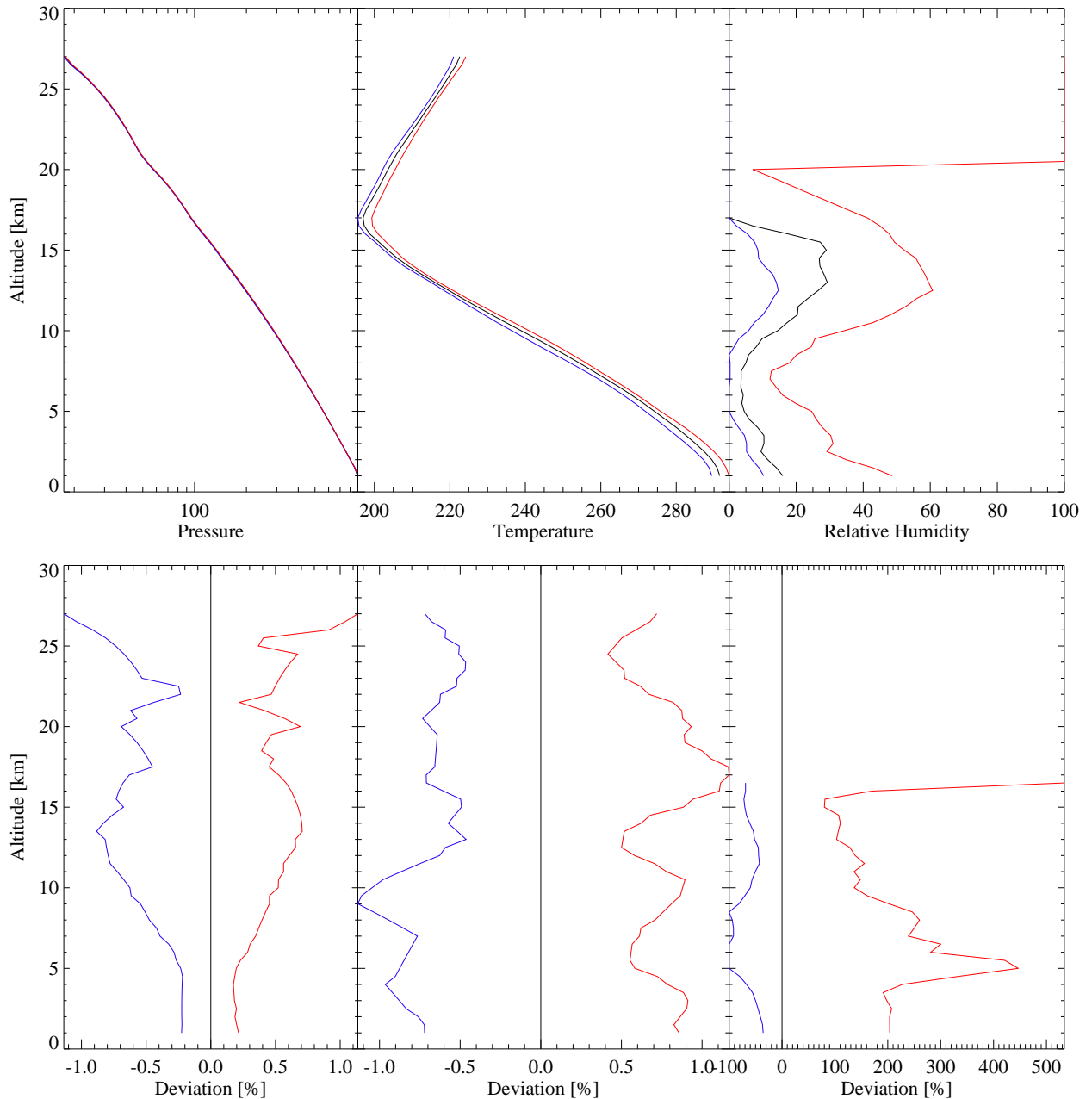


Figure 8: *GDAS profile for December/January midnight*: The six panels show data for pressure, temperature, and relative humidity (columns from left to right). The top row displays GDAS profiles, while the bottom row shows percentual $\pm 1\sigma$ deviations from the mean profile. Red, black, and blue lines symbolise the -1σ , average and $+1\sigma$ values, respectively.

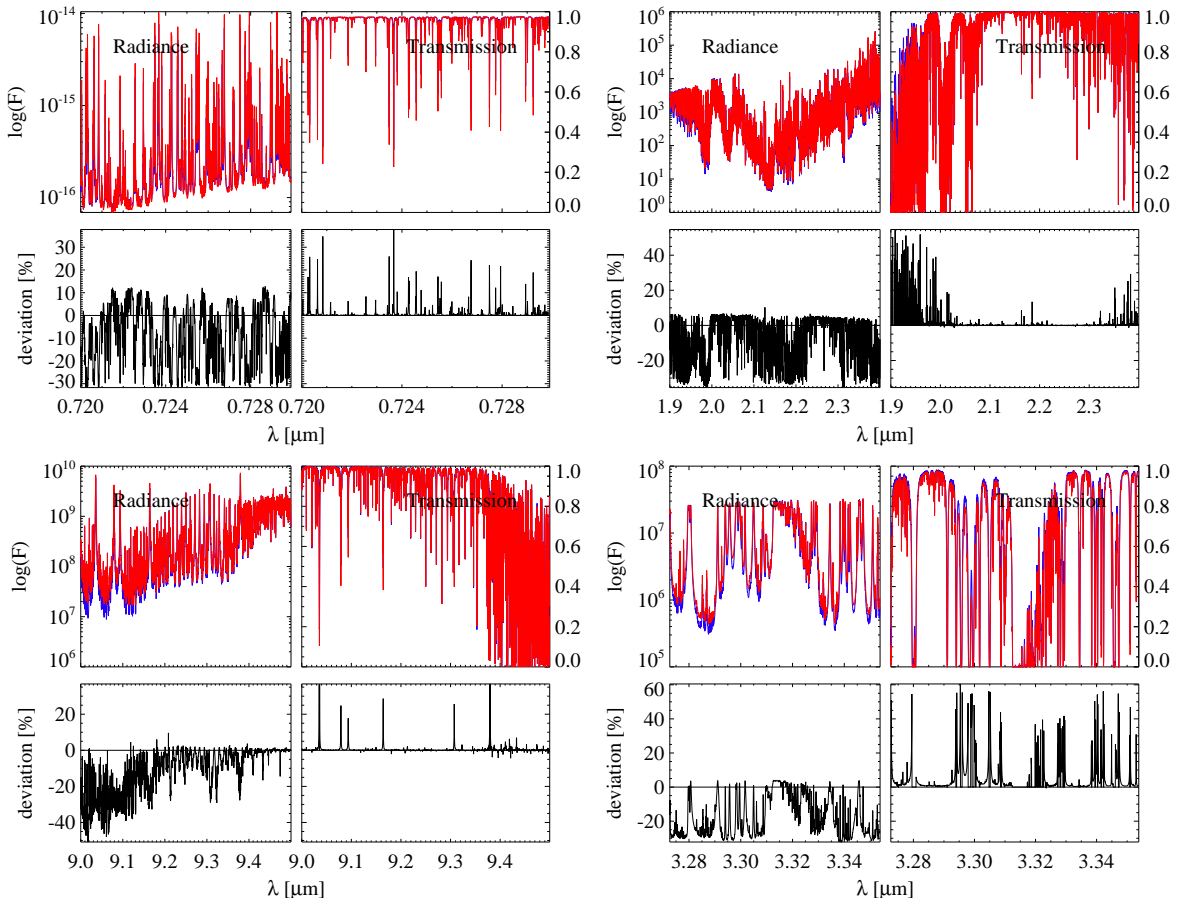


Figure 9: *Spectra for December/January evening and morning:* Spectra represent the difference between the values of the spectra for the beginning and end of the same night. Each of the four panels shows a different spectral window ($\sim 0.7 \mu\text{m}$, K -band, $\sim 9 \mu\text{m}$, $\sim 3.3 \mu\text{m}$; from top left, clockwise). The panels display radiance (left half) and transmission spectra (right half). The top rows show the emission (in flux units) and transmission spectra, while the bottom rows indicate the relative deviation of the plus/minus spectra from the mean. Blue, red, and black curves show the evening and morning spectra and the deviation, respectively.

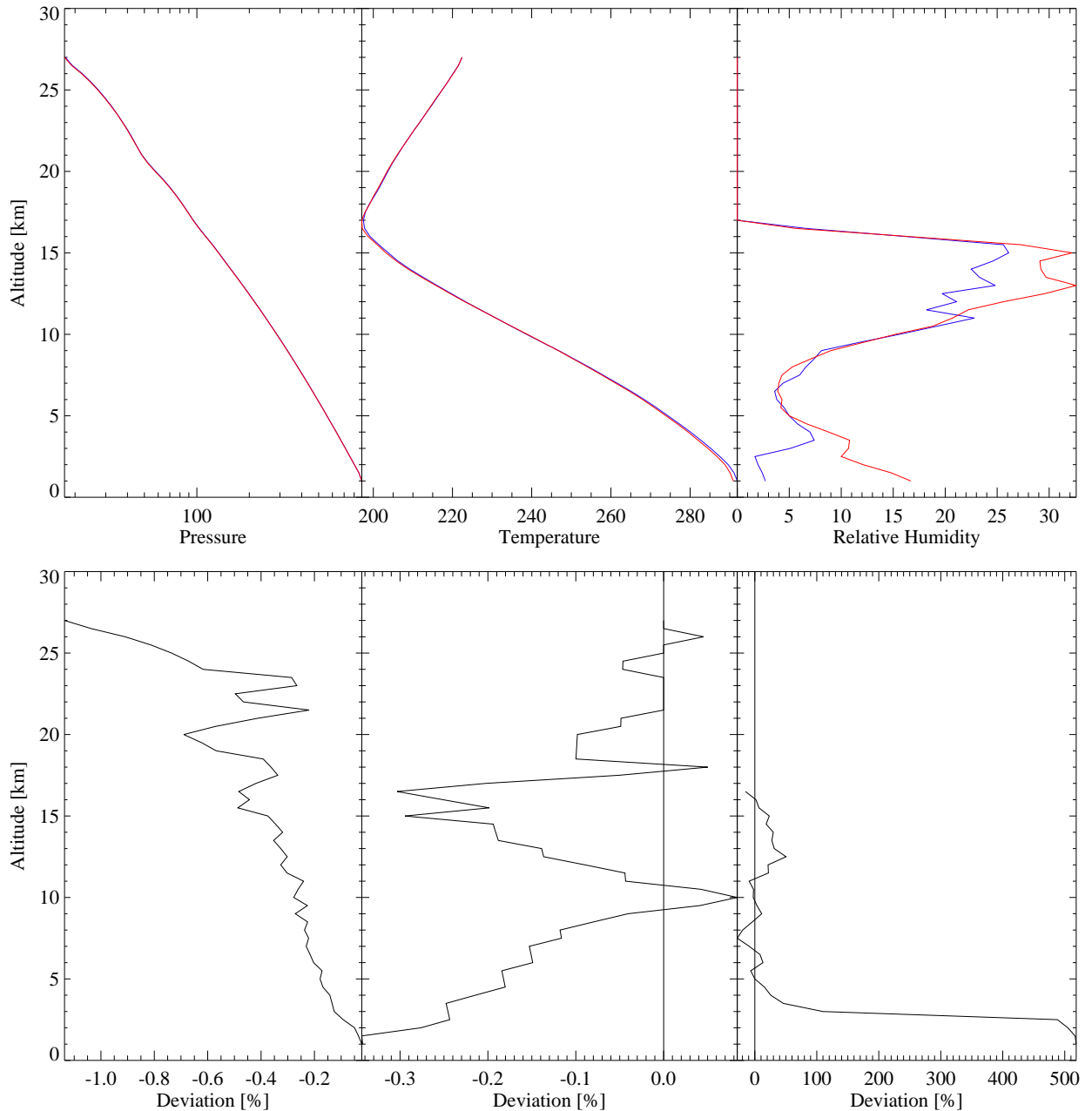


Figure 10: *GDAS profiles for December/January evening and morning*: The six panels show data for pressure, temperature, and relative humidity (columns from left to right). The top row displays GDAS profiles, while the bottom row shows percentual $\pm 1\sigma$ deviations from the mean profile. Dusk data are drawn in blue, the dawn profile in red.

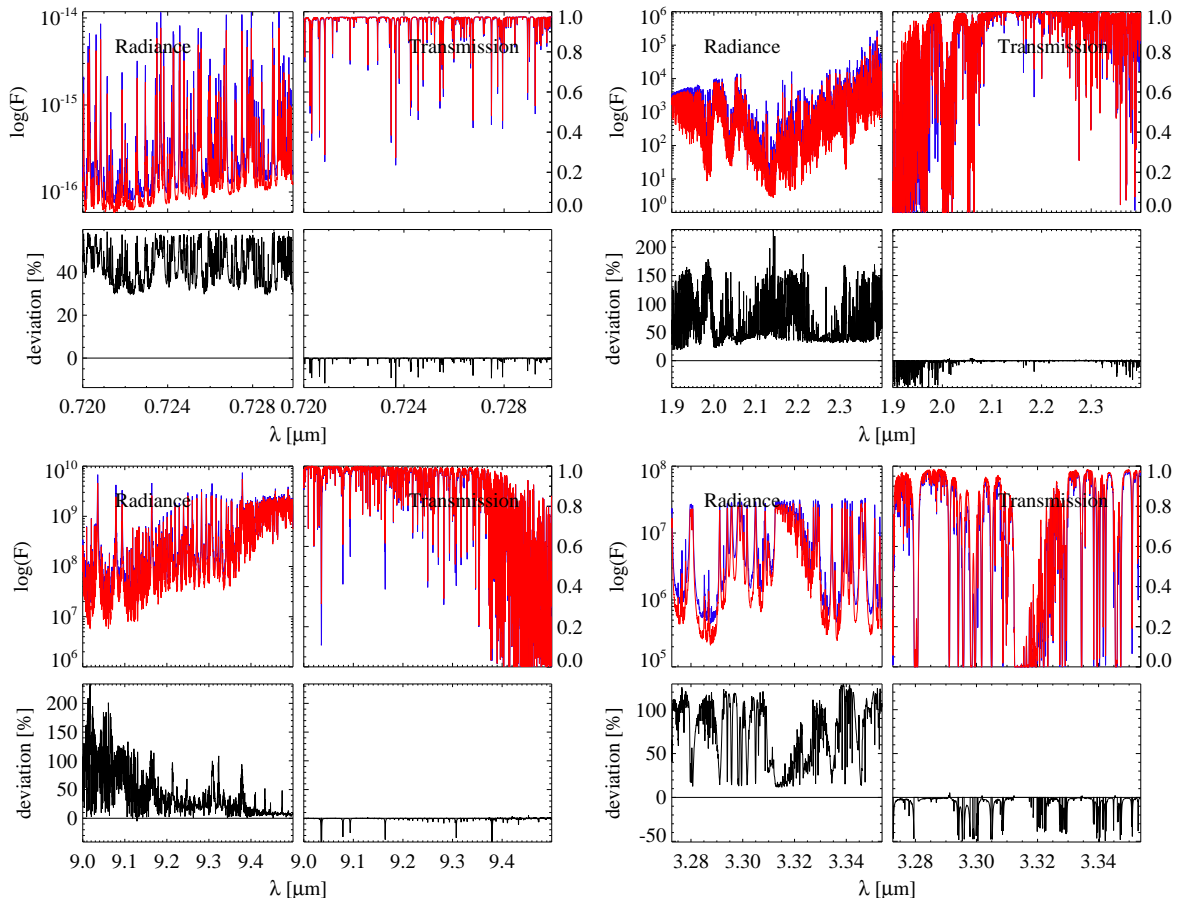


Figure 11: *Spectra comparing December/January and June/July for a whole night:* Spectra represent the difference between the values of the spectra for the two seasons each around midnight. Each of the four panels shows a different spectral window ($\sim 0.7 \mu\text{m}$, K -band, $\sim 9 \mu\text{m}$, $\sim 3.3 \mu\text{m}$; from top left, clockwise). The panels display radiance (left half) and transmission spectra (right half). The top rows show the emission (in flux units) and transmission spectra, while the bottom rows indicate the relative deviation of the plus/minus spectra from the mean. Blue, red, and black curves show the summer and winter spectra and the deviation, respectively.

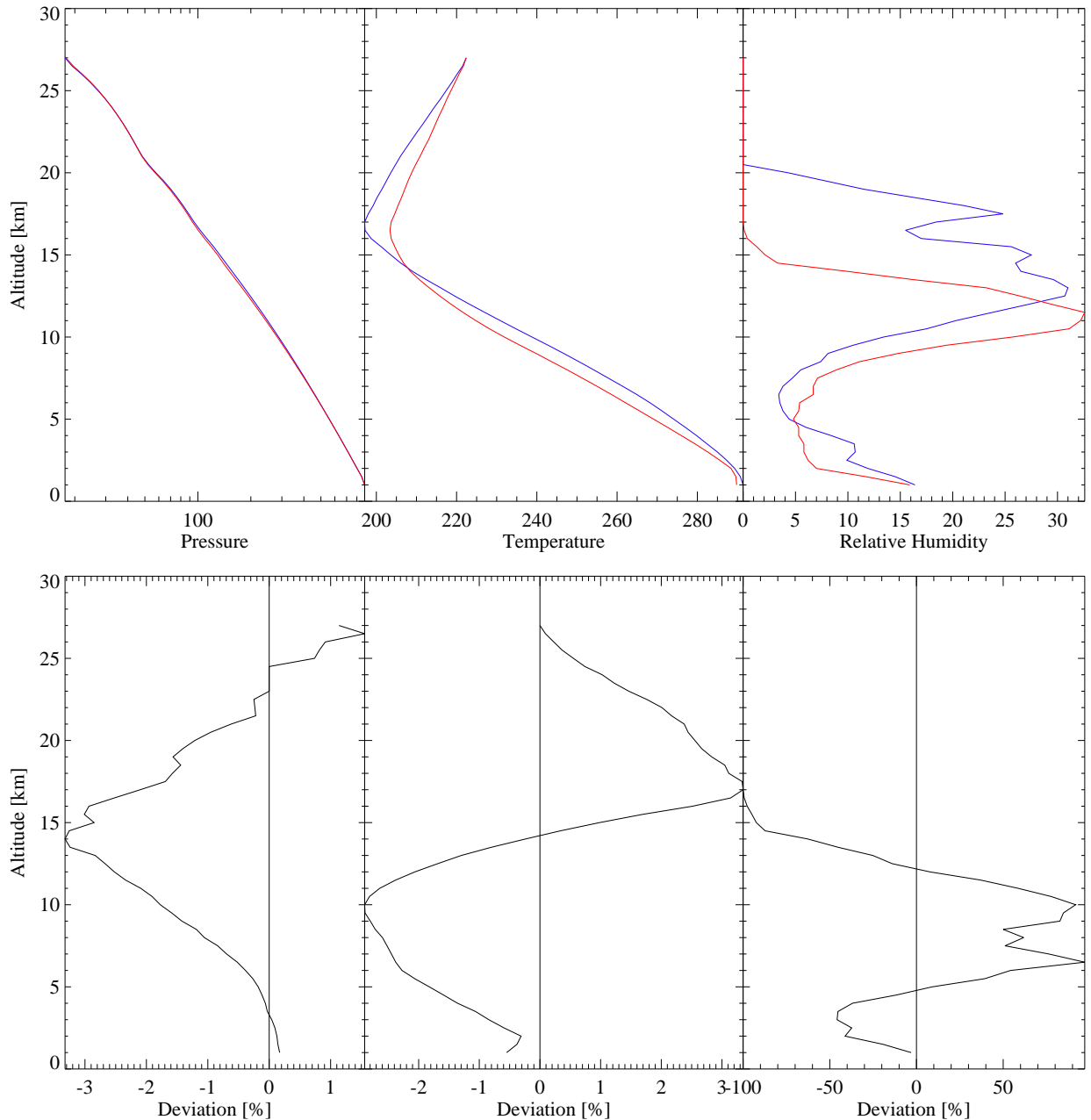


Figure 12: *GDAS profiles comparing December/January and June/July for a whole night:* The six panels show data for pressure, temperature, and relative humidity (columns from left to right). The top row displays GDAS profiles, while the bottom row shows percentual $\pm 1\sigma$ deviations from the mean profile. The December/January profile is shown in blue, the June/July profile in red.

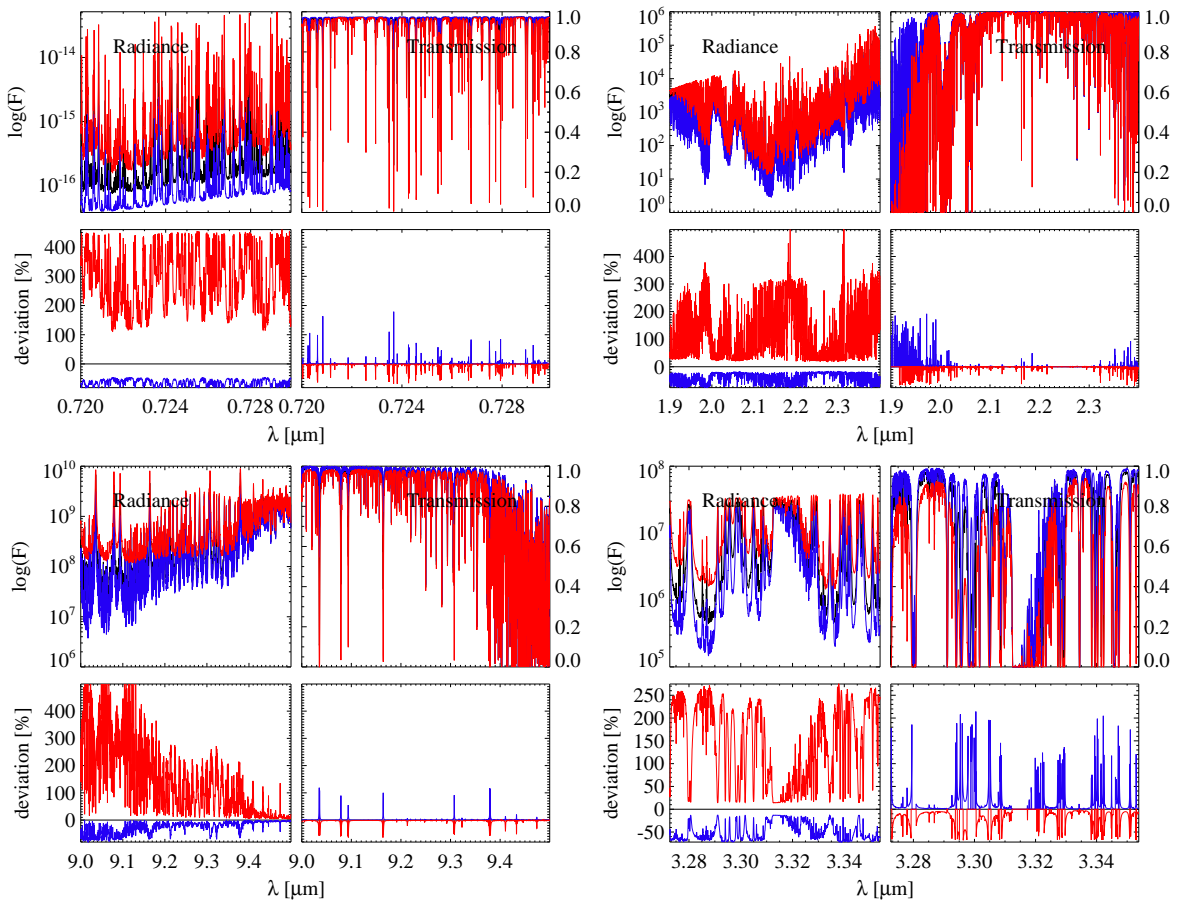


Figure 13: *Spectra for December/January, whole night:* Each of the four panels shows a different spectral window ($\sim 0.7 \mu\text{m}$, K -band, $\sim 9 \mu\text{m}$, $\sim 3.3 \mu\text{m}$; from top left, clockwise). The panels display radiance (left half) and transmission spectra (right half). The top rows show the emission (in flux units) and transmission spectra, while the bottom rows indicate the relative deviation of the plus/minus spectra from the mean. Blue, red, and black curves show the negative and positive error spectra and the mean spectrum, respectively.

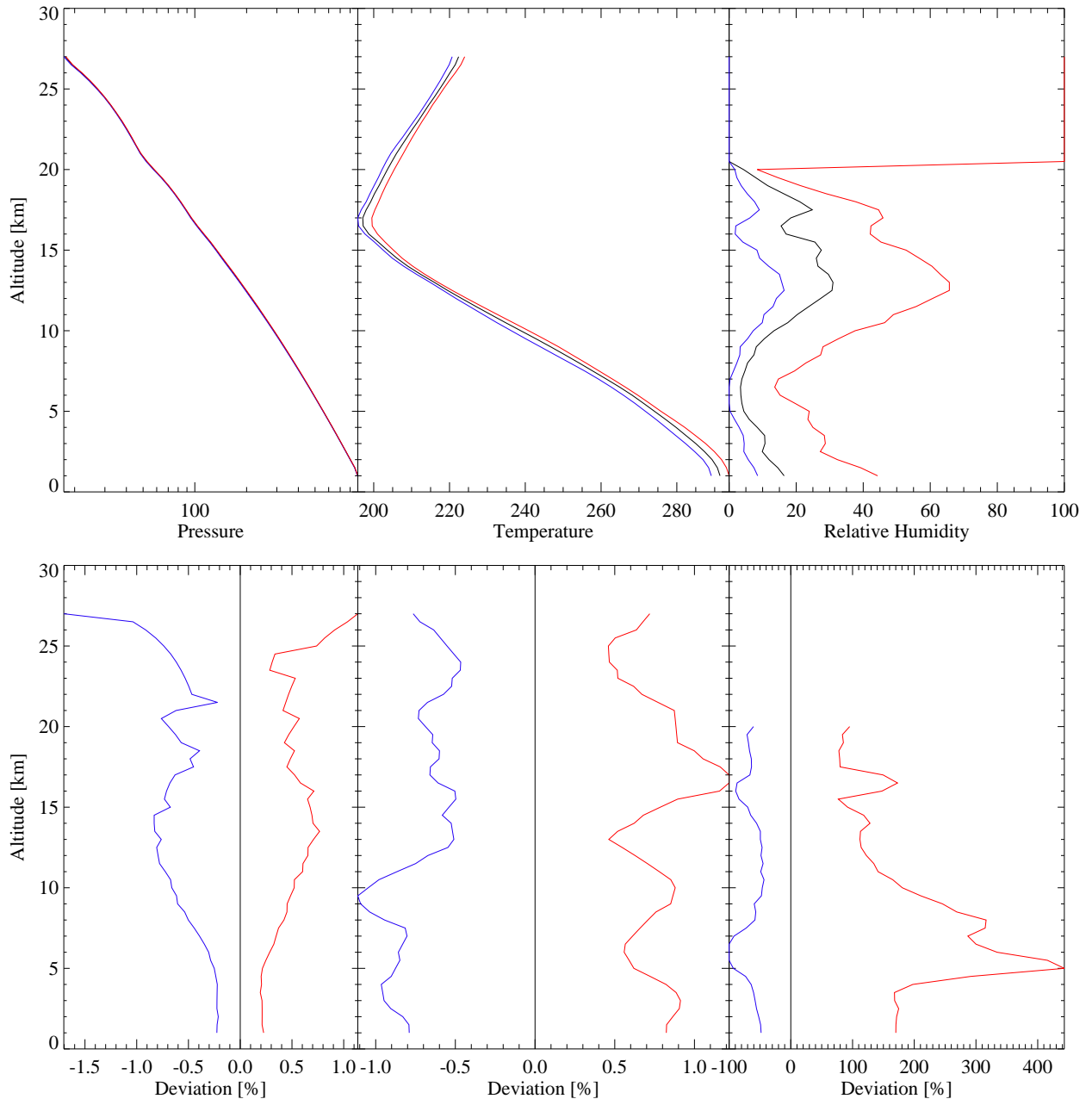


Figure 14: *GDAS profile for December/January, whole night:* The six panels show data for pressure, temperature, and relative humidity (columns from left to right). The top row displays GDAS profiles, while the bottom row shows percentual $\pm 1\sigma$ deviations from the mean profile. Red, black, and blue lines symbolise the -1σ , average and $+1\sigma$ values, respectively.

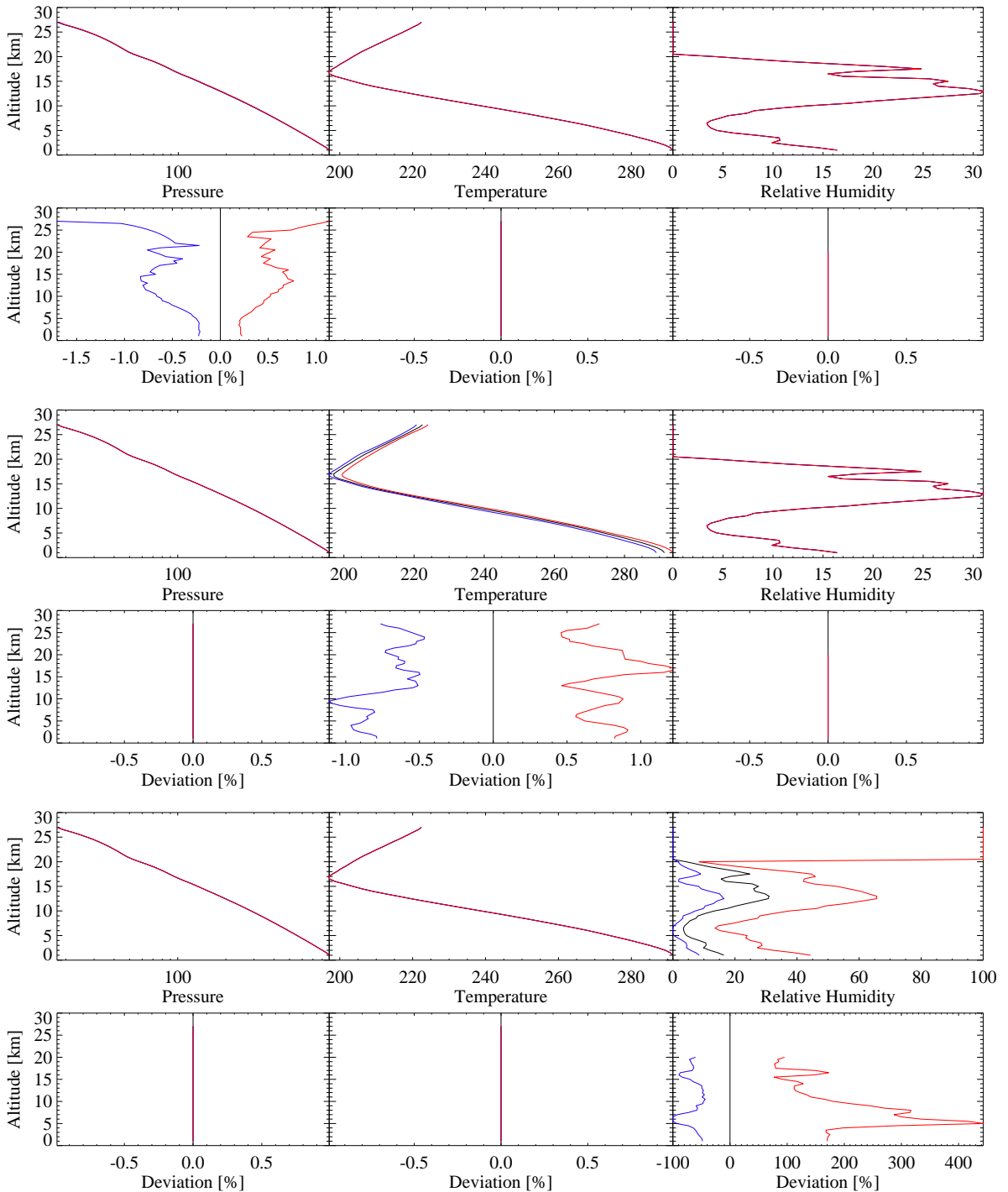


Figure 15: *Variation of pressure, temperature and humidity:* Average profiles (black) and their variation (red and blue) are shown (rows 1,3,5) together with the relative change compared to the average (rows 2,4,6). From left to right the graphs depict pressure, temperature, and relative humidity. Red, black, and blue lines symbolise the -1σ , average and $+1\sigma$ values, respectively.

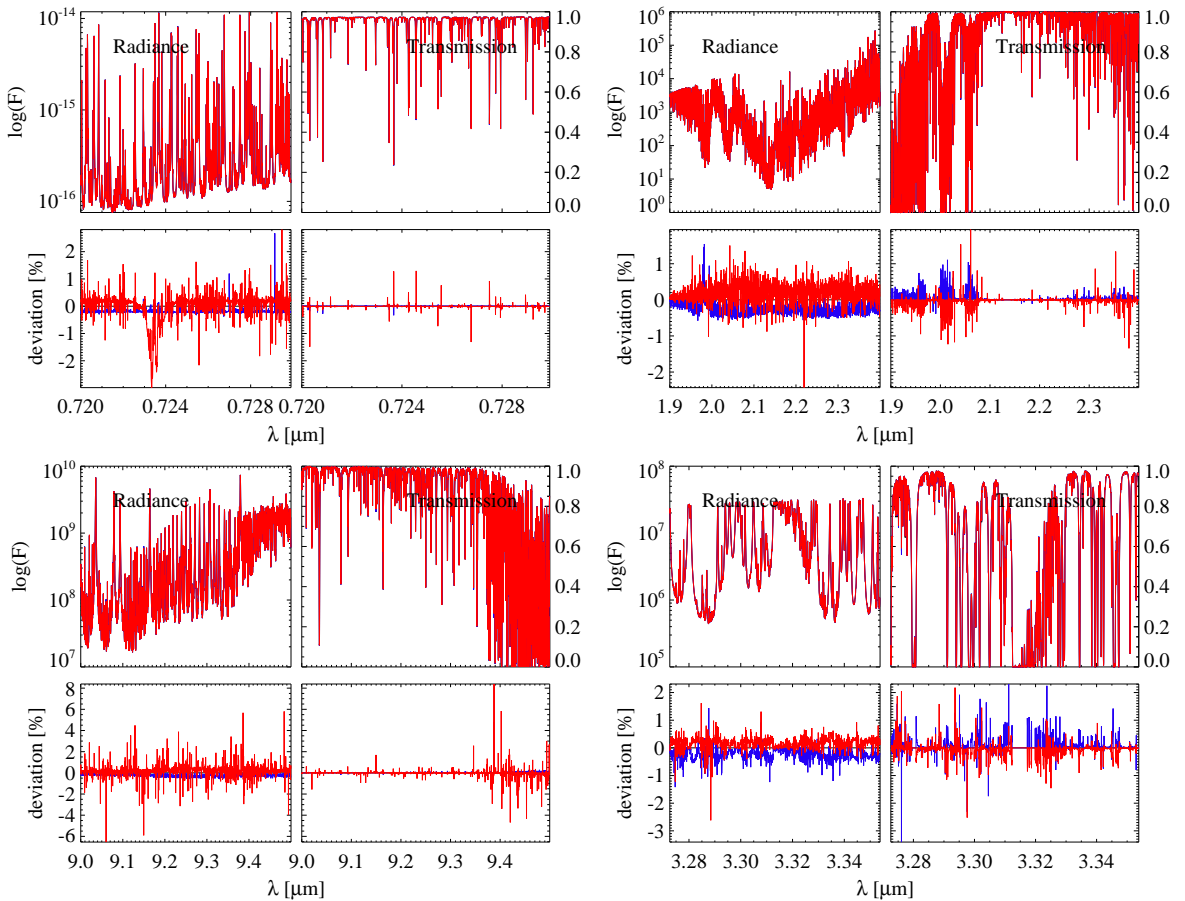


Figure 16: *Spectra resulting from varied pressure:* Each of the four panels shows a different spectral window ($\sim 0.7 \mu\text{m}$, K -band, $\sim 9 \mu\text{m}$, $\sim 3.3 \mu\text{m}$; from top left, clockwise). The panels display radiance (left half) and transmission spectra (right half). The top rows show the emission (in flux units) and transmission spectra, while the bottom rows indicate the relative deviation of the plus/minus spectra from the mean. Red, black, and blue lines symbolise the -1σ , average and $+1\sigma$ values, respectively.

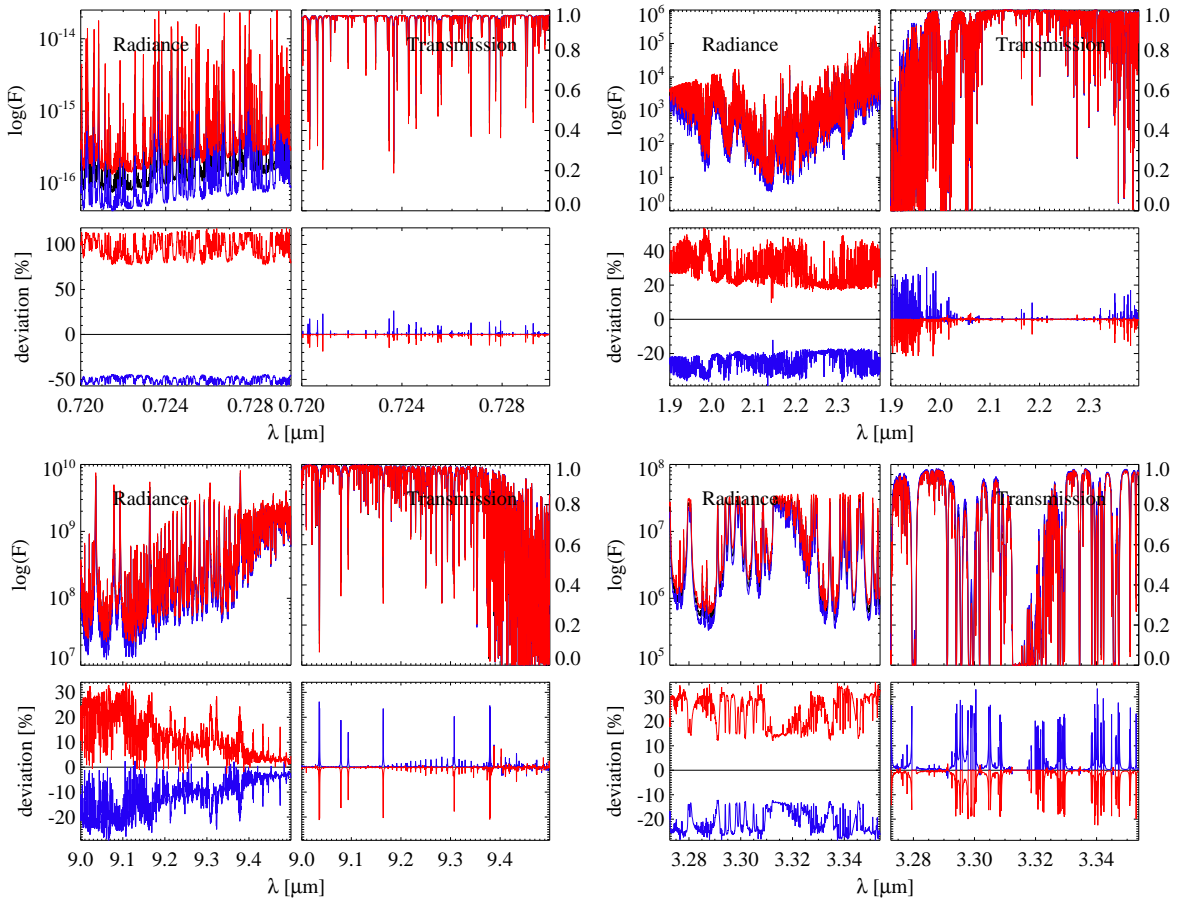


Figure 17: Same as Figure 16 for temperature.

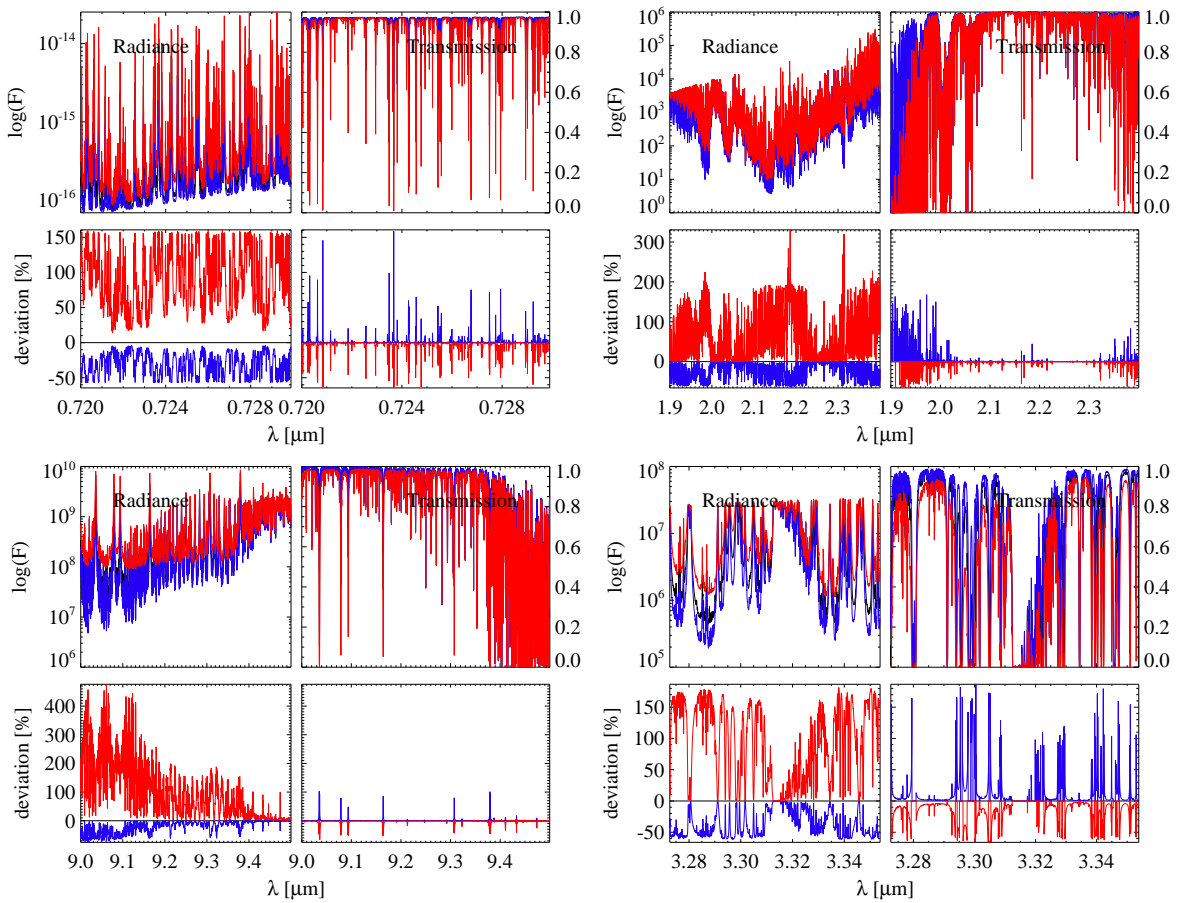


Figure 18: Same as Figure 16 for relative humidity.

ESO	The Cerro Paranal Advanced Sky Model	Doc:	VLT-MAN-ESO-19550-5339
		Issue:	Issue 1.1.1
		Date:	Date 2013-09-18
		Page:	40 of 80

5.5 Processing of the GDAS profiles and the EMM data

The main disadvantage of the GDAS profiles is that they do not represent the local atmospheric conditions of the geographical position and height of the observing site as accurately as provided by the EMM. Therefore, one has to investigate how the two sources of information can be merged into a single profile.

However, before applying such a merging process, the GDAS data themselves must be treated for use in the sky spectra library. First, they are regredded to a regular height grid with data points every 500 m in the interval from 1 km to 27 km. Interpolation uses a least squares algorithm at heights of up to and including 2.5 km and linear interpolation above. In addition, values are linearly interpolated at a height of 2.64 km to represent the level of Paranal Observatory. This value is used for calibration purposes only and does not enter the final output table. Values for relative humidity are constrained to the interval 0% to 100%.

For every requested time interval (in the ETC application) all included GDAS and EMM data points are collected and averaged. The two resulting distributions of selected data points at fixed height provide a mean as well as a scatter. The latter will serve as a 1σ error bar.

These distributions are fitted with a probability distribution function (PDF). The analytical version of the PDF takes the form of a skewed Gaussian as defined below:

$$p = \frac{\phi(y)}{\alpha - \kappa(x - \xi)}, \text{ where}$$

$$y = \begin{cases} -\frac{1}{\kappa} \ln \left[1 - \frac{\kappa(x - \xi)}{\alpha} \right], & \kappa \neq 0 \\ \frac{x - \xi}{\alpha}, & \kappa = 0 \end{cases}$$

$$\phi(x) = a \exp \left(-\frac{1}{2} x^2 \right),$$

with the mean value ξ , the width of the Gaussian α , and a measure for the skewedness κ as a function of the position x .

The form of the GDAS data point distributions varies significantly, though. As a result, this analytic form does not always produce a good fit for the mean and width. In cases where no good fit could be obtained, a second attempt is made to obtain at least an acceptable result for the mean by restricting the distribution to data points around the most probable point (all points with probabilities higher than 50% of that of the most probable data point). If that also fails, the mean of the distribution is obtained by a Gaussian fit or a resistant mean if more or less than four data points are available, respectively. In the cases when the analytic fit failed, the scatter is obtained from integrating outwards from the mean to the point until 1σ of the integrated total of the distribution on that side is reached. Only when the fitting succeeded, the value for the scatter is taken from the analytical function. An example of various fits is shown in Figure 19.

Finally, the fits for the individual heights are compiled in profiles for the mean and scatter. As the abrupt change from a successful analytical fit and an iterative estimate for the scatter results in artificial noise in the profiles, both the mean and scatter profiles are boxcar averaged with a 3-point smoothing window.

In comparison to the GDAS profiles, the EMM values are treated slightly differently before being used to correct the GDAS data. The EMM provides a distribution of measurements for a single height level only. Here, the data are more well behaved and the analytical function shown above provides decent fits resulting in acceptable mean values without further special treatment. However, the scatter is obtained again from an iterative integration around the mean value as detailed above.

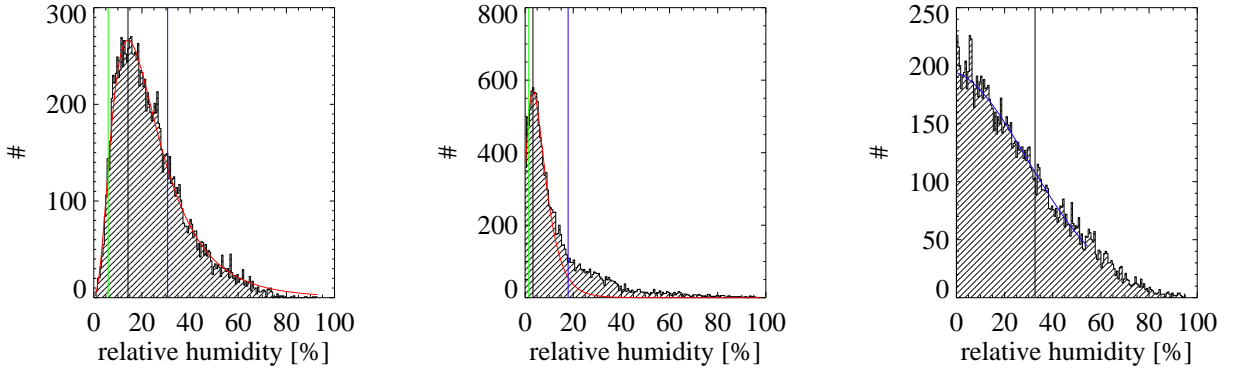


Figure 19: *PDF for a set of relative humidity values:* Successful fit with the analytical function (*left*): mean and scatter taken from analytical profile; successful fit with the analytical function only after restricting the fit range to values around the highest peak (*middle*): only mean taken from analytical fit, scatter results from iterative integration; fit with a Gaussian function (here with negative centre; *right*): mean from Gaussian (here forced to 0), scatter from iterative integration. See text for more detail.

What remains is to combine the two data sources into one single profile. As development of a sophisticated atmospheric model for this purpose is far beyond the scope of this application (and might not have a significant advantage over the solution presented here), it was opted to use a linear interpolation scheme to adjust the relative “importance” of the EMM data, *i.e.* the scaling factor by which the GDAS data have to be multiplied to incorporate the EMM data, from 100% at the height of the EMM measurement (and below) to 0% at a specific critical height h_{crit} (and above). Thus, the corrected value of a GDAS measurement $v_{\text{corr},\text{GDAS}}$ as a function of geoelevation h amounts to

$$v_{\text{corr},\text{GDAS}}(h) = c(h) \times v_{\text{GDAS}}(h)$$

with the correction factor

$$c(h) = \begin{cases} c(h_{\text{EMM}}), & h < h_{\text{EMM}} \\ (1 - b) \frac{h}{h_{\text{crit}}} + b, & h_{\text{EMM}} < h < h_{\text{crit}} \\ 1, & h > h_{\text{crit}} \end{cases}$$

and with

$$b = \frac{c(h_{\text{EMM}}) h_{\text{crit}} - h_{\text{EMM}}}{h_{\text{crit}} - h_{\text{EMM}}} \text{ and } c(h_{\text{EMM}}) = \frac{v_{\text{EMM}}}{v_{\text{GDAS}}(h_{\text{EMM}})}.$$

Here, h_{EMM} is the geoelevation of the EMM measurement v_{EMM} , h_{crit} is the critical altitude, and $v_{\text{GDAS}}(h)$ is the GDAS measurement at the geoelevation h .

A standard error propagation approach is used to implement a combined error $\sigma_{\text{corr},\text{GDAS}}(h)$ as function of geoelevation h from GDAS and EMM data. The correction function $c(h)$ as defined above is used again:

$$\sigma_{\text{corr},\text{GDAS}}(h) = v_{\text{corr},\text{GDAS}}(h) \left(1 \pm \sqrt{\left(\frac{\sigma_{\text{EMM}}}{v_{\text{EMM}}} \right)^2 c(h) + \left(\frac{\sigma_{\text{GDAS}}}{v_{\text{GDAS}}} \right)^2} \right),$$

with the EMM and GDAS measurements v_{EMM} and v_{GDAS} and their corresponding errors σ_{EMM} and σ_{GDAS} .

ESO	The Cerro Paranal Advanced Sky Model	Doc:	VLT-MAN-ESO-19550-5339
		Issue:	Issue 1.1.1
		Date:	Date 2013-09-18
		Page:	42 of 80

A close inspection of the predominant wind direction from the GDAS profiles as function of height (see Figure 20) reveals a gradual reversal (rotation of 180°) from sea level to a specific altitude layer (at around 5 km) beyond which it remains constant. Thus, it is safe to assume that by reaching this altitude, the air properties are no more significantly correlated with the local on-site measurements from EMM and have to be described by the GDAS data only. This defines the critical altitude $h_{\text{crit}} = 5 \text{ km}$ by which the impact of the EMM data must be reduced to zero, *i.e.* $c(h_{\text{crit}}) = 1$. The lower geoelevation limit of the altitude range of constant wind direction does not depend significantly on the season (*i.e.* time).

An example for a completely reduced GDAS profile including the aforementioned 3-point smoothing and the linearly interpolated local EMM data is shown in Figure 21.

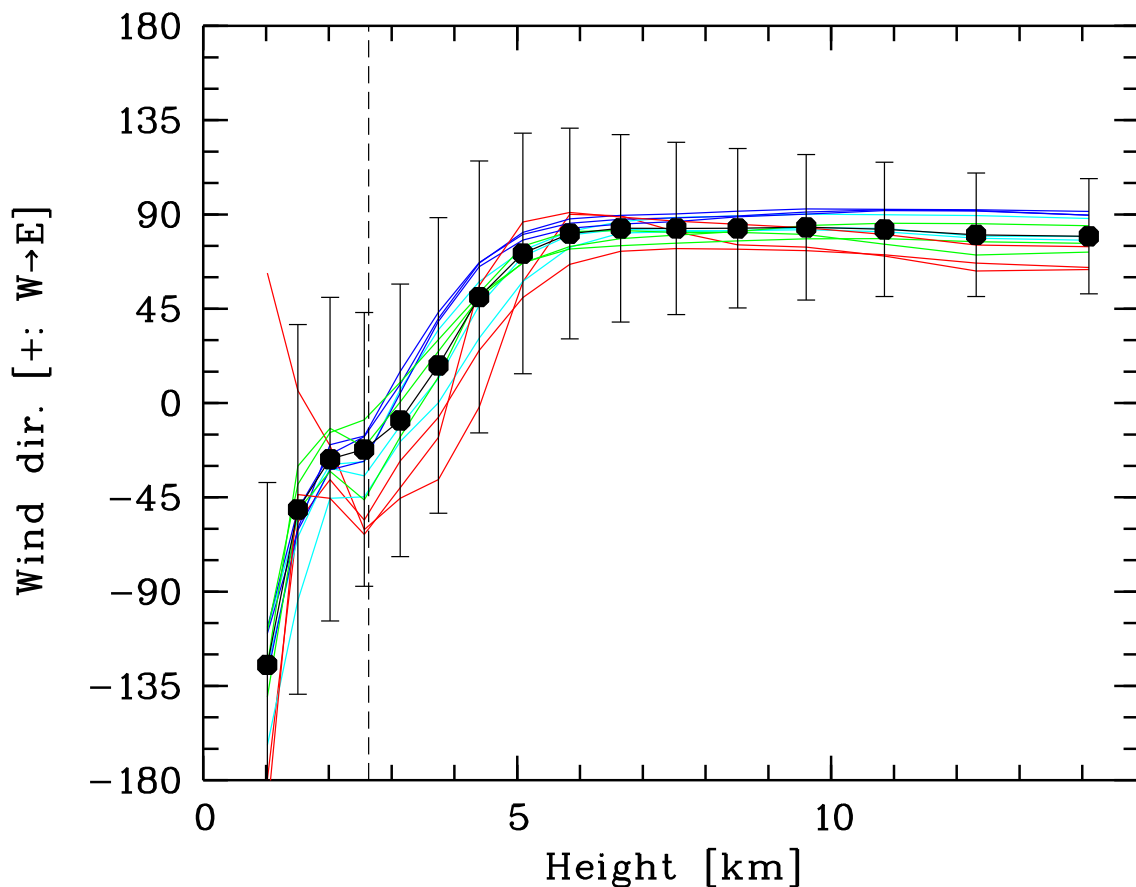


Figure 20: *GDAS wind direction as function of geoelevation:* red, cyan, blue, and green curves represent summer, autumn, winter, and spring, respectively. The black symbols show the all year average with the corresponding scatter. The vertical dashed line marks the geoelevation of Cerro Paranal. At $\sim 5 \text{ km}$ height, a constant plateau is reached.

ESO	The Cerro Paranal Advanced Sky Model	Doc: VLT-MAN-ESO-19550-5339
		Issue: Issue 1.1.1
		Date: Date 2013-09-18
		Page: 43 of 80

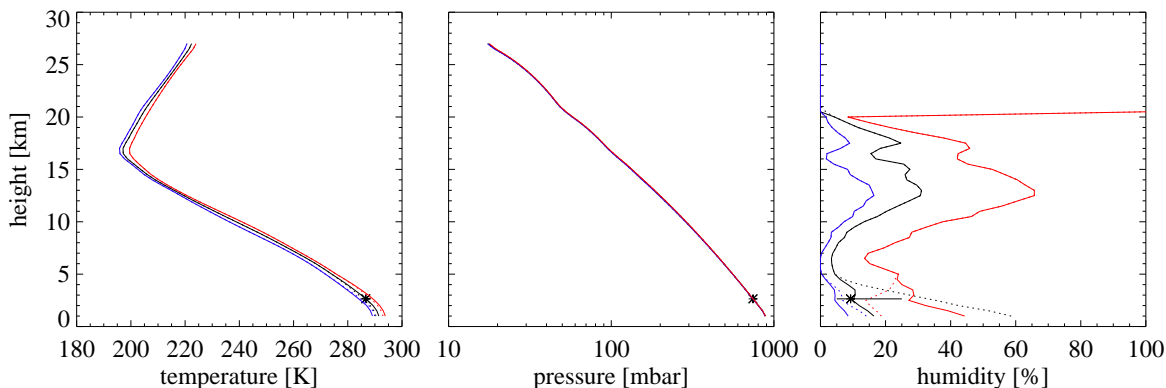


Figure 21: *Fully reduced GDAS profile including EMM data:* The panels show temperature, pressure, and humidity (from left to right). Black, red, and blue curves illustrate the average, plus, and minus 1σ profiles. The EMM value and its $\pm 1\sigma$ scatter are indicated by the cross with the horizontal bar (largest impact in humidity). The dotted lines show the GDAS profiles without incorporating the EMM data.

5.6 Merging standard and GDAS profiles

The main input to Module 1 are the pre-processed atmospheric standard and GDAS profiles (see Section 5.5). The LBLRTM code requires a single atmospheric profile to work with, though. Therefore, a common step in Module 1 before starting either of the two codes is to merge the GDAS and the standard profile.

In the merging procedure, the information contained in the GDAS profiles is incorporated into the standard atmospheric profile. The resulting merged profile comprises all columns from the standard profile and has pressure, temperature, and H₂O columns replaced with the GDAS values. The merged profile is interpolated to a new irregular altitude grid over the range from 1 km to 120 km with 50 levels, the first 25 of which originate from GDAS. The four altitude levels from 20 km to 26 km are a weighted mix of GDAS and standard profile. The influence of the GDAS profile decreases with increasing geoelevation: 80%, 60%, 40%, and 20% at 20 km, 22 km, 24 km, and 26 km, respectively. Beyond 26 km, no GDAS information is available. Note that GDAS does not contain values for molecules other than H₂O (in the form of relative humidity). At altitudes $h < 26$ km, only standard profile information is available for all other molecules.

5.7 Profiles for given PWV values

The sky model offers the computation of radiance and transmission spectra for fixed PWV values (see Section 3). The required input atmospheric profiles for the radiative transfer code are produced by a simple scaling of the merged profiles discussed in Section 5.6. For the selected season, the water vapour profile is integrated to obtain the corresponding PWV value. The ratio of the requested value and the profile-related one then results in a correction factor that is applied to the water vapour concentrations of all pressure levels in the same way. Since the amount of water vapour in the profiles is given in ppmv, the possible occurrence of relative humidities larger than 100% is not an issue. After the scaling, the original profile uncertainties are no more valid. Since the true scatter for a fixed PWV value cannot be retrieved from the existing profiles, spectra are computed without errors.

ESO	The Cerro Paranal Advanced Sky Model	Doc:	VLT-MAN-ESO-19550-5339
		Issue:	Issue 1.1.1
		Date:	Date 2013-09-18
		Page:	44 of 80

The standard library for Module 2 contains molecular spectra for the PWV values 0.5, 1.0., 1.5, 2.5, 3.5, 5.0, 7.5, 10.0, and 20.0 mm. All spectra are based on the annual mean profile, *i.e.* the spectra do not depend on the selected bimonthly period. For each PWV value, the same set of airmasses is available as for the time-dependent library (see Section 5.4).

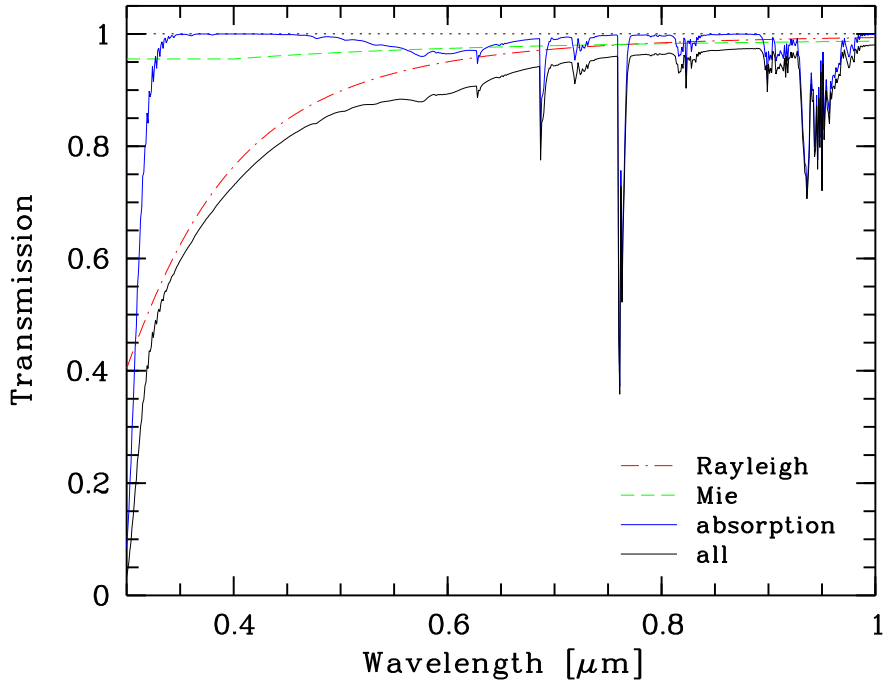


Figure 22: Annual mean zenith transmission curve for Cerro Paranal in the optical (black solid line). The Earth's atmosphere extinguishes the flux from point sources by Rayleigh scattering by air molecules (red dash-dotted line), Mie scattering/absorption by aerosols (green dashed line), and molecular absorption (blue solid line). For the plotted wavelength range, the latter is caused by molecular oxygen (A band at $0.762\text{ }\mu\text{m}$, B band at $0.688\text{ }\mu\text{m}$, and γ band at $0.628\text{ }\mu\text{m}$), water vapour (prominent bands at 0.72 , 0.82 , and $0.94\text{ }\mu\text{m}$), and ozone (Huggins bands in the near-UV and broad Chappuis bands at about $0.6\text{ }\mu\text{m}$).

6 Sky model components

The sky model provides transmission curves (values between 0 and 1; Section 6.1) as well as night-sky radiance spectra in $\text{phot s}^{-1}\text{ m}^{-2}\text{ }\mu\text{m}^{-1}\text{ arcsec}^{-2}$ (Section 6.2) depending on the selected input parameters. In both cases, the wavelength units are μm . In the following, a brief overview of the sky model given. For more details, see Noll et al. [2012].

6.1 Transmission

Atmospheric extinction includes Rayleigh scattering by air molecules, Mie scattering by aerosols, and molecular/aerosol absorption (see Figure 22). The strongly wavelength-dependent Rayleigh scattering is approximated using a well-established formula provided by Liou [2002]. For aerosol extinction, the approximation of Patat et al. [2011] for Cerro Paranal is taken. For wavelengths longer than $0.4\text{ }\mu\text{m}$, the extinction coefficient is then

$$k_{\text{aer}}(\lambda) \approx k_0 \lambda^\alpha, \quad (1)$$

where $k_0 = 0.013 \pm 0.002 \text{ mag airmass}^{-1}$ and $\alpha = -1.38 \pm 0.06$, with the wavelength λ in μm . For shorter wavelengths, the constant $k_{\text{aer}} = 0.050 \text{ mag airmass}^{-1}$ is used, which shows a better agreement with the data

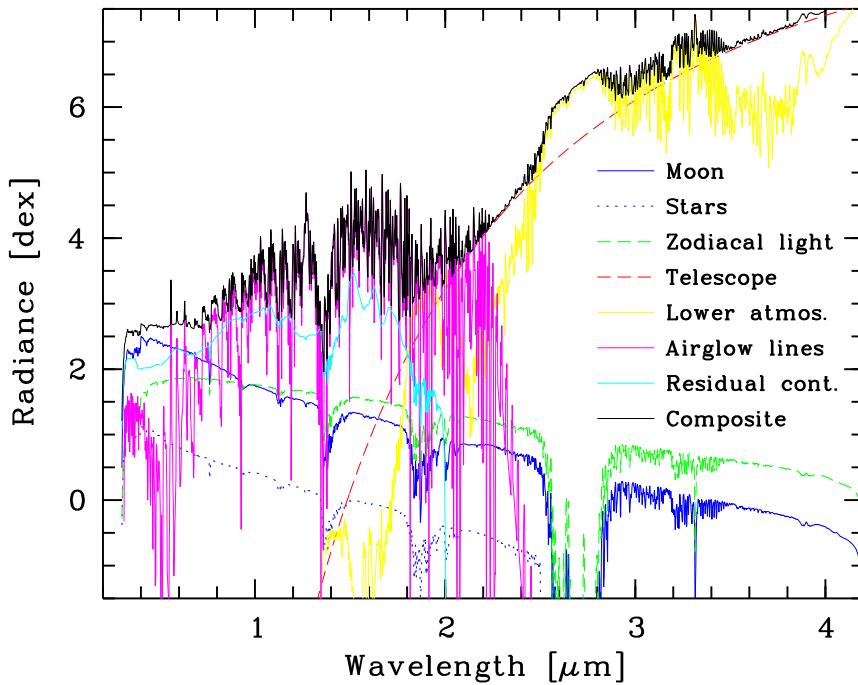


Figure 23: Components of the sky model in logarithmic radiance units for wavelengths between 0.3 and 4.2 μm . This example, with the Moon above the horizon, shows scattered moonlight, scattered starlight, zodiacal light, thermal emission by the telescope and instrument, molecular emission of the lower atmosphere, airglow emission lines of the upper atmosphere, and airglow/residual continuum.

than the fit. The molecular absorption can be computed by a radiative transfer code (see Section 4). Module 1 (see Section 2.1) provides a suitable library of LBLRTM [1] absorption spectra (see Section 5.4), which especially depend on the amount of water vapour in the atmosphere. The library contains mean spectra and 1σ scatter for six bimonthly periods (starting with December/January) and the entire year (cf. Section 5.4, 6.2.5, 6.2.6, and 6.2.7). Instead of a selection by period, the user can also choose a certain amount of PWV (see Section 3). Spectra for nine different PWV values from 0.5 to 20 mm are available in the default Module 1 library. Molecular spectra are available for five different airmasses from 1 to 3. An interpolation/extrapolation procedure is performed by the ASM to derive realistic transmission curves for arbitrary object altitude angles. For the conversion from zenith distance z to airmass X , the formula

$$X = \left(\cos(z) + 0.025 e^{-11 \cos(z)} \right)^{-1}, \quad (2)$$

of Rozenberg [1966] is taken.

6.2 Radiances

The sky emission model consists of seven additive components (see Figure 23). These are scattered moonlight, scattered starlight, zodiacal light, thermal emission by telescope and instrument, molecular emission in the lower atmosphere, airglow emission lines of the upper atmosphere, and the residual airglow continuum.

ESO	The Cerro Paranal Advanced Sky Model	Doc:	VLT-MAN-ESO-19550-5339
		Issue:	Issue 1.1.1
		Date:	Date 2013-09-18
		Page:	47 of 80

6.2.1 Scattered moonlight

Moonlight scattered in the Earth's atmosphere is an important sky emission component. In particular, optical wavelengths are affected, since the Moon spectrum can be approximated by a reddened solar spectrum and the intensity of scattering increases with decreasing wavelength (see Figure 24).

The top-of-atmosphere Moon irradiance is modelled using the solar spectrum of Colina et al. [1996] and the phase- and wavelength-dependent disc-equivalent Moon albedo of Kieffer & Stone [2005] based on data from the RObotic Lunar Observatory (ROLO). Considering the results of Velikodsky et al. [2011], the ROLO-based albedo is increased by 15%. Since Kieffer & Stone did not study the distribution of highlands and maria for crescent Moon phases, a simple constant extrapolation of the relative irradiance change by this effect is assumed for such conditions. The model parameters related to the Moon irradiance are the lunar phase angle α , *i.e.* the separation angle of Moon and Sun as seen from Earth, and the Moon distance, which can deviate up to 9% from the mean radius of the Moon's orbit around the Earth (384,400 km). The parameter α can be estimated from the fractional lunar illumination (FLI) by

$$\alpha \approx \arccos(1 - 2 \text{FLI}), \quad (3)$$

since the influence of the lunar ecliptic latitude on α is negligible. In order to distinguish between waxing and waning Moon, α values between 0° and 360° are allowed. For $\alpha > 180^\circ$, a waning Moon is assumed. An example Moon irradiance spectrum is shown in Figure 24. It is redder than the solar spectrum. The continuum slope depends on α .

The ASM calculates the Moon-related sky surface brightness by means of a three-dimensional (3D) radiative transfer model for Rayleigh scattering, aerosol extinction, and molecular absorption. The single scattering calculations are performed in a similar way as described in Noll et al. [2012] for extended radiation sources (see also Woltencroft & van Breda [1967]; Staude [1975]), although the Moon is approximated by a point source and Rayleigh and aerosol scattering are calculated simultaneously, assuming the optical depths related to the Patat et al. [2011] extinction curve for Cerro Paranal (see Figure 22). Moreover, using the Bohren & Huffman [1983] Mie scattering algorithm, the aerosol scattering phase functions were derived from log-normal aerosol distributions (Warneck & Williams [2012]) optimised for the Patat et al. [2011] extinction curve. The required input parameters for the scattering calculations are the altitudes of the target and the Moon above the horizon, and the angular separation of target and Moon ρ . The resulting wavelength-dependent single scattering intensities are corrected for multiple scattering by factors which were pre-calculated by an external, extended 3D radiative transfer code for double scattering. This code considers all relevant combinations of scattering processes by molecules, aerosols, and the ground. The required wavelength-dependent ground reflectance function was taken from reflectance measurements of soil from the Atacama desert by Sutter et al. [2007] and slightly adapted to values from data of the Ozone Measuring Instrument (OMI) of the Aura satellite [12] for the Cerro Paranal region.

Absorption by aerosols is considered by assuming a single scattering albedo of 0.97, as also estimated from OMI data. For absorption by molecules, the same density profile as for Rayleigh scattering is used. The reduction of scattered moonlight by molecular absorption is approximated via the input transmission spectrum (see Section 6.1) and an effective airmass, which is derived from single scattering calculations of fixed scattering optical depth and variable absorption optical depth. No radiative transfer calculations are performed for ozone. Instead, a layer at an altitude of 25 km is assumed, which absorbs but does not scatter.

The described model deviates from an older approach based on the model of Krisciunas & Schaefer [1991], which is discussed in Noll et al. [2012]. The new model is more accurate, especially at short wavelengths (see

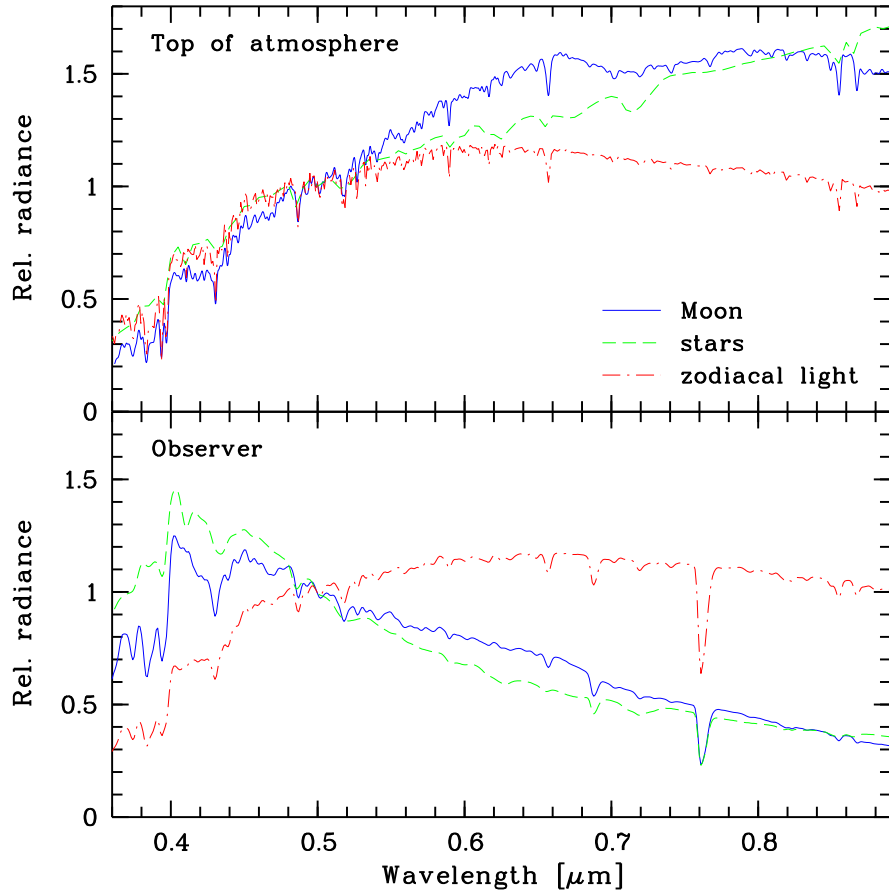


Figure 24: Effects of atmospheric scattering on radiation originating outside of the atmosphere. The displayed radiation sources are Moon (blue solid lines), stars (green dashed lines), and interplanetary dust (red dash-dotted lines). All spectra are normalised to unity at $0.5\text{ }\mu\text{m}$. In the *upper panel*, a top-of-atmosphere moonlight spectrum is shown. It is significantly reddened compared to a solar spectrum due to the wavelength-dependent surface reflectance of the Moon. A slightly reddened solar spectrum is taken for solar radiation scattered at interplanetary dust grains. Integrated starlight tends to be redder than sunlight at long wavelengths. The *lower panel* shows the resulting, low-resolution example spectra, after light has been scattered in the Earth's atmosphere. While the lunar and stellar contributions represent scattered radiation only, the dust-related zodiacal light consists of scattered and direct light.

ESO	The Cerro Paranal Advanced Sky Model	Doc:	VLT-MAN-ESO-19550-5339
		Issue:	Issue 1.1.1
		Date:	Date 2013-09-18
		Page:	49 of 80

Section 7).

Note [August 2018]: The original version of the sky model included a correction factor of 1.2 applied on the scattered moonlight. This is discussed in Jones et al. [2013], p.10. Subsequently, in August 2018 it was decided to remove the correction factor from the sky model and the code has been updated accordingly. Thus, the results in this document can only be reproduced taking the correction factor into account.

6.2.2 Scattered starlight

Like moonlight, starlight is also scattered in the Earth's atmosphere. However, stars are distributed over the entire sky with a distribution maximum towards the centre of the Milky Way. Since scattered starlight is only a minor component compared to scattered moonlight and zodiacal light (see Figure 23), it is sufficient for an ETC application to compute a mean spectrum.

For the integrated starlight (ISL), Pioneer 10 data at $0.44\text{ }\mu\text{m}$ are used (Toller [1981]; Toller et al. [1987]; Leinert et al. [1998]). These data are almost unaffected by zodiacal light. Since the Pioneer 10 maps do not include stars brighter than 6.5 mag in V , a global correction given by Melchior et al. [2007] is applied.

ISL is an extended radiation source. Hence, light is not only scattered out of the line of sight, it is also scattered into it. This effect causes an effective extinction curve to differ from that of a point source and depends on the spatial distribution of the extended emission. To quantify the change of the extinction curve, 3D scattering calculations were performed (see Wolstencroft & van Breda [1967]; Staude [1975]; Noll et al. [2012]). The scattering code was run for different combinations of zenithal optical depth, zenith distance, azimuth, and side-real time for Rayleigh and aerosol (Mie) scattering. Using the relation between optical depth and wavelength as provided by the Cerro Paranal extinction curve (see Section 6.1), the resulting mean scattering intensities were translated into a spectrum. This was then multiplied by the B -band normalised, mean ISL spectrum of Mattila [1980] (see Figure 24) to obtain the final scattered starlight spectrum. The molecular absorption remains the only variable and depends on the selected library spectrum (see Section 6.1). For the effective absorption airmass, the mean value of 1.25 is assumed.

6.2.3 Zodiacal light

Zodiacal light is caused by scattered sunlight from interplanetary dust grains in the plane of the ecliptic. A strong contribution is found for low absolute values of ecliptic latitude and heliocentric ecliptic longitude. The brightness distribution provided by Levasseur-Regourd & Dumont [1980] and Leinert et al. [1998] for $0.5\text{ }\mu\text{m}$ shows a relatively smooth decrease for increasing elongation, *i.e.* angular separation of object and Sun. A striking exception is the local maximum of the so-called gegenschein at the antisolar point in the ecliptic. The spectrum of the optical zodiacal light is similar to the solar spectrum (Colina et al. [1996]), but slightly reddened (see Figure 24). The relations given in Leinert et al. [1998] are applied to account for the reddening. The correction is larger for smaller elongations. Thermal emission of interplanetary dust grains in the IR is neglected in the sky model, since the airglow components of atmospheric origin (see Figure 23) completely outshine it. In the optical, zodiacal light is a significant component of the sky model. A contribution of about 50% is typical of the B and V bands when the Moon is down.

The model of the zodiacal light presented in Leinert et al. [1998] describes the characteristics of this emission component outside of the Earth's atmosphere. Ground-based observations of the zodiacal light also have to take

ESO	The Cerro Paranal Advanced Sky Model	Doc:	VLT-MAN-ESO-19550-5339
		Issue:	Issue 1.1.1
		Date:	Date 2013-09-18
		Page:	50 of 80

atmospheric extinction into account. Since zodiacal light is an extended radiation source, the observed intensity is a combination of the extinguished top-of-atmosphere emission in the viewing direction and the intensity of light scattered into the line of sight (see Figure 24). The latter can be treated by scattering calculations as discussed in Section 6.2.2. The radiative transfer code was run for different combinations of zenithal optical depth, zenith distance, azimuth, sidereal time, and solar ecliptic longitude for Rayleigh and aerosol (Mie) scattering. The results were used to derive approximations for the wavelength-dependent effective extinction of the zodiacal light, which require the Cerro Paranal extinction curve (Patat et al. [2011]) as input and only depend on the zenith distance of the object and the line-of-sight top-of-atmosphere zodiacal light intensity. In this way, additional sky model input parameters are not needed for the scattering model. At the most affected blue wavelengths, its uncertainties are expected to be in the order of a few per cent only. Finally, the molecular absorption of the zodiacal light is taken from the Module 1 library spectrum with the best-fitting observing conditions (see Section 6.1).

6.2.4 Thermal emission by telescope and instrument

The telescope structure and the observing instrument cause unavoidable thermal emission in the IR. Although the sky model aims at providing an instrument-independent sky background flux, this component cannot be neglected, since it is usually a remnant of flux-calibrated sky spectra. Astronomical data pipelines do not remove this contribution because it does not affect sky-subtracted spectra. For ETC applications, it is also an important component. Since the current ESO ETCs only handle the flux losses inside the telescope and instrument by means of an instrument response curve, the sky model provides a simple thermal emission model. It assumes that atmospheric and instrument-related emission is corrected by the same response curve. In principle, this is not correct, because radiation from optical components is less absorbed than the sky emission. Therefore, the calculated emission is an apparent one that overestimates the true emission. Nevertheless, this procedure returns the correct flux ratio of instrument and sky emission provided that a single response curve is applied to both emission sources.

The thermal emission of an optical component i can be estimated by so-called grey bodies which are calculated by a black body (BB) of temperature T_i times a wavelength-independent emissivity ϵ_i . The components $i + 1$ to n , which are behind the component i in the light path, absorb part of this emission. Each component reduces it by a factor of $1 - \epsilon$. In order to have the same flux level as the sky emission, which is absorbed by all n components, the telescope/instrument emission of i has to be divided by the product of the transmissions of the components 1 to i . Hence, the effective, apparent grey body emission (without applying the instrument response curve) can be calculated by

$$F_{\text{tel}} = \frac{\epsilon_1}{(1 - \epsilon_1)} \text{BB}(T_1) + \frac{\epsilon_2}{(1 - \epsilon_1)(1 - \epsilon_2)} \text{BB}(T_2) + \dots + \frac{\epsilon_n}{(1 - \epsilon_1)(1 - \epsilon_2)\dots(1 - \epsilon_n)} \text{BB}(T_n). \quad (4)$$

The first component corresponds to the main mirror, which usually dominates the emission. The equation above provides only a rough estimate, since emission and absorption in an instrument is not considered if it is not related to a listed optical component. Moreover, scattering is completely neglected.

Since at least the telescope is at the ambient temperature of about 280-290 K (Cerro Paranal), telescope/instrument emission is expected to be important at wavelengths longwards of the H -band.

ESO	The Cerro Paranal Advanced Sky Model	Doc:	VLT-MAN-ESO-19550-5339
		Issue:	Issue 1.1.1
		Date:	Date 2013-09-18
		Page:	51 of 80

6.2.5 Molecular emission of the lower atmosphere

Weather-dependent emission by molecules in the lower atmosphere, *i.e.* troposphere and stratosphere, is an important component of the sky model in the IR. As in the case of the telescope/instrument emission (see Section 6.2.4), wavelengths longwards of the H -band are significantly affected by molecular emission (see Figure 23). The rough agreement of telescope/instrument emission and molecular emission close to the ground level at their lower wavelength limit is caused by the similarity of their temperatures.

As the molecular absorption (see Section 6.1), the molecular emission and its uncertainties are taken from the library computed by Module 1 (see Section 2.1 and 5.4). The default library contains results from the radiative transfer code LBLRTM [1] and depends on season (six two-month periods) and target altitude (or airmass). This classification takes into account the differences in molecular radiance spectra resulting from the variation of typical weather conditions for different seasonal periods. Only nocturnal atmospheric profiles were considered for the computation of the seasonal averages. As already discussed in Section 6.1, the library of molecular spectra also includes spectra for a fixed PWV value, which can be selected by setting the corresponding ASM input parameter (see Section 3). For airmasses not provided by the library, an extrapolation is carried out which uses the transmission spectrum to estimate the optical depth dependent effect of the airmass on the flux. For the standard airmass set, the errors of this extrapolation are not larger than 5%. For wavelength regions of high transmission, the deviations are close to zero.

6.2.6 Emission lines of the upper atmosphere

The wavelength range from the near-UV to the near-IR is characterised by strong emission lines. Most of them constitute band structures. This airglow (see Khomich et al. [2008] for a comprehensive discussion) mostly originates in the mesopause region at about 90 km. In addition, some lines arise in the ionospheric F2-layer at about 270 km. In general, airglow is caused by chemiluminescence, *i.e.* chemical reactions that lead to light emission by the decay of excited electronic states of reaction products. Apart from atomic oxygen and sodium, the oxygen (O_2) and hydroxyl (OH) molecules are the most important reaction products in this context. In general, airglow lines show strong variability from time scales in the order of minutes to years. This behaviour can be explained by the solar activity cycle, seasonal changes in the temperature, pressure, and chemical composition of the emission layers, the day-night contrast, dynamical effects such as gravity waves, or geomagnetic disturbances.

A complex semi-empirical model has been developed to treat emission lines of the upper atmosphere in the context of the sky model (see Noll et al. [2012]). For the wavelength range from 0.3143 to 0.9228 μm line wavelengths, relative fluxes, and identifications are taken from Cosby et al. [2006], who considered the UVES-based sky emission line atlas of Hanuschik [2003]. A gap at about 0.86 μm is filled by unpublished UVES 800U data. For this wavelength range, lines were identified by means of the HITRAN database (see Rothman et al. [2009] and [4]). At wavelengths longer than 0.9228 μm , calculations of OH line intensities of Rousselot et al. [2000] are used. In contrast to the outdated Einstein coefficients of Mies [1974] employed by Rousselot et al., the sky model line list contains corrected intensities based on Einstein coefficients published by Goldman et al. [1998]. The band-averaged correction factors range from 0.38 to 2.06. The most extreme corrections are related to the bands with the largest transition in the vibrational level Δv (see Khomich et al. [2008] for a comparison). Changes in the ratio of OH lines within a band were neglected, since these corrections are only in the order of a few per cent for most relevant lines (see Goldman et al. [1998]). The flux of the calculated OH lines is scaled to the Cosby et al. [2006] line intensities between 0.642 and 0.858 μm . In addition, the $O_2(a-$

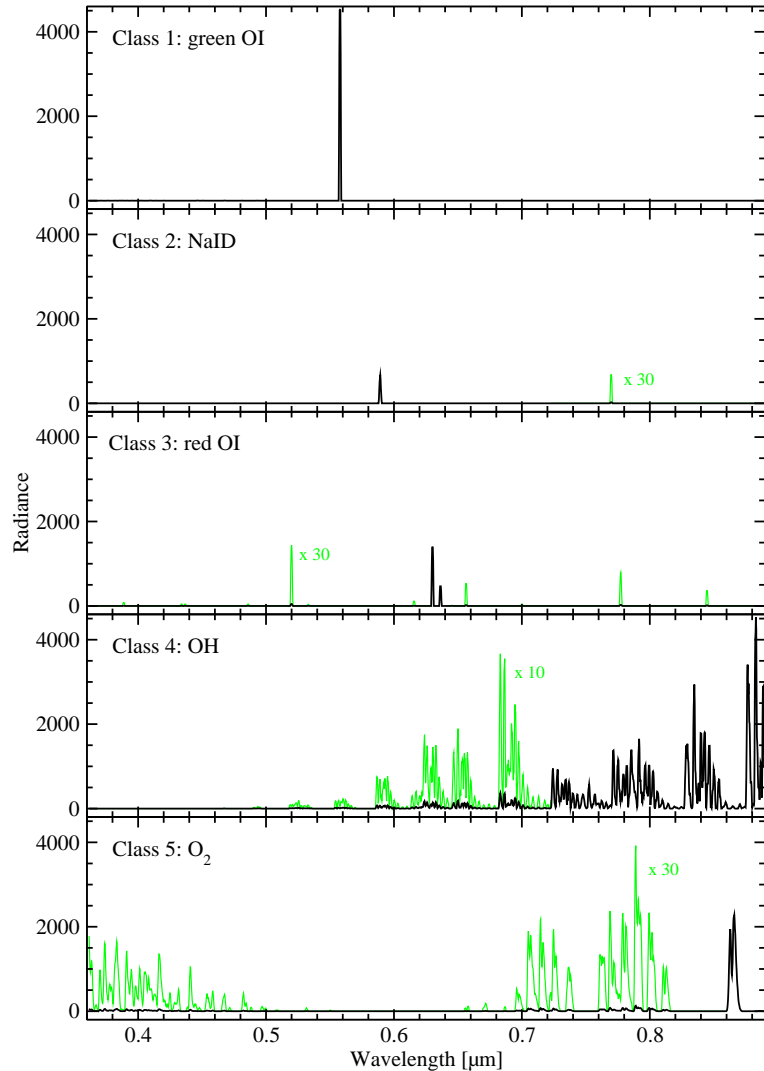


Figure 25: Variability classes for airglow emission lines. The following groups are defined: (1) green O I, (2) Na ID, (3) red O I, (4) OH, and (5) O₂. The weak lines (green curves) are scaled by a factor of 30 for Na ID, red O I, and O₂, and a factor of 10 for OH.

ESO	The Cerro Paranal Advanced Sky Model	Doc:	VLT-MAN-ESO-19550-5339
		Issue:	Issue 1.1.1
		Date:	Date 2013-09-18
		Page:	53 of 80

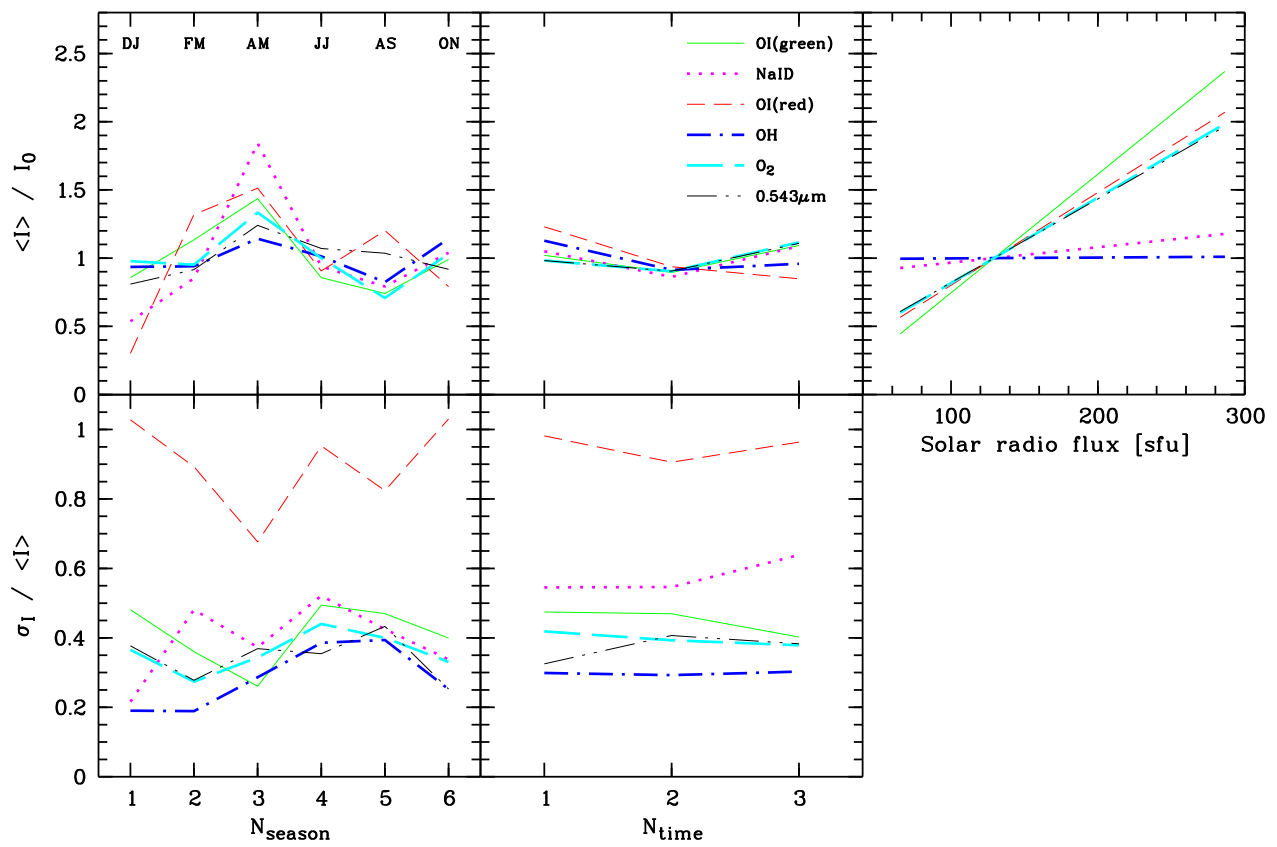


Figure 26: Variability correction for the five airglow line classes and the airglow continuum (analysed at $0.543\mu\text{m}$) of the sky model. *Upper panels*: The variability is shown as a function of the bimonthly period (1 = Dec/Jan, ..., 6 = Oct/Nov), time bin (third of the night), and solar activity measured by the solar radio flux. *Lower panels*: For bimonthly period and time bin, the relative uncertainties of the variability correction are displayed.

ESO	The Cerro Paranal Advanced Sky Model	Doc:	VLT-MAN-ESO-19550-5339
		Issue:	Issue 1.1.1
		Date:	Date 2013-09-18
		Page:	54 of 80

X)(0-0) and (0-1) bands at 1.27 and 1.58 μm are included in the model. The lines of these prominent bands were taken from the HITRAN database (see Rothman et al. [2009] and [4]). Their flux level compared to the line intensities of adjacent OH bands was roughly estimated from the IR X-Shooter spectra of the ESO sky model verification data set (see Section 7.1).

The lines of the final sky emission line list are divided into five variability classes (see Figure 25). These are (1) green OI, (2) NaID, (3) red OI, (4) OH, and (5) O₂ (cf. Patat [2008]). The emission of all classes with the exception of (3) mainly occurs in the low-temperature mesopause region. The variability of the different line types was studied by means of 1186 VLT FORS 1 night sky spectra from the ESO sky model verification data set⁴ (Patat [2008]; see Section 7.1). A majority of these spectra provides reliable data between 0.44 and 0.89 μm . As result of the variability analysis, class-dependent correction factors for the tabulated line fluxes were derived. The final correction factors are computed from several multiplicative components.

At first, a global factor for each line class is applied which returns the year, night, and solar cycle averaged zenithal flux average. In the averaging process, the solar 10.7 cm radio flux [13] distribution of the cycles 19 to 23, *i.e.* the years 1954 to 2007, was considered.

For given solar radio fluxes deviating from the mean value of 129 solar flux units (sfu = 0.01 MJy), another correction factor is computed by a polynomial of first order with individual constant and slope for each line type. The OI lines with slopes of about 0.01 sfu⁻¹ show the strongest dependence on solar activity (see Figure 26). On the other hand, the OH lines are not significantly correlated with the solar radio flux. Since the 1186 FORS 1 spectra studied, only cover the period between April 1999 and February 2005, the solar flux correction becomes less reliable for radio fluxes below 95 and above 228 sfu, *i.e.* for fluxes typical of solar activity minima and particularly strong maxima.

The dependence of the line intensities on the period of the year is treated in the same way as it is done for the molecular radiance and transmission spectra (Section 6.2.5 and 6.1), *i.e.* the year is divided into six two-month periods starting with Dec/Jan. Moreover, the night is always divided in three periods of equal length. This subdivision results in 28 bins if less specific averages over the entire year and/or night are also considered. The corresponding flux correction factors and their uncertainties were derived from the flux distribution of the different line types in these bins. The strongest seasonal variations with a maximum intensity ratio of 3.4 and 5.0 are found for the NaID and red OI lines with global maxima in autumn and global minima in summer (see Figure 26). In contrast, the OH lines show variations by a factor of only about 1.4 over the year. The flux variations over the night are smaller (see Figure 26). Averaged over the year, a dynamical range of 20 to 30% is typical. However, for a given bimonthly period, the variation can be distinctly larger (see Noll et al. [2012]). On average, the weakest lines are found in the middle of the night. In contrast to the neglected, small nocturnal variations of the molecular emission of the lower atmosphere (see Section 5.4), the significant night-time variability of the airglow lines justifies its inclusion in the sky model.

The line fluxes rise with increasing zenith distance by the increase of the projected emission layer width. This behaviour is expressed by the van Rhijn function

$$\frac{I(z)}{I(0)} = \left(1 - \left(\frac{R \sin(z)}{R + h}\right)^2\right)^{-0.5} \quad (5)$$

⁴Using the same data for building a model and verifying it is a somehow unsatisfying situation. However, the airglow analysis requires a very large data set for the observing site due to the high number of parameters that influence the airglow intensity. So far, the only suitable data are those of Patat [2008], which belong to the sky model verification data. Nevertheless, an independent comparison could be performed with photometric data from the literature discussed in Section 7.3.

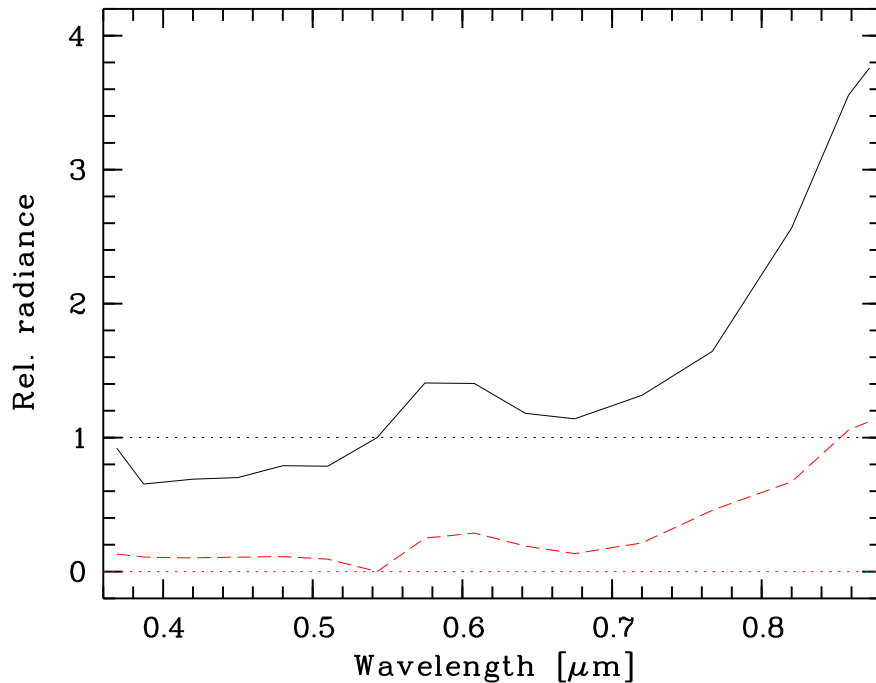


Figure 27: Optical airglow/residual continuum (solid line) and its variability (dashed line) relative to the reference wavelength $0.543 \mu\text{m}$.

(van Rhijn [1921]). Here, z , R , and h are the zenith distance, the Earth's radius, and the height of the emitting layer above the Earth's surface, respectively. Consequently, the maximum airmasses for a given zenith distance are lower for higher layers.

Finally, the airglow intensity is affected by scattering and absorption in the lower atmosphere. Since the airglow emission is distributed over the entire sky, the scattering by molecules and aerosols can be treated in a similar way as described in Section 6.2.3. The 3D scattering calculations resulted in a parametrisation of the effective extinction that only depends on the target zenith distance (see Noll et al. [2012]). The Cerro Paranal extinction curve (Patat et al. [2011]) was used for the conversion from optical depths to wavelengths. For most zenith distances relevant for astronomical observations, the effective extinction by scattering is close to zero. The molecular absorption is estimated for the target airmass by using the list of airglow line absorptions for the given meteorological conditions as provided by Module 1a (see Section 2.1). The effective line transmissions are derived for airglow line shapes that are assumed to be produced by thermal Doppler broadening only. This assumption is also used for the calculation of the sky model output spectra. For low resolution spectra, line absorption tends to be lower than continuum absorption due to the low chance to find an airglow line at the centre of a strong absorption feature. An exception are bands of O_2 ground state transitions like (b-X)(0-0) at $0.76 \mu\text{m}$ and (a-X)(0-0) at $1.27 \mu\text{m}$, which suffer from strong self-absorption.

ESO	The Cerro Paranal Advanced Sky Model	Doc:	VLT-MAN-ESO-19550-5339
		Issue:	Issue 1.1.1
		Date:	Date 2013-09-18
		Page:	56 of 80

6.2.7 Airglow continuum

The airglow continuum is the least understood emission component of the night sky. In the optical, the best-documented process is a chemiluminescent reaction of nitric oxide (NO) and atomic oxygen in the mesopause region as proposed by Krassovsky [1951] (see also Sternberg & Ingham [1972]; von Savigny et al. [1999]; Khomich et al. [2008]). Reactions of NO and ozone could be important for the airglow continuum at red to near-IR wavelengths (Clough & Thrush [1967]; Kenner & Ogryzlo [1984]). Finally, a pseudo continuum by molecular band emission of excited FeO (West & Broida [1975]) appears to be an important component of the continuum between 0.55 and 0.65 μm (Jenniskens et al. [2000]; Evans et al. [2010]; Saran et al. [2011]).

The airglow continuum is treated in a similar way as the airglow emission lines (see Section 6.2.6). Taking the 874 FORS 1 spectra of the ESO sky model verification data set observed with the Moon below the horizon (see Section 7.1), an average continuum for the solar cycles 19 to 23 was derived in 16 continuum windows (see Figure 27; see also Noll et al. [2012] for more details) after subtraction of the other sky model components. For the near-IR, this was done in 27 windows by means of 26 X-Shooter spectra with sufficient signal-to-noise ratio belonging to the same data set. Since these spectra are probably contaminated by straylight from the K band (see Vernet et al. [2011]), the derived residual continuum should be only considered as a rough upper limit of the airglow continuum. Due to the low number of spectra and additional serious uncertainties in the flux calibration (see Section 7.1), the mean X-Shooter spectrum was scaled to be consistent with the J - and H -band OH emission line intensities of the sky model. The continuum is particularly uncertain in wavelength ranges with very low atmospheric transmission (*e.g.* at about 1.4 μm). For wavelengths beyond 2 μm , it is set to zero, since a possible airglow continuum is negligible (and probably undetectable) due to the strong emission of molecules in the lower atmosphere and the thermal telescope/instrument radiation at these wavelengths (see Section 6.2.5 and 6.2.4). The relatively low number of FORS 1 spectra that provide reliable fluxes shortwards of 0.44 μm also cause higher uncertainties in this wavelength range (see Noll et al. [2012]). Regardless of the uncertainties in the near-UV and near-IR, the assumption of a fixed shape of the airglow continuum is a good approximation at least in the optical, where a substantial test data set could be analysed. Taking a reference wavelength of 0.543 μm (which is not contaminated by emission lines and is present in all FORS 1 spectra), relatively small deviations of about 10 to 20% are typical for wavelengths lower than 0.8 μm (see Figure 27). A more flexible model requires much better data sets especially in the near-UV and near-IR and is, therefore, a challenging future task.

As the treatment of the variability of the airglow continuum follows the approach for the night-sky emission lines (see Section 6.2.6), the flux level of the airglow continuum measured at 0.543 μm depends on the solar radio flux, bimonthly period, period of the night, and zenith distance (see Figure 26). The latter affects the emission layer thickness (see Equation 5) and the amount of extinction, which is computed by the same procedure as described in Section 6.2.6, except for the molecular absorption, for which the full transmission spectra from Module 1 are used (see Section 5.4). The dependence of the continuum emission on the solar radio flux is significant and comparable with the results for the O I lines. However, seasonal and nocturnal variations of the airglow continuum are relatively weak. The dynamical range for seasonal variations is about 1.5 only. The average nocturnal variation is even weaker.

ESO	The Cerro Paranal Advanced Sky Model	Doc:	VLT-MAN-ESO-19550-5339
		Issue:	Issue 1.1.1
		Date:	Date 2013-09-18
		Page:	57 of 80

7 Comparison with observational data

In this section, the quality of the sky model (see Section 6) will be evaluated by comparing it to a verification data set and results from the literature. For a more detailed discussion of the model quality in the optical wavelength regime, see Noll et al. [2012] and Jones et al. [2013]. It should be noted that the comparison was made for $\text{moonscal} = 1.2$ (Section 3 and Section 6.2.1) in agreement with Jones et al. [2013].

The discussion is organised as follows. First, the verification data set is briefly introduced (Section 7.1). Then, sky model spectra and observed spectra are compared by discussing typical examples (Section 7.2). A more systematic and quantitative comparison is shown in Section 7.3. It is based on broad-band magnitudes derived from the spectra. These magnitudes are also used to evaluate the ASM with respect to results from other sky brightness studies. Finally, the results of the comparison are summarised (Section 7.4).

7.1 Verification data set

The verification data set for the ASM provided by ESO consists of 1189 optical FORS 1 long-slit spectra (see Figure 28), 45 X-Shooter IR spectra, 7 SINFONI IR spectra, and an optical high-resolution UVES spectrum. The latter was also used for compiling the sky line atlas of Hanuschik [2003].

The FORS 1 sky spectra were collected from the ESO archive and reduced by Patat [2008]. 1186 spectra were used for the analysis, since three exposures had to be excluded because of unreliable continua. The data were taken with the low/intermediate resolution grisms 600B (12%), 600R (17%), and 300V, the latter with and without the order separation filter GG435 (57 and 14%). The set-ups cover the wavelength range from 0.365 to 0.89 μm . Wavelengths below 0.44 μm are the least covered, since only 600B and 300V spectra without GG435 can be used there. The FORS 1 spectra were taken between April 1999 and February 2005, *i.e.* observations during a phase of low solar activity are not part of the present data set (see Figure 28). The mean and standard deviation of the solar radio flux of the sample are 153 and 35 sfu respectively. The data set is also characterised by a mean elevation of 59°. The corresponding σ is only 13° and the minimum elevation corresponds to 23°. The fraction of exposures with the Moon above the horizon amounts to 26%. 29 spectra were even taken at sky positions with Moon distances below 30°. Exposures affected by strong zodiacal light contribution are almost completely absent.

The near-IR is covered by only a few high-resolution X-Shooter ($R = 3500 - 11300$ depending on slit width; wavelength range of 1 – 2 μm) and SINFONI spectra ($R = 2000 - 4000$; J , H , or K). 26 of 45 provided X-Shooter spectra could be used for the model evaluation only, since the exposure time of the other spectra was too short (< 2 min) for a reasonable signal-to-noise ratio. The useful spectra were taken at very low solar activity ($F_{10.7\text{ cm}} < 85$ sfu) between October 2009 and April 2010, mainly during the first half of the night (see Figure 29). The elevation angles vary from 35° to 85°. The mean value is 55°. The insufficient coverage of the sky model parameter space by the X-Shooter data does not allow a systematic evaluation of the sky model in the IR. Due to uncertainties in the flux calibration and the fact that the X-Shooter sky spectra tend to be much brighter than photometric data from literature (see Section 7.3) and the ASM (concerning airglow lines in particular), all spectra were divided by 1.375 being the square root of the mean OH line intensity ratio of model and observed data. Consequently, it is assumed that part of the differences are caused by flux calibration issues. Since the correction factor is very uncertain, the results of the model evalution in the near-IR (see Section 7.3) have to be taken with care. Moreover, model components derived from the X-Shooter data such as the IR airglow continuum (see Section 6.2.7) suffer from significant systematic uncertainties.

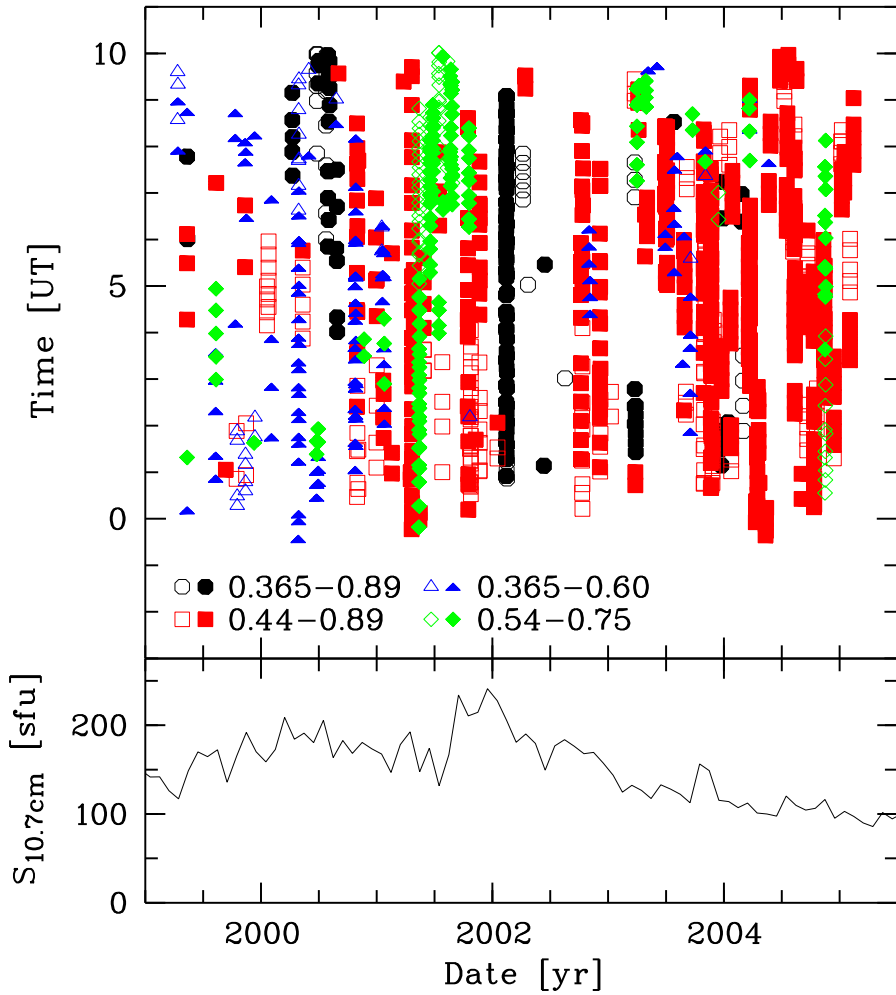


Figure 28: Date, time, and solar activity for the VLT FORS 1 observations of the Patat ([2008]) spectroscopic data set. The solar activity is given by the solar radio flux measured at 10.7 cm in sfu. The FORS 1 spectra were taken with different instrument set-ups, which are indicated by different symbols and colours. The plot legend identifies the different set-ups by their covered wavelength ranges in μm . Open symbols indicate that the data were taken with the Moon above the horizon, whereas filled symbols refer to dark-time observations.

ESO	The Cerro Paranal Advanced Sky Model	Doc:	VLT-MAN-ESO-19550-5339
		Issue:	Issue 1.1.1
		Date:	Date 2013-09-18
		Page:	59 of 80

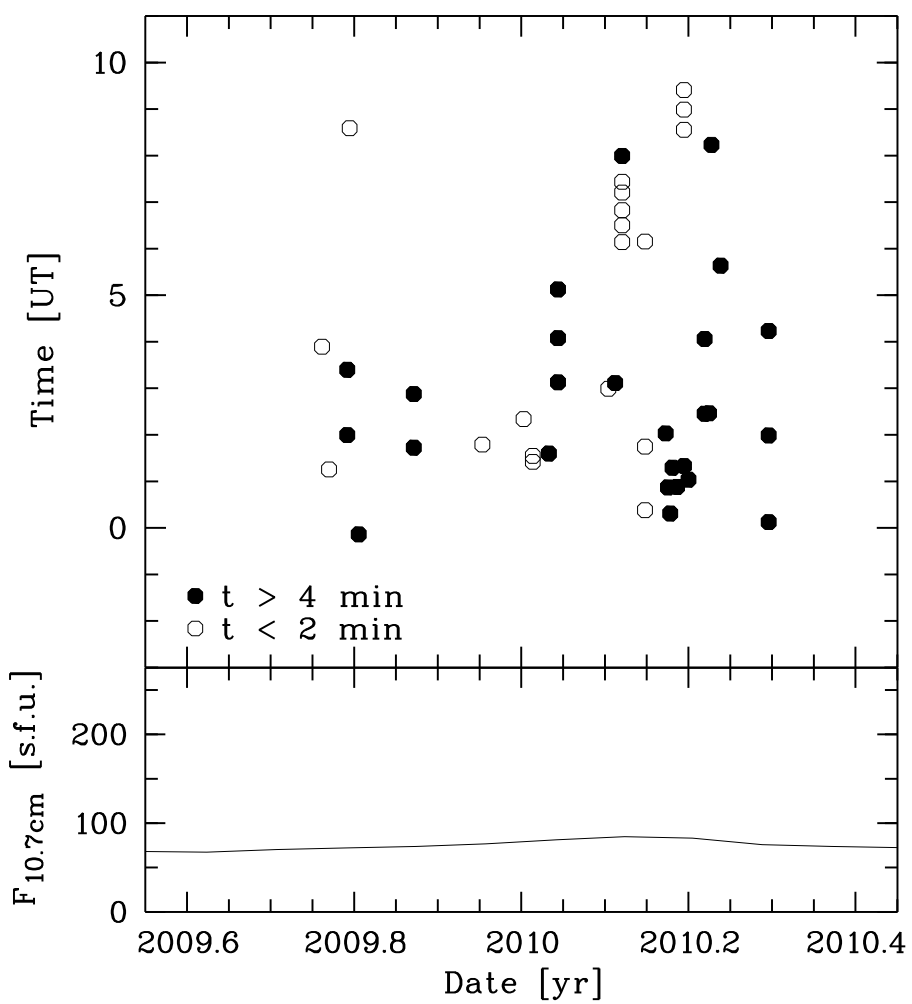


Figure 29: Date, time, and solar activity for the VLT X-Shooter observations of the sky model verification set. The solar activity is given by the solar radio flux measured at 10.7 cm in sfu. Spectra with very low exposure time that were not considered for the analysis are indicated by open symbols.

ESO	The Cerro Paranal Advanced Sky Model	Doc:	VLT-MAN-ESO-19550-5339
		Issue:	Issue 1.1.1
		Date:	Date 2013-09-18
		Page:	60 of 80

The SINFONI data set comprises 2 *J*-band, 2 *H*-band, and 3 *K*-band spectra. They were taken between April 2005 and March 2006, *i.e.* during low solar activity. 4 out of 7 spectra were obtained during a single night in April 2005. The elevation angles vary from 51° to 76°. The very low number of SINFONI sky spectra makes an evaluation of the sky model even more difficult than in the case of the X-Shooter data. Moreover, the IR continuum of the provided spectra turned out to be unreasonably bright (see Section 7.2). Therefore, SINFONI data were not used for improving the airglow continuum model (see Section 6.2.7).

7.2 Comparison of spectra

In order to evaluate the quality of the sky model, spectra were computed for input parameters describing the instrumental set-up and observing conditions for different exposures of the verification data set. A detailed description of the sky model input parameters can be found in Section 3. In the following, a few typical sky model spectra in comparison to the corresponding observed spectra are shown (Figures 30 to 38). For the optical wavelength range, the mean deviation and scatter of the sky model compared to the FORS 1 data are also shown (see Figure 33).

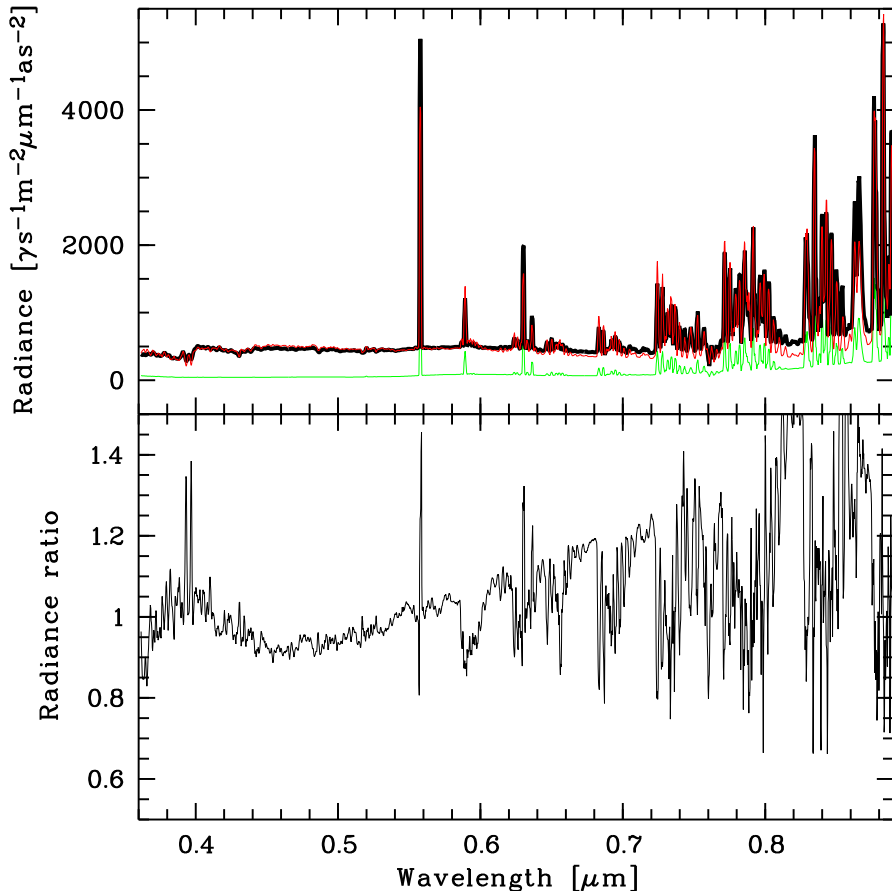


Figure 30: Comparison of the sky model (*upper panel*: thick black line) and an observed FORS 1 300V spectrum (thin red line) with moderate lunar contribution. The uncertainty of the sky model due to airglow variability is also shown (green). The *lower panel* exhibits the ratio of the sky model and the observed spectrum.

ESO	The Cerro Paranal Advanced Sky Model	Doc:	VLT-MAN-ESO-19550-5339
		Issue:	Issue 1.1.1
		Date:	Date 2013-09-18
		Page:	62 of 80

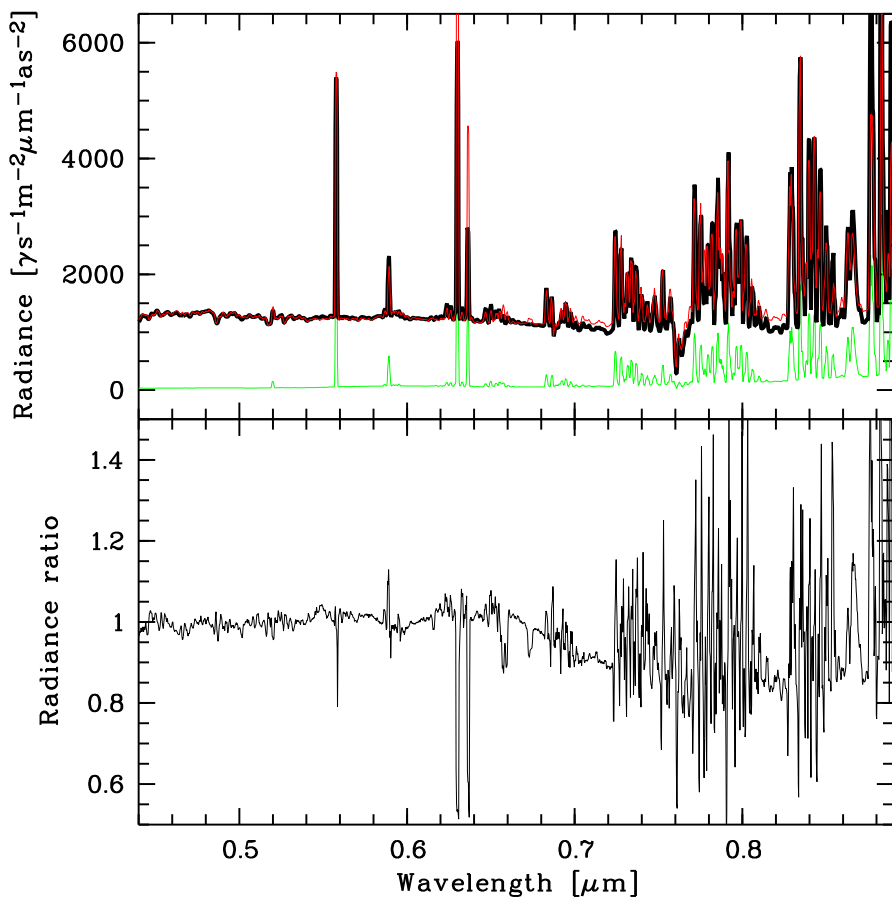


Figure 31: Comparison of the sky model and an observed FORS 1 300V+GG435 spectrum with strong lunar contribution. For an explanation of the different curves, see Figure 30.

ESO	The Cerro Paranal Advanced Sky Model	Doc:	VLT-MAN-ESO-19550-5339
		Issue:	Issue 1.1.1
		Date:	Date 2013-09-18
		Page:	63 of 80

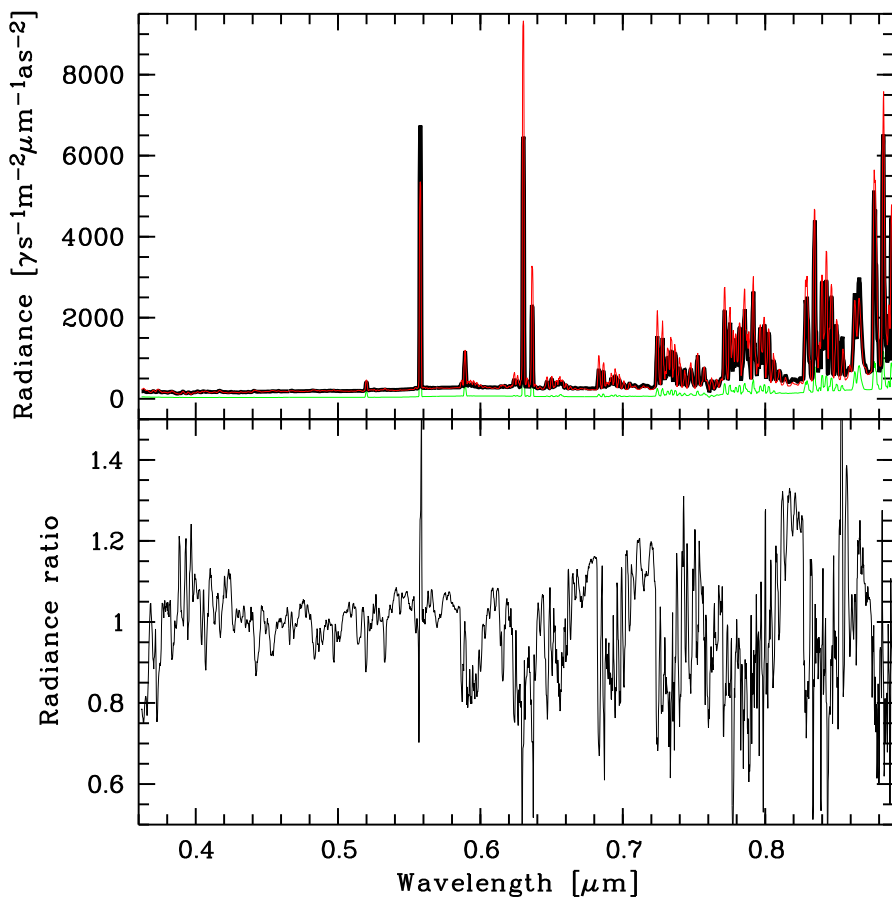


Figure 32: Comparison of the sky model and an observed FORS 1 300V spectrum without lunar contribution, but strong airglow emission lines. For an explanation of the different curves, see Figure 30.

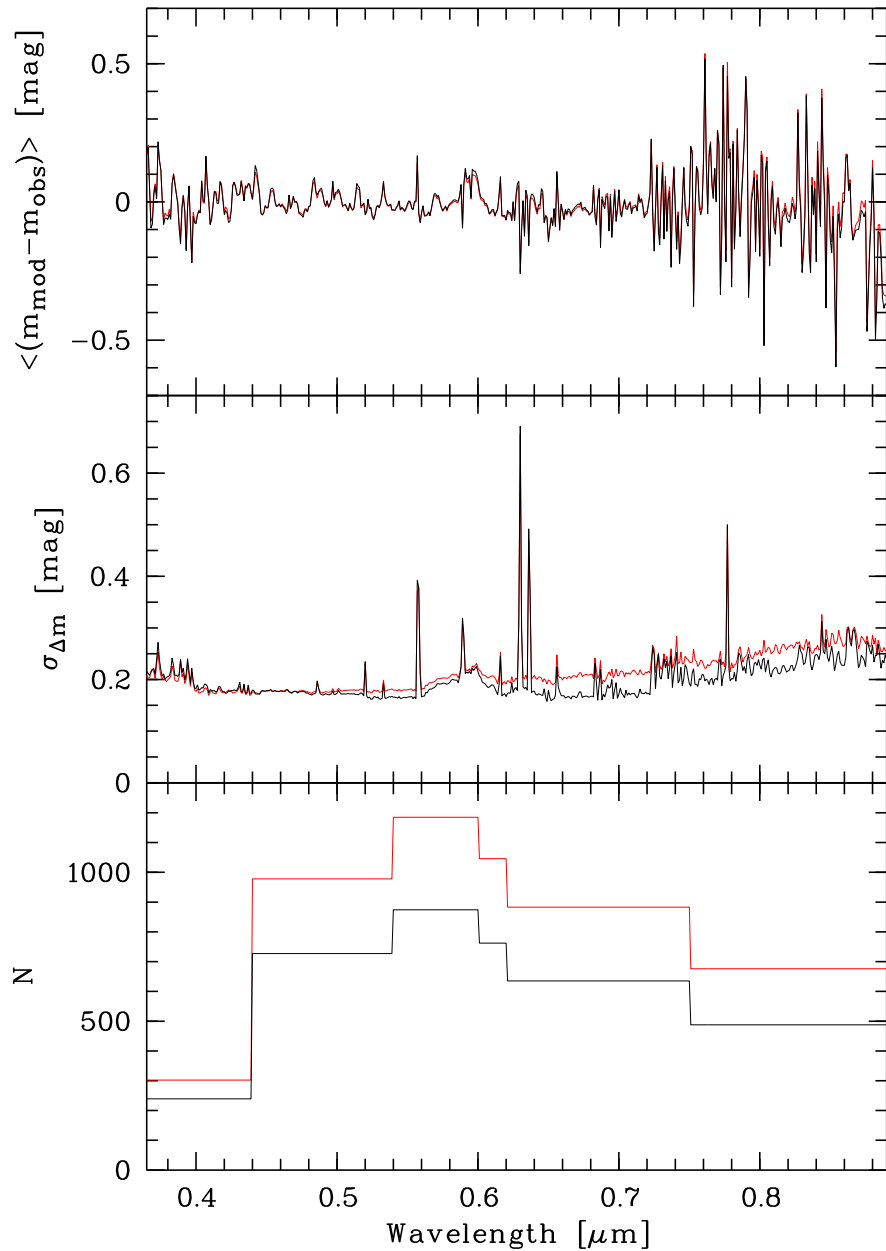


Figure 33: Deviations between the sky model and the observed FORS 1 spectra in magnitudes. The mean magnitude difference (*upper panel*), the standard deviation (*middle panel*), and the wavelength-dependent number of considered spectra (*lower panel*) are shown for 1 nm bins. Results for the full spectroscopic data set (red) and for spectra with the Moon below the horizon (black) are displayed.

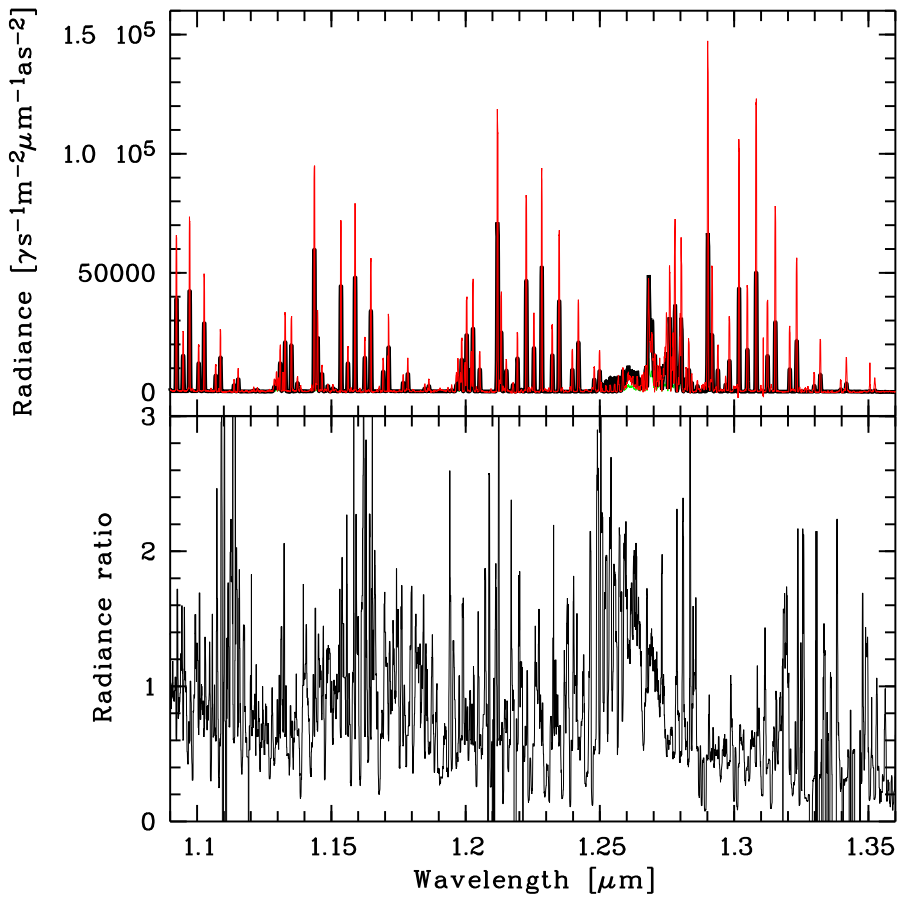


Figure 34: Comparison of the sky model and a typical observed X-Shooter spectrum in the *J* band. For an explanation of the different curves, see Figure 30. Due to the high resolution and the significant dependence of the instrumental profile on the wavelength, the radiance ratio spectrum in the lower panel is affected by strong residuals mainly originating in the line wings. Therefore, only line centre and continuum ratios are reliable.

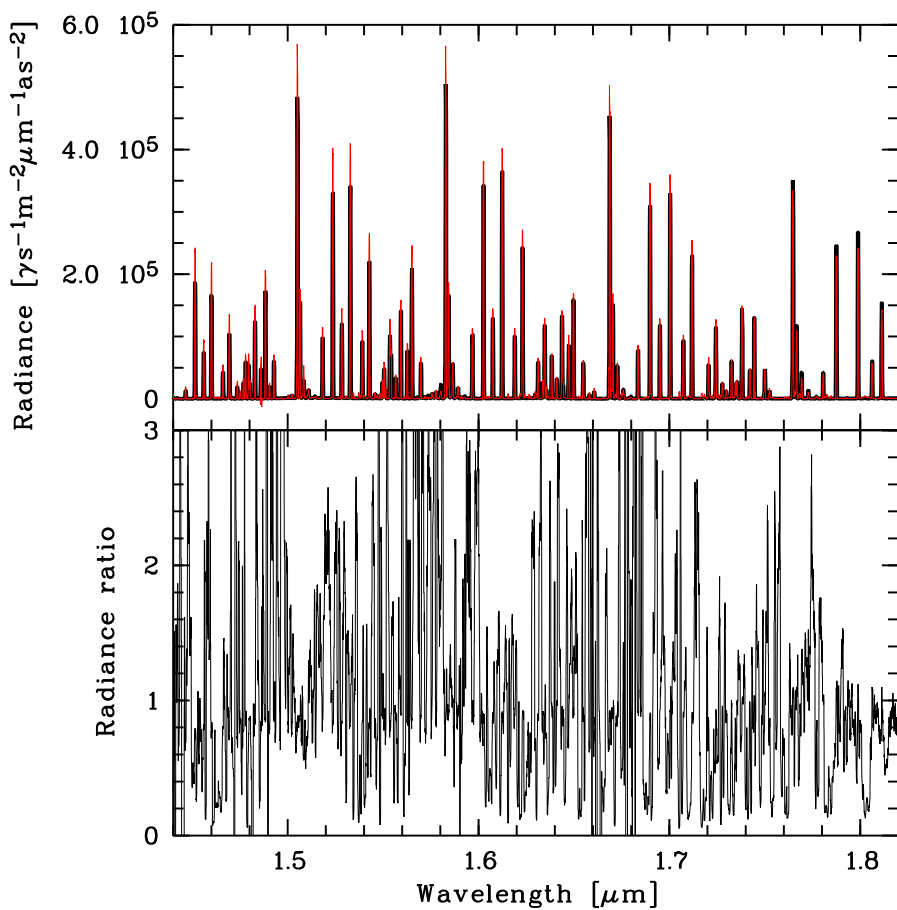


Figure 35: Comparison of the sky model and a typical observed X-Shooter spectrum in the H band (same spectrum as in Figure 34). For an explanation of the different curves, see Figure 30.

ESO	The Cerro Paranal Advanced Sky Model	Doc:	VLT-MAN-ESO-19550-5339
		Issue:	Issue 1.1.1
		Date:	Date 2013-09-18
		Page:	67 of 80

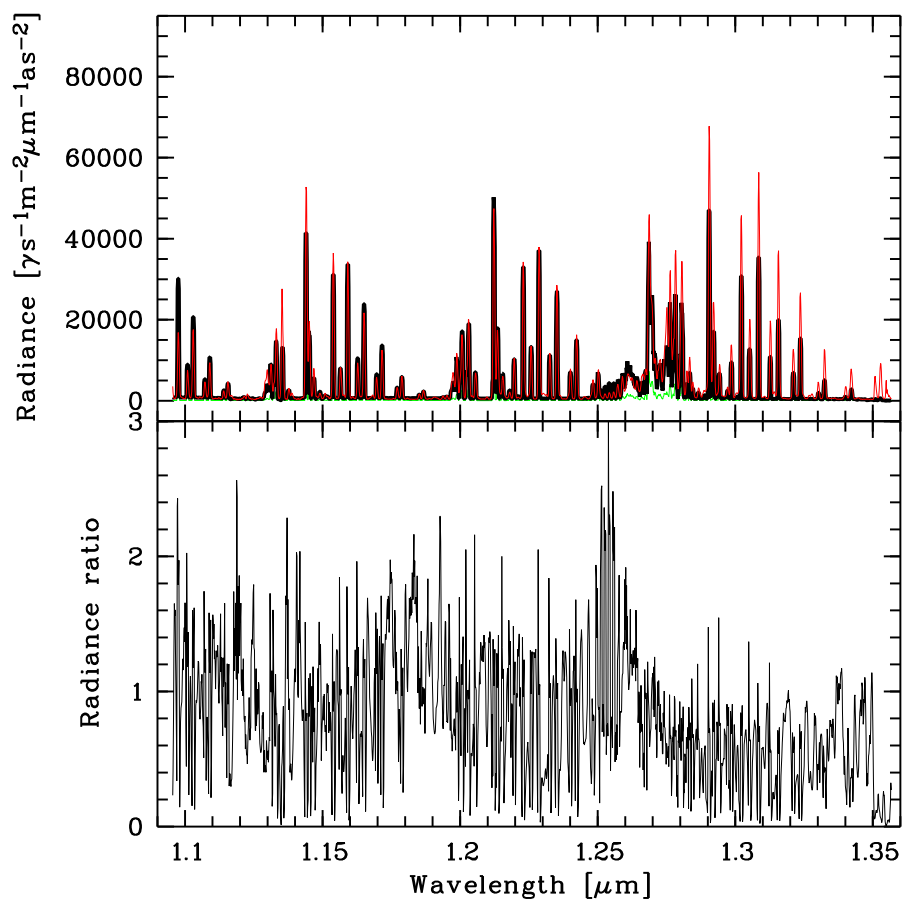


Figure 36: Comparison of the sky model and an observed SINFONI *J*-band spectrum. For an explanation of the different curves, see Figure 30.

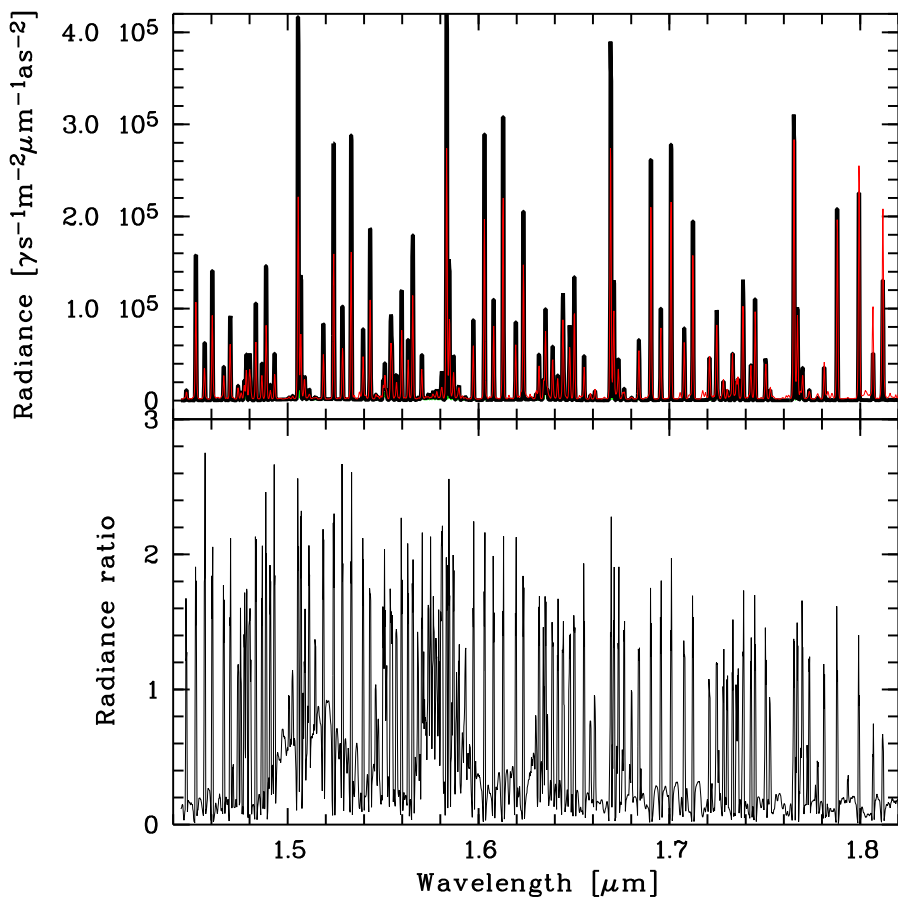


Figure 37: Comparison of the sky model and an observed SINFONI *H*-band spectrum. For an explanation of the different curves, see Figure 30.

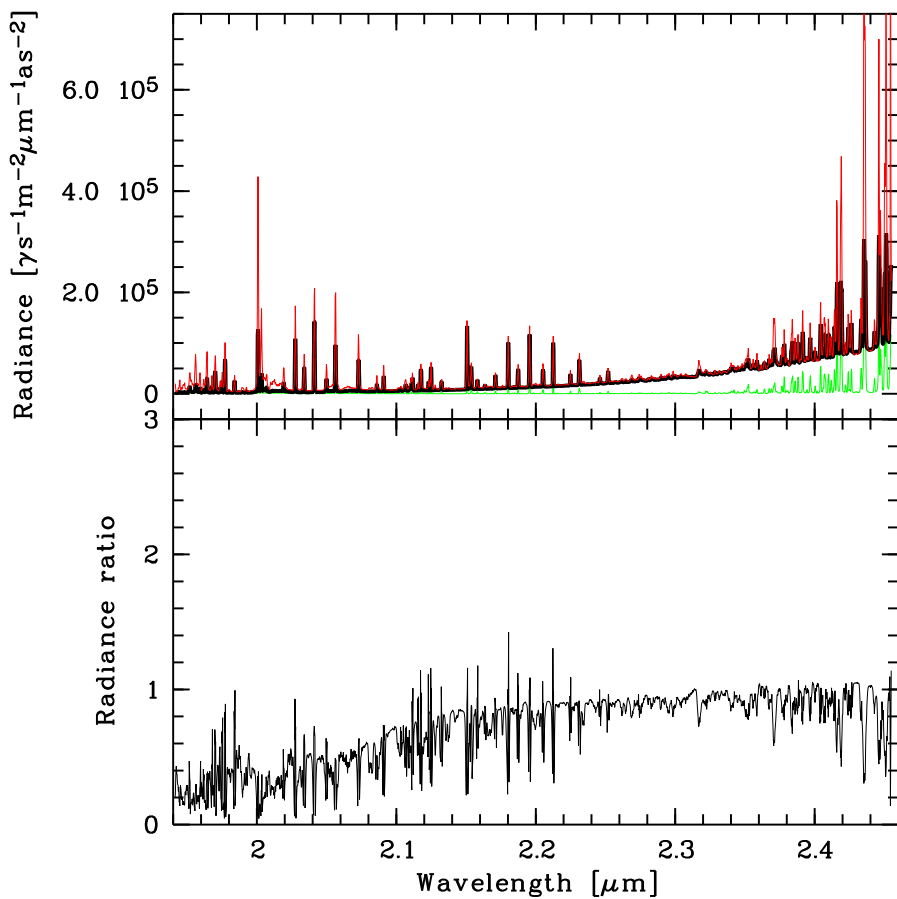


Figure 38: Comparison of the sky model and an observed SINFONI K -band spectrum. For an explanation of the different curves, see Figure 30.

ESO	The Cerro Paranal Advanced Sky Model	Doc:	VLT-MAN-ESO-19550-5339
		Issue:	Issue 1.1.1
		Date:	Date 2013-09-18
		Page:	70 of 80

In the optical, the relevant sky model components are scattered moonlight, scattered starlight, zodiacal light, and airglow lines and continuum of the upper atmosphere (see Section 6). Figures 30 to 32 compare typical 300V FORS 1 spectra with moderate Moon contribution, strong Moon contribution, and no Moon but strong airglow lines to the corresponding sky model. For 300V spectra without order separation filter, there can be a slight ($\lesssim 10\%$) contamination by the second order spectrum in the near-IR. However, this does not affect the quality of the sky model (see Section 7.3), because of the small number of involved spectra and the exclusion of these data from the derivation of the airglow continuum. Despite of the very different observing conditions, the three figures demonstrate that the sky model agrees reasonably well with the observed spectra.

For a more systematic comparison, Figure 33 shows the mean and standard deviation of the magnitude differences between model and FORS 1 data for the entire sample and a subset with the Moon above the horizon. The systematic model deviations (upper panel) are close to zero. This is very satisfying, but not unexpected, since the airglow line and continuum components were derived based on the FORS 1 spectra. Therefore, the real accuracy of the model depends on the quality of the flux calibration of the Patat [2008] data. Uncertainties are expected to be in the order of 10%. The standard deviation of the magnitude differences (middle panel) indicates a model uncertainty of about 20% for dark-time conditions. The continuum uncertainty ranges from 0.16 to 0.24 mag in this case. Including observations with scattered moonlight, these values change to 0.17 and 0.27 mag. The higher uncertainties at redder wavelengths can be explained by the increasing importance of scattering at aerosols and surface reflectance, which tend to vary (see Section 6.2.1). The strong lines in the standard deviation spectrum suggest that atomic lines of the thermospheric ionosphere are not well predicted by the sky model. This can be explained by their sensitivity to geomagnetic disturbances (see Roach & Gordon [1973]), which are difficult to model. The relatively broad feature at about $0.6\mu\text{m}$ is probably caused by the FeO pseudo continuum (see Section 6.2.7). These bands show very strong variation, which is not considered by the airglow continuum model, so far. Finally, the middle panel of Figure 33 does not exhibit strong signatures of OH bands, which indicates a good quality of the OH variability model (see Section 6.2.6).

In the near-IR, sky spectra are dominated by OH and O₂ airglow emission lines. The continuum components are very weak. This wavelength range is covered by the X-Shooter spectra of the sky model verification data set. Figures 34 and 35 show the *J* and *H* band wavelength ranges of such a spectrum. The OH lines of the model tend to be fainter than those of the observed spectra. As already described in Section 7.1, this is a general, unsatisfying feature of the X-Shooter spectra. Moreover, the ratio of the model and X-Shooter OH intensities appears to depend on wavelength. In the *H* band the deviations are small (see upper panel of Figure 35). In contrast, in the *J* band the deviations are large and they grow with increasing wavelength. The relation between OH intensitiy ratio and wavelength is not fixed for the sample of X-Shooter spectra. However, the larger deviations for the *J* band is a general trend. As already discussed, flux calibration issues and shortcomings of the OH model used could explain the differences. Interestingly, in the *J* band, an increasing difference between model and X-Shooter spectrum with increasing wavelength is also clearly present for the continuum. The shape of the continuum was derived from the X-Shooter data set, which reduces the wavelength-dependent deviations at least on average. In Figure 34, the modelled O₂ band at $1.27\mu\text{m}$ is brighter than the observed one. Although the X-Shooter spectra were used to scale the IR O₂ bands to the OH bands of the average spectrum, individual spectra can show significant differences in the deviations from the model for OH and O₂ lines, since these lines belong to different variability classes (see Section 6.2.6). The quality of the variability correction for the IR O₂(a-X) bands, using results for the O₂(b-X)(0-1) band at $0.865\mu\text{m}$ (a different electronic transition), cannot currently be evaluated, since the available X-Shooter data set is too small for an independent variability study.

Figures 36 to 38 show SINFONI spectra for the *J*, *H*, and *K*-band. For the airglow lines, the correspondence with the sky model is not bad. However, if all SINFONI spectra are considered, the sky model tends to show

ESO	The Cerro Paranal Advanced Sky Model	Doc:	VLT-MAN-ESO-19550-5339
		Issue:	Issue 1.1.1
		Date:	Date 2013-09-18
		Page:	71 of 80

Table 3: Mean values and standard deviations for magnitude differences between the sky model and the FORS 1 verification data. The standard deviation of the magnitudes of the observed data σ_{obs} is also shown for each filter. Moreover, mean values $\langle \Delta m_w \rangle$ and standard deviations $\sigma_{\Delta m,w}$ for magnitude differences between the Moon phase related data of Walker and the Patat data are displayed. Results are listed for the full and a dark-time sample.

Filter	All						No Moon					
	N	$\langle \Delta m \rangle$	$\sigma_{\Delta m}$	σ_{obs}	$\langle \Delta m_w \rangle$	$\sigma_{\Delta m,w}$	N	$\langle \Delta m \rangle$	$\sigma_{\Delta m}$	σ_{obs}	$\langle \Delta m_w \rangle$	$\sigma_{\Delta m,w}$
U	302	+0.048	0.202	0.518	-0.113	0.725	239	+0.040	0.211	0.214	-0.059	0.703
B	302	+0.047	0.168	0.557	+0.269	0.430	239	+0.046	0.171	0.182	+0.196	0.407
V	978	-0.006	0.184	0.553	+0.356	0.409	727	+0.000	0.172	0.250	+0.244	0.322
R	1046	-0.010	0.194	0.447	+0.169	0.365	762	-0.012	0.179	0.260	+0.083	0.287
I	839	-0.022	0.231	0.365	+0.413	0.326	615	-0.043	0.208	0.287	+0.365	0.294

fainter lines. A striking result of the comparison is the much weaker model continuum. In particular, in the H band, the offset is very large. In some parts of the band, the model continuum reaches about 20% of the corresponding SINFONI flux only. This raises the question whether the continua of the SINFONI spectra are reliable. In Section 7.3, this issue is discussed in more detail. In the K -band, the quality of the correspondence also depends on a good knowledge of the thermal emission by the telescope and the instrument, which dominates the continuum (see Section 6.2.4). At the blue end of the K -band, differences in the temperature cause higher relative deviations than at longer wavelengths, as indicated by Figure 38. Moreover, molecular emission of the lower atmosphere starts to contribute (see Section 6.2.5). Since the bimonthly atmospheric mean profiles of the model can only roughly characterise the weather conditions during the exposure, the observed deviations at the red margin of the filter are not unexpected. Finally, the computed CO₂ band intensities at about 2 μm are too weak, most probably due to too low temperatures in the atmospheric temperature profile.

7.3 Comparison of photometry

To perform a more quantitative comparison of sky model and observed data, magnitudes derived from broad-band filter fluxes will be used in the following. Specifically, the standard photometric system consisting of U , B , V , R , I , J , H , and K is applied. For each spectrum of the verification data set and its corresponding sky model, only a subset of filters can be used. A requirement is that the spectrum covers most of the filter curve. An exception is the U filter, which extends below 0.365 μm, which is the lower wavelength limit of the bluest spectral set-up.

Figure 39 and Table 3 show the results for the FORS 1 spectra. Differences between sky model and observed fluxes are given as magnitudes. Only a small fraction of the spectra contribute to the mean values and standard deviations of the U and B filters. Most spectra cover the range of the V , R , and I filters. For all filters, the mean magnitude differences are very small (< 0.05 mag). No serious systematic deviations can be identified. The standard deviations $\sigma_{\Delta m}$ are relatively similar for the different filters. They range from 0.17 for the V -band to 0.23 for the I band. Consequently, the accuracy of the sky model is in the order of 20%. These values can be compared to the magnitude variations in the measured data σ_{obs} , which correspond to the $\sigma_{\Delta m}$ for a sky model of time-invariant flux. In this case, the deviations are distinctly larger. They range from 0.37 to 0.56. However, these large deviations are mainly due to observations characterised by a strong lunar contribution. Here, the flux level is very different from the sample average. Therefore, a subsample of spectra with the Moon

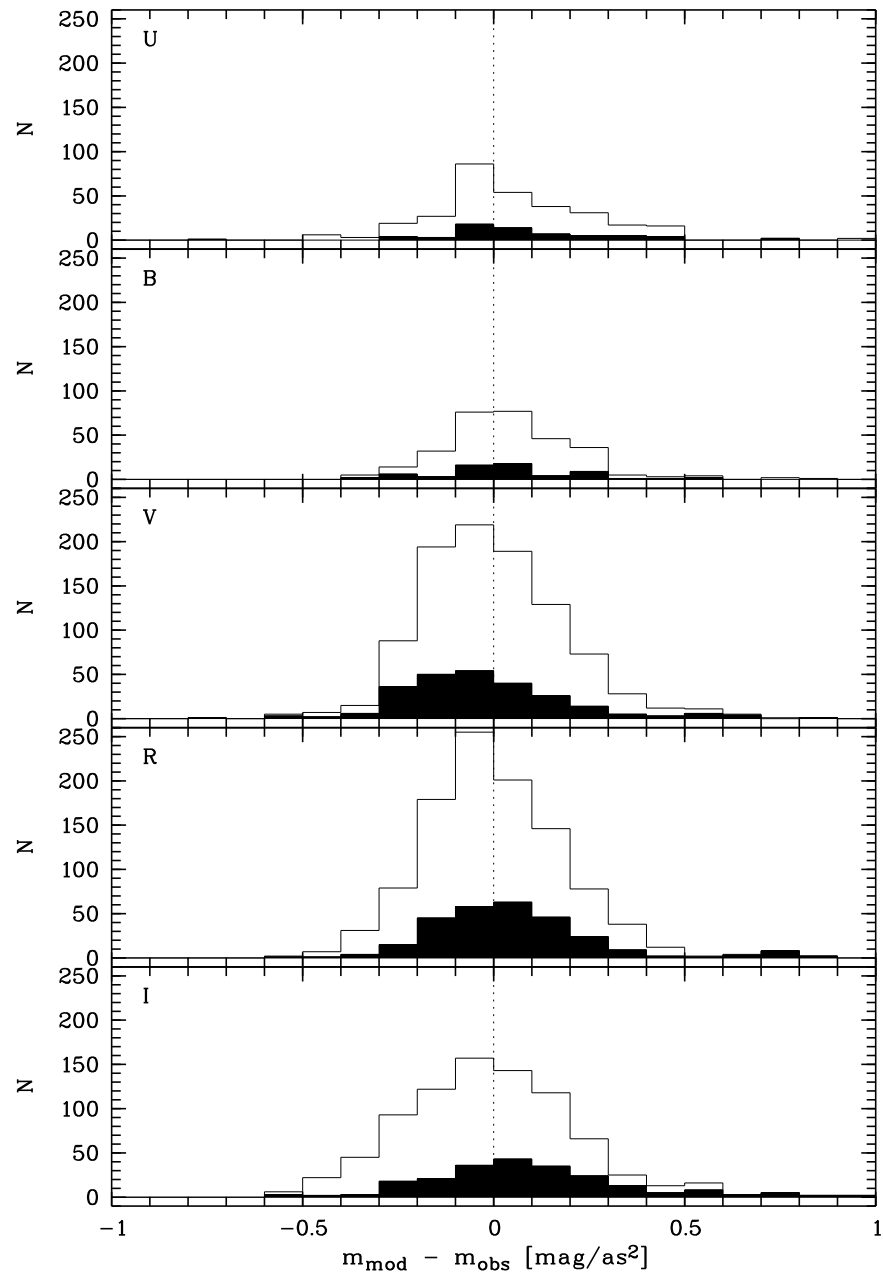


Figure 39: Histograms for the deviations of the sky model from the FORS 1 data in mag for the filters U , B , V , R , and I . The filled histograms show only data with the Moon above the horizon.

ESO	The Cerro Paranal Advanced Sky Model	Doc:	VLT-MAN-ESO-19550-5339
		Issue:	Issue 1.1.1
		Date:	Date 2013-09-18
		Page:	73 of 80

Table 4: Mean values and standard deviations for magnitude differences between the sky model and the X-Shooter verification data. The standard deviation of the magnitudes of the observed data σ_{obs} is also shown for each filter.

Filter	N	$\langle \Delta m \rangle$	$\sigma_{\Delta m}$	σ_{obs}
J	26	+0.545	0.298	0.352
H	26	+0.119	0.340	0.375

below the horizon was also studied. For this subsample, the mean offset only slightly changes compared to the full data set. Selecting only dark-time observations results in $\sigma_{\Delta m}$ of the ASM between 0.17 and 0.21, which indicates a moderate improvement for V to I and a slight deterioration for U and B . Even though the quality of a time-invariant sky model would improve in all filters for dark-time conditions, deviations between 0.25 and 0.29 at wavelengths where airglow lines and continuum dominate are still significantly higher than those obtained for the ASM. The differences show the advantage of having a model with variable airglow emission. The improvement would even be better if the airglow continuum was modelled in a more sophisticated way (see Section 7.2).

For a long time, ESO has been using the Moon-phase dependent, photometric sky brightness table of Walker [1987] as basis for the ETC sky background calculations in the optical. Computing the Walker magnitudes for the observing conditions of the FORS 1 data set then allows us to evaluate the quality of this simple but extensively used model compared to the ASM (see also Noll et al. [2012]). The results of the comparison of the Walker model with the observed data are shown in Table 3. The mean offset and the standard deviation are provided by $\langle \Delta m_w \rangle$ and $\sigma_{\Delta m,w}$, respectively. In general, the Walker model performs significantly worse than the ASM. Excluding the U band, the offsets are between 0.17 and 0.41 and the scatter is about 0.4 for the full sample. The values only slightly improve for dark-time conditions. Interestingly, $\sigma_{\Delta m,w}$ is better than σ_{obs} of the time-invariant model for the full sample, but significantly worse for the dark-time subsample. This unsatisfactory performance of the Walker model is caused by the unconsidered, varying amount of scattered moonlight during a Moon phase. Even for phases close to Full Moon, dark-time observations are possible. This result implies that a Moon-phase dependent model is not suitable to provide reliable sky brightness estimates. The scattered moonlight model of the ASM (see Section 6.2.1) performs significantly better in this respect.

A similar comparison as for the FORS 1 data is shown for the X-Shooter near-IR data in Table 4. For the 26 X-Shooter spectra used, the table indicates the deviations in the J and H band of the sky model from the observed data. On average, the sky model is 0.55 and 0.12 mag, respectively, fainter. This significant difference is not unexpected, since the calibration of the X-Shooter spectra (see Section 7.1) and the OH line model (see Section 6.2.6) are relatively uncertain. On the other hand, Table 3 suggests that the variability in the near-IR sky brightness can at least in part be reproduced by the sky model, since the standard deviation $\sigma_{\Delta m}$ derived from the difference between model and observed data is lower than the scatter in the sky brightnesses of the X-Shooter data σ_{obs} for both near-IR filters.

The deviations of the sky model from the SINFONI verification data are listed in Table 5. Values are provided for each spectrum individually, since their number is too small for computing statistically significant averages. The Δm values of the spectra taken through the J and H filter are completely different. Spectrum 1 and 6 indicate deviations of (+0.40 and +1.16) that would be extremely rare if the typical $\sigma_{\Delta m}$ of the optical were assumed (see Table 3). On the other hand, the X-Shooter data indicate a $\sigma_{\Delta m}$ of about 0.3 and an offset of the model towards fainter magnitudes. If the systematic uncertainties are comparable to those of the comparison between sky

ESO	The Cerro Paranal Advanced Sky Model	Doc:	VLT-MAN-ESO-19550-5339
		Issue:	Issue 1.1.1
		Date:	Date 2013-09-18
		Page:	74 of 80

Table 5: Deviations between the sky model and the SINFONI spectra of the verification data set.

ID	Filter	Date	Time [UT]	Δm [mag]
1	<i>H</i>	2005-04-02	23:59	+0.40
2	<i>H</i>	2005-04-03	06:31	-0.13
3	<i>K</i>	2005-04-03	07:13	+0.39
4	<i>K</i>	2005-04-03	10:04	+0.26
5	<i>K</i>	2005-08-11	00:53	+0.17
6	<i>J</i>	2005-10-31	00:33	+1.16
7	<i>J</i>	2006-03-13	06:04	+0.25

Table 6: Typical sky model and literature night-sky brightnesses in mag arcsec⁻² for zenith, New Moon, faint zodiacal light, and different 10.7 cm solar radio fluxes $S_{10.7}$ in sfu.

Source	Site	$S_{10.7}$	<i>U</i>	<i>B</i>	<i>V</i>	<i>R</i>	<i>I</i>	<i>J</i>	<i>H</i>	<i>K</i>
Benn & Ellison [2007]	La Palma	80	22.0	22.7	21.9	21.0	20.0	16.6	14.4	12.0
Walker [1987]	Cerro Tololo	90	22.0	22.7	21.8	20.9	19.9			
Krisciunas et al. [2007]	Cerro Tololo	130	22.1	22.8	21.8	21.2	19.9			
Mattila et al. [1996]	La Silla	150		22.8	21.7	20.8	19.5			
Patat [2008]	Cerro Paranal	160	22.4	22.7	21.7	20.9	19.7			
Cuby et al. [2000]	Cerro Paranal	170						16.5	14.4	13.0
Patat [2003]	Cerro Paranal	180	22.3	22.6	21.6	20.9	19.7			
Sky model	Cerro Paranal	90	22.3	22.9	22.0	21.2	19.8	16.8	14.4	12.8
		130	22.1	22.8	21.8	21.0	19.7	16.7	14.4	12.8
		180	21.9	22.6	21.6	20.9	19.6	16.5	14.4	12.8

model and X-Shooter data, the deviations found could be explained. At least the airglow continuum emission in the SINFONI data (which is in part several times brighter than the continuum derived from the X-Shooter spectra; see Section 7.2) appears to be much too bright, which suggests that instrumental and calibration issues could play a role. Moreover, systematic errors in the OH line model based on Rousselot et al. [2000] could contribute to the discrepancies. In conclusion, there are too many uncertainties in data and model in order to reliably quantify the deviations between the ASM and the corresponding verification data set for the near-IR regime.

Finally, the sky model is compared to literature data unrelated to the verification data set. To this end, magnitudes in the eight broad-band filters *U* to *K* were calculated using standardised observing conditions. Specifically, zenith, New Moon, ecliptic pole, annual and nocturnal average, mean solar activity for the cycles 19 to 23, *i.e.* 130 sfu, a telescope/instrument emissivity of 0.17 (corresponding to an apparent value of 0.2; see Section 6.2.4), and a temperature of 290 K were assumed. The resulting magnitudes are provided in Table 6. For a better comparison with published data, the table also contains sky model results for 90 and 180 sfu. The reference data in Table 6 originate from Mattila et al. [1996] for La Silla, Walker [1987] and Krisciunas et al. [2007] for Cerro Tololo, Benn & Ellison [2007] for La Palma, and Patat [2003], Patat [2008] and Cuby et al. [2000] for Cerro Paranal.

ESO	The Cerro Paranal Advanced Sky Model	Doc:	VLT-MAN-ESO-19550-5339
		Issue:	Issue 1.1.1
		Date:	Date 2013-09-18
		Page:	75 of 80

A comparison of the sky model with the Cerro Paranal data of Patat [2003] and [2008] shows good agreement. Only the U filter exhibits a deviation larger than 0.1 mag. The other telescope sites indicate differences of up to 0.2 mag for B to I and up to 0.3 mag for the U band. The relatively bad agreement of the U -band magnitudes of the sky model with published sky brightnesses could be due to the lack of spectroscopic verification data below 0.365 μm . Moreover, only 26% of the FORS verification data set (see Section 7.1) covers the wavelength range below 0.44 μm and most observations were carried out during very high solar activity (see Figure 28). The Cerro Tololo and La Palma data were taken at the solar activity minimum. Hence, the sky model is very uncertain at blue wavelengths when the solar activity is low. At this activity level, the contributions of the Moon (even if below the horizon), the zodiacal light, and scattered starlight can become relatively important. Furthermore, it is not obvious whether the set-up of the sky model matches the observed conditions sufficiently in this context. Differences in the observing site could also have an effect.

Next, the J , H , and K sky brightnesses of the sky model are compared to the results of Benn & Ellison [2007] for La Palma and Cuby et al. [2000] for Cerro Paranal. While the agreement of the model K -band magnitude with the Cuby et al. result is satisfying, the deviation from the La Palma value is about 0.8 mag. The striking observing site dependence of the K -band magnitude can be explained by the K flux dependence on telescope, instrument, and typical ambient temperature. Concerning J and H , Table 6 indicates a very good agreement between the sky model and the published sky magnitudes. The deviations are not larger than 0.1 mag. In view of the large model uncertainties in the near-IR, this is a remarkable result.

An independent option to check the quality of the sky model in the near-IR is a comparison of the continuum flux of the model and measurements from the literature at certain wavelengths. Apart from the photometry, Cuby et al. [2000] also provide continuum fluxes at 1.19 and 1.7 μm , respectively. Interestingly, their fluxes (1200 and $2300 \text{ phot s}^{-1} \text{ m}^{-2} \mu\text{m}^{-1} \text{ arcsec}^{-2}$) are significantly higher than those from the sky model (390 and $660 \text{ phot s}^{-1} \text{ m}^{-2} \mu\text{m}^{-1} \text{ arcsec}^{-2}$). On the other hand, the sky model continuum agrees much better with the measurements of Maihara et al. [1993], who derived $590 \text{ phot s}^{-1} \text{ m}^{-2} \mu\text{m}^{-1} \text{ arcsec}^{-2}$ at 1.665 μm . For similar observing conditions, the flux of the sky model continuum amounts to about $450 \text{ phot s}^{-1} \text{ m}^{-2} \mu\text{m}^{-1} \text{ arcsec}^{-2}$ at this wavelength. Relatively low near-IR continuum fluxes are also suggested by Lopez-Moreno et al. [1987] and Sobolev [1978] (see also Content [1996] for an overview). Hence, the Cuby et al. measurements are probably not representative for the near-IR. Measurements of the weak near-IR continuum can be affected by instrumental straylight (see Ellis & Bland-Hawthorn [2008]; Vernet et al. [2011]). For this reason, the continuum level tends to be instrument dependent and the sky model near-IR residual continuum is probably still higher than the true airglow continuum.

7.4 Conclusions

We have analysed the quality of the current version of the ASM by direct comparison of model and observed spectra, the calculation of broad-band magnitudes, and the comparison of these values to published data. Overall, the sky model provides good results. The best wavelength range is the optical, where the airglow variability was studied. Typical uncertainties are in the order of 20%. The most crucial component in this wavelength range is scattered moonlight. At least for a moderate lunar contribution and photometric observing conditions, the sky model allows good predictions. In any case, the sophisticated handling of scattered moonlight in the ASM provides significantly better results than the Moon-phase dependent Walker [1987] sky brightness table, which ESO has been using for ETC applications. The inclusion of the airglow variability in the sky model significantly improves the model quality in the photometric bands V , R , and I compared to a very simple model with time-invariant airglow contribution. The model quality is better for OH and O₂ bands than for strongly varying

ESO	The Cerro Paranal Advanced Sky Model	Doc:	VLT-MAN-ESO-19550-5339
		Issue:	Issue 1.1.1
		Date:	Date 2013-09-18
		Page:	76 of 80

oxygen and sodium atomic lines, which fortunately cover only a very small fraction of the optical regime.

The quality of the airglow model strongly depends on the extent of the spectroscopic data set. A satisfying coverage of observing conditions is found for the optical, even though there is a lack of observations at low solar activity. The number of spectra is already distinctly smaller in the near-UV, which causes higher systematic uncertainties of the sky model. Even more critical is the situation in the near-IR at wavelengths beyond 0.9 μm , where data with reliable flux calibration were not available for the analysis. For this reason, the current near-IR model mainly relies on an extrapolation of the optical model, rough theoretical airglow calculations, relative fluxes from a small sample of X-Shooter spectra, and an adjustment of the model to published photometric sky brightness measurements. The most uncertain component is the near-IR airglow continuum, where it is even unclear whether it exists at all. Apart from the lack of data, instrument-specific continua usually outshine the conjectured atmospheric contributions (see *e.g.* Vernet et al. [2011]). Hence, the ASM near-IR continuum should only be considered as upper limit. Even in the optical, where a large data set is available, the airglow continuum should be taken with care, since the derived intensity of this residual continuum is very sensitive to the accuracy of the other model components (especially zodiacal light, where the wavelength dependence is only roughly known) and systematic errors in the flux calibration of the spectroscopic data. Finally, in the thermal IR the model should be more reliable than in the near-IR, since the atmospheric emission can be calculated by means of a radiative transfer code. Moreover, it appears that the ASM will preferentially be used in ETCs for this wavelength regime with user-selected amount of water vapour, which distinctly reduces the uncertainty of the thermal molecular emission model.

In summary, the advanced sky model for Cerro Paranal is a significant improvement compared to other sky background models used in ETCs, so far. Nevertheless, there are still relatively uncertain model components. For further improvements, it is required to study large data sets of well calibrated spectra, to better understand the relevant atmospheric processes, and to find more advanced modelling approaches.

ESO	The Cerro Paranal Advanced Sky Model	Doc:	VLT-MAN-ESO-19550-5339
		Issue:	Issue 1.1.1
		Date:	Date 2013-09-18
		Page:	77 of 80

ESO	The Cerro Paranal Advanced Sky Model	Doc:	VLT-MAN-ESO-19550-5339
		Issue:	Issue 1.1.1
		Date:	Date 2013-09-18
		Page:	78 of 80

References

- [2007] Benn C.R., & Ellison, S.L. 2007, La Palma technical note, 115
- [1983] Bohren, C.F., & Huffman, D.R. 1983, Absorption and Scattering of Light by Small Particles, Wiley, New York
- [1967] Clough, P.N., & Thrush, B.A. 1967, Trans. Faraday Soc. 63, 915
- [2005] Clough, S.A, Shephard, M.W., Mlawer, E.J., et al. 2005, J. Quant. Spectrosc. Radiat. Transfer, 91, 233
- [1992] Clough, S.A., Iacono, M.J., & Moncet, J.-L. 1992, J. Geophys. Res., 97, 15761
- [1996] Colina, L., Bohlin, R.C., & Castelli, F. 1996, AJ, 112, 307
- [1996] Content, R. 1996, ApJ, 464, 412
- [2006] Cosby, P.C., Sharpee, B.D., Slanger, T.G., Huestis, D.L., & Hanuschik, R.W. 2006, J. Geophys. Res., 111, A12307
- [2000] Cuby, J.G., Lidman, C., & Moutou, C. 2000, The Messenger, 101, 2
- [2008] Ellis, S.C., & Bland-Hawthorn, J. 2008, MNRAS, 386, 47
- [2010] Evans, W.F.J., Gattinger, R.L., Slanger, T.G., et al. 2010, Geophys. Res. Lett., 37, L22105
- [1998] Goldman, A., Schoenfeld, W.G., Goorvitch, D., et al. 1998, J. Quant. Spectrosc. Radiat. Transfer, 59, 453
- [2003] Hanuschik, R.W. 2003, A&A, 407, 1157
- [2000] Jenniskens, P., Lacey, M., Allan, B.J., Self, D.E., & Plane, J.M.C. 2000, Earth Moon Planets, 82/83, 429
- [2013] Jones, A.M., Noll, S., Kausch, W., et al. 2013, A&A, 560, A91.
- [1984] Kenner, R.D., & Ogryzlo, E.A. 1984, J. Chem. Phys., 80, 1
- [2008] Khomich, V.Y, Semenov, A.I., & Shefov, N.N. 2008, Airglow as an Indicator of Upper Atmospheric Structure and Dynamics, Springer, Berlin
- [2005] Kieffer, H.H., & Stone, T.C. 2005, AJ, 129, 2887
- [1991] Krisciunas, K., & Schaefer, B.E. 1991, PASP, 103, 1033
- [2007] Krisciunas, K., Semler, D.R., Richards, J., et al. 2007, PASP, 119, 687
- [1951] Krassovsky, V.I. 1951, Dokl. Akad. Nauk SSSR, 78, 669
- [1980] Levasseur-Regourd, A.-C., & Dumont, R. 1980, A&A, 84, 277
- [1998] Leinert, C., Bowyer, S., Haikala, L.K., et al. 1998, A&AS, 127, 1
- [2002] Liou, K.-N. 2002, Introduction to Atmospheric Radiation, Second Edition, Academic Press, San Diego

ESO	The Cerro Paranal Advanced Sky Model	Doc:	VLT-MAN-ESO-19550-5339
		Issue:	Issue 1.1.1
		Date:	Date 2013-09-18
		Page:	79 of 80

- [1987] Lopez-Moreno, J.J., Rodrigo, R., Moreno, F., Lopez-Puertas, M., & Monila, A. 1987, *Planet. Space Sci.*, 35, 1029
- [1993] Maihara, T., Iwamuro, F., Yamashita, T., et al. 1993, *PASP*, 105, 940
- [1974] Mies, F.H. 1974, *J. Molec. Spectrosc.*, 53, 150
- [1988] Musuda, K., Takashima, T., & Takayama, Y. 1988, *Remote Sens. Environ.*, 24, 313
- [1980] Mattila, K. 1980, *A&AS*, 39, 53
- [1996] Mattila, K., Väisänen, P., & von Appen-Schnur, G.F.O. 1996, *A&AS*, 119, 153
- [2007] Melchior, A.-L., Combes, F., & Gould, A. 2007, *A&A*, 462, 965
- [2005] Niro, F., Jucks , K., & Hartmann, J.-M. 2005, *J. Quant. Spectrosc. Radiat. Transfer*, 95, 469
- [2012] Noll, S., Kausch, W., Barden, M., et al. 2012, *A&A*, 543, A92
- [2003] Patat, F. 2003, *A&A*, 400, 1183
- [2008] Patat, F. 2008, *A&A*, 481, 575
- [2011] Patat, F., Moehler, S., O'Brien, K., at al. 2011, *A&A*, 527, A91
- [1973] Roach, F.E., & Gordon J.L. 1973, *The light of the night sky*, Reidel, Dordrecht
- [2009] Rothman, L.S., Gordon, I.E., Barbe, A., et al. 2009, *J. Quant. Spectrosc. Radiat. Transfer*, 110, 533
- [2000] Rousselot, P., Lidman, C., Cuby, J.-G., Moreels, G., & Monnet, G. 2000, *A&A*, 354, 1134
- [1966] Rozenberg, G.V. 1966. *Twilight: A Study in Atmospheric Optics*, New York: Plenum Press, 160
- [2011] Saran, D.V., Slanger, T.G., Feng, W., & Plane, J.M.C. 2011, *J. Geophys. Res.*, 116, D12303
- [1978] Sobolev, V.G. 1978, *Planet. Space Sci.*, 26, 703
- [1975] Staude, H.J. 1975, *A&A*, 39, 325
- [1972] Sternberg, J.R., & Ingham, M.F. 1972, *MNRAS*, 159, 1
- [2007] Sutter, B., Dalton, J.B., Ewing, S.A., Amundson, R., & McKay, C.P. 2007, *J. Geophys. Res.*, 112, G04S10
- [1981] Toller, G.N. 1981, Ph.D. Dissertation, State University of N.Y. at Stony Brook
- [1987] Toller, G.N., Tanabe, H., & Weinberg, J.L. 1987, *A&A*, 188, 24
- [1921] van Rhijn, P.J. 1921, *Publ. Astr. Lab. Groningen*, 31, 1
- [2011] Velikodsky, Y.I., Opanasenko, N.V., Akimov, L.A., et al. 2011, *Icarus*, 214, 30
- [2011] Vernet, J., Dekker, H., D'Odorico, S., et al. 2011, *A&A*, 536, A105
- [1999] von Savigny, C.H.A., McDade, I.C., Shepherd, G.G., & Rochon, Y. 1999, *Ann. Geophysicae*, 17, 1439

ESO	The Cerro Paranal Advanced Sky Model	Doc:	VLT-MAN-ESO-19550-5339
		Issue:	Issue 1.1.1
		Date:	Date 2013-09-18
		Page:	80 of 80

- [1987] Walker, A. 1987, NOAO Newsletter, 10, 16
- [2012] Warneck, P. & Williams, J. 2012, The Atmospheric Chemist's Companion: Numerical Data for Use in the Atmospheric Sciences, Springer
- [1975] West, J.B., & Broida, H.P. 1975, J. Chem. Phys., 62, 2566
- [WMO12] WMO Greenhouse Gas Bulletin, No. 8, 19 November 2012
- [1967] Wolstencroft, R.D., & van Breda, I.G. 1967, ApJ, 147, 255
- [1997] Wu, X. & Smith, L. 1997, Appl. Opt., 36, 2609
- [Anu Duhia 2009] Duhia, A. 2009, private communication

Links

- [1] http://rtweb.aer.com/lblrtm_frame.html
- [2] http://irina.eas.gatech.edu/Lab_5560/lblrtm/lblrtm_inst.html
- [3] ftp://ftp.aer.com/pub/anon_downloads/aer_documents/FAQ_LBLRTM.pdf
- [4] <http://www.cfa.harvard.edu/HITRAN/>
- [5] <http://ready.arl.noaa.gov/gdas1.php>
- [6] <ftp://arlftp.arlhq.noaa.gov/pub/archives/gdas1/>
- [7] <http://www.arl.noaa.gov/READYmet.php>
- [8] <http://www.aer.com/>
- [9] http://rtweb.aer.com/line_param_whats_new.html
- [10] <http://www.atm.ox.ac.uk/RFM/>
- [11] VLT Astronomical Site Monitor, ASM Data, User Manual, VLT-MAN-ESO-17440-1773
- [12] <http://disc.sci.gsfc.nasa.gov/giovanni/overview/index.html>
- [13] <http://www.spaceweather.ca/>

— End of document —